

**Applications of Bipolar Electrochemistry for Characterization of Electrocatalysts and the Development of Biosensors**

by

Buhua Wang

A dissertation submitted to the Graduate Faculty of  
Auburn University  
in partial fulfillment of the  
requirements for the Degree of  
Doctor of Philosophy

Auburn, Alabama  
August 8, 2020

Keywords: glucose biosensor, bipolar electrochemistry,  
cathodic chemiluminescence

Copyright 2020 by Buhua Wang

Approved by

Curtis Shannon, Chair, Professor of Chemistry & Biochemistry  
Christopher J. Easley, C. Harry Knowles Professor of Chemistry & Biochemistry  
Wei Zhan, Associate Professor of Chemistry & Biochemistry  
Byron H. Farnum, Assistant Professor of Chemistry & Biochemistry

## Abstract

Bipolar electrochemistry, which is an untraditional technique where redox reaction happens on the surface of a conducting object (BPE) that immersed in an electrolyte solution wirelessly connected with an external power source, has attracted great interest over last decades and used in a variety of fields. This dissertation work, which used bipolar electrochemistry as a basic platform, focuses on electrodeposition of bimetallic materials and its electrocatalysis on molecules, refinements of BPE setup on electrochemical cell, and biosensing.

Chapter 1 presents a detailed literature review on the background and operational principle of bipolar electrochemistry and ECL (electrochemiluminescence), and its applications on the fields of materials science and dynamic systems, sensing and screening, also, the current stage of research is detailly discussed. Moreover, a brief introduction on diabetes, especially on glucose detection based on bipolar electrochemistry platform.

Chapter 2 describes an experimental approach for adapting the principles of Raman Spectro-electrochemistry to electrodes controlled using a bipolar circuit, which allows the simultaneous acquisition of spectroscopic data as a function of both the electrode potential and the chemical composition of a bimetallic alloy and can be generalized to other system variables. The electrochemical reduction of 4-nitrothiophenol (4-NTP) was carried out on bimetallic Ag/Au alloy gradients and monitored in situ using a confocal Raman microscope with 785 nm excitation.

Chapter 3 illustrates the potential profiles from open cell frame, closed cell frame, and channel cell frame. And four models from channel cell frames were offered to describe and explain the channel potential based on the variables of normalized channel length and width. Most importantly, this work may give some guideline to some researchers to the determination of what

kind of cell frames to choose, what kind of details to be aware of for different cell frames, and what is the optimal cell frame design for the BPE system.

Chapter 4 reports a new glucose biosensor platform based on cathodic ECL in a closed BPE system. In this C-ECL-C-BPE (cathodic ECL in a close BPE cell) glucose biosensor,  $Ru(bpy)_3^{2+}$  (tris(2,2'-bipyridyl) ruthenium) used as luminophore and  $K_2S_2O_8$  used as co-reagent to generate the cathodic ECL signal; two GCEs (glassy carbon electrodes), one acts as BPE cathode and the other acts as driving anode, used in the reporting cell; and a commercial test strip that already modified  $GO_x$  (glucose oxidase) and mediator used in the sensing cell. Under a certain applied DC voltage, a higher current would produce when glucose concentration varied from low to high, which need reduce more  $Ru(bpy)_3^{2+}$  and persulfate to compensate for it and result in a more incensed ECL signal, using this mechanism, glucose detection could be achieved. Moreover, a comparison between proposed C-ECL-C-BPE glucose biosensor and commercial blood glucose meter was performed for determination of glucose in human serum samples.

Chapter 5 summarizes the research contribution of this dissertation, and a briefly statement of recommended future work of these projects.

## Acknowledgments

Pursuing a Ph.D. has been a challenging and rewarding experience in my life. By no means could I be able to achieve it without the help of countless people over the past years.

Firstly, I would like to express my sincere thanks to my advisor, Dr. Curtis Shannon for being such a great mentor, for his invaluable assistance, guidance, and encouragement throughout my PhD studies at Auburn. Dr. Shannon, your intelligence, enthusiasm, has a broad knowledge and rich experience on electrochemistry and surface science, set an example I hope to match someday. Also, deepest thanks for you allow me freely to test my ideas on research and pursuit my goals.

Next, I would like to offer my sincere gratitude for the incredible contributions from my committee members, Dr. Christopher Easley, Dr. Wei Zhan, Dr. Byron Farnum. Thank you for your generous guidance, suggestions, and kindly supports. Dr. Easley has always been amicable and put me at ease every time talking with him and give me some pertinent suggestions on my research. Dr. Zhan is honest and kind, gave me some useful and practical advice for doing a better presentation. Dr. Farnum is pleasant and obliging, helped me out to serve as my committee member, for that I really appreciated it.

Thanks also goes to Dr. Tae-Sik Oh from chemical engineering department for being my university reader, who is such a kind and descent man!

Also, a special thanks go to Dr. Masoud Mehrgardi from the University of Isfahan giving me some useful guidance on my research during his visiting time.

Thanks to my previous and current lab mates, Dr. Sanjun Fan, Dr. Songyan yu, Li Zhang, Apu Mazumder, Md Akteruzzaman, Waliul Khan and Humaira Yeasmin. Thank you for the fun and support. Good luck to all of you!

Thanks to students from Dr. Easley's group, especially Dr. Mark Holtan for his continuous assistance in 3D printing, photolithography, and electronics. Thanks to Dr. Xiangpeng Li encouragement during my hard time on research. Thanks to Dr. Subramanian Somasundaram for many patient and extensive discussions. Thanks also go to Nan Shi, Dr. Jean Negou, Dr. Juan Hu, Dr. Katarena Ford, and Gebriel Hagos.

I would like to give a special thanks to Peter Traverso for being such a great roommate and friend. I would also like thanks to my other friends, Dr. Chunkun Jiao, Dr. Mingming Wang, Dr. Chao Li, Qi Cui, Dr. Ye Li, Dr. Zening Liu, Sicheng Li, Jinyan Cui, Dr. Shamin Iqbal and Hui Jin.

Last but not the least, my deepest and greatest thanks go to my parents and other family members for their endless support, encouragement, and love.

## Table of Contents

<b>Abstract</b> .....	ii
<b>Acknowledgments</b> .....	iv
<b>Table of Contents</b> .....	vi
<b>Lists of Figures</b> .....	ix
<b>Lists of Tables</b> .....	xiii
<b>Chapter 1</b> .....	1
<b>Introduction</b> .....	1
<b>1.1 Bipolar electrochemistry</b> .....	1
1.1.1 Background of Bipolar electrochemistry .....	1
1.1.2 Principles of Bipolar electrochemistry.....	1
1.1.3 Open BPE system and Closed BPE system .....	3
<b>1.2 ECL (Electrochemiluminescence)</b> .....	5
1.2.1 Fundamentals of ECL .....	5
1.2.2 General Reaction Mechanisms .....	6
1.2.3 ECL Luminophores and Co-reagents.....	9
<b>1.3 Applications of Bipolar electrochemistry</b> .....	12
1.3.1 Bipolar Electrochemistry in Analytical Sensing.....	12
1.3.2 Bipolar Electrochemistry in Materials Science.....	16
1.3.3 Other Fields.....	19
<b>References</b> .....	21
<b>Chapter 2</b> .....	41
<b>Reduction of 4-nitrothiophenol on Ag/Au Bimetallic Alloy Surfaces Studied Using Bipolar Raman Spectroelectrochemistry</b> .....	41
<b>2.1 Introduction</b> .....	41
<b>2.2 Experimental Section</b> .....	44
2.2.1 Materials and Reagents .....	44
2.2.2 Preparation of Bipolar Electrochemical Cell Frames .....	44
2.2.3 Self-made tiny Ag/AgCl Reference Electrodes for Solution Potential Measurement .	45
2.2.4 Setup of Solution Potential Measurement.....	46
2.2.5 Electrodeposition of Ag/Au on Stainless Steel Substrate Using Bipolar System.....	46
2.2.6 SEM-EDX Measurement .....	47

2.2.7 Setup of Bipolar Cell for Raman Spectroscopy .....	47
<b>2.3 Results and Discussion</b> .....	48
2.3.1 Electrodeposition of Ag/Au Alloy on Stainless Steel BPE Substrate.....	48
2.3.2 Solution Potential Profile in Bipolar Cell System .....	52
2.3.3 Characterization of the Reduction of NTP Monolayer on Bimetallic Ag/Au Alloy Using BRSE.....	54
<b>2.4 Conclusions</b> .....	66
<b>References</b> .....	67
<b>Chapter 3</b> .....	72
<b>Control of the Potential Profile of Bipolar Electrodes Using Cell Frames</b> .....	72
<b>3.1 Introduction</b> .....	72
<b>3.2 Experimental section</b> .....	74
3.2.1 Materials and Reagents .....	74
3.2.2 Apparatus .....	75
3.2.3 Preparation of Bipolar Electrochemical Cell Frames .....	75
3.2.4 Prepared Self-made tiny Ag/AgCl Reference Electrodes for Solution Potential Measurement.....	76
3.2.5 Gold BPE cleanness.....	76
3.2.6 ECL measurement.....	76
<b>3.3 Results and Discussion</b> .....	77
3.3.1 Self-made Ag/AgCl reference electrodes .....	77
3.3.2 Closed cell frames versus open cell frames .....	78
3.3.3 Effect of Measuring tip depth and Concentration of electrolyte.....	81
3.3.4 Study of Potential Profile using Channel Cell Frames .....	82
3.3.5 Model the Potential of Channel Cell Frames.....	88
3.3.6 ECL Comparison using Closed Cell Frame and Channel Cell Frame.....	94
3.3.7 Multiple BPEs Cell Frames Design.....	96
<b>3.4 Conclusions</b> .....	98
<b>References</b> .....	100
<b>Chapter 4</b> .....	102
<b>Cathodic Electrochemiluminescence Glucose Biosensor Using Closed Bipolar Electrode System</b> .....	102
<b>4.1 Introduction</b> .....	102
<b>4.2 Experimental section</b> .....	107
4.2.1 Chemicals and Reagents .....	107

4.2.2 Apparatus .....	108
4.2.3 Modification of glassy carbon electrodes (GCEs) with GOx .....	108
4.2.4 Preparation of C-ECL-C-BPE glucose biosensor and data acquisition .....	109
<b>4.3 Results and discussion .....</b>	<b>109</b>
4.3.1 Effect of Acetonitrile for Cathodic ECL.....	109
4.3.2 Oxygen Effect for Cathodic ECL .....	112
4.3.3 Electrochemical study of modified GCEs.....	115
4.3.4 Electrochemical study of commercial blood glucose test strips .....	118
4.3.5 Performance of the Proposed Cathodic ECL Glucose biosensor in Closed BPE System .....	121
4.3.6 Glucose Detection of Human Serum .....	127
<b>4.4 Conclusions.....</b>	<b>131</b>
<b>References.....</b>	<b>132</b>
<b>Chapter 5 .....</b>	<b>139</b>
<b>Conclusions and Future Directions .....</b>	<b>139</b>
<b>5.1 Reduction of 4-NTP on Ag/Au Bimetallic Alloy Surfaces using Bipolar Raman Spectroelectrochemistry .....</b>	<b>139</b>
<b>5.2 Potential Profile of BPE using Different Cell Frames Design.....</b>	<b>140</b>
<b>5.3 Cathodic ECL Glucose Biosensor using Closed BPE System.....</b>	<b>141</b>



## Lists of Figures

<b>Figure 1.1</b> Basic Bipolar device and illustration of potential profile and redox reaction of the bipolar electrode in open configuration <sup>15</sup> , adapted with permission from Copyright © 2013 WILEY-VCH Verlag GmbH & Co. KGaA, Weinheim. ....	3
<b>Figure 1.2</b> Two kinds of bipolar electrochemistry systems: (A) an open configuration and (B) a closed configuration.....	4
<b>Figure 1.3</b> ECL mechanism of luminol with hydrogen peroxide. <sup>57</sup> Adapted with permission from Copyright © 2007, Springer Nature. ....	9
<b>Figure 1.4</b> (A) Synthetic route for Ru(bpy) <sub>3</sub> <sup>2+</sup> -labeled antibody and Ru(bpy) <sub>3</sub> <sup>2+</sup> -labeled oligonucleotide probes; (B) Schematic of the sandwich immunoassay and nucleic acid assays (the antibody or nucleic acid probes are labeled with biotin and Ru(bpy) <sub>3</sub> <sup>2+</sup> ). <sup>73</sup> Adapted with permission from Copyright © 2014, Springer Nature. ....	11
<b>Figure 1.5</b> Schematic representation of intracellular c-Myc mRNA detection using BPE- ECL biosensor. <sup>118</sup> Adapted permission from Copyright © 2012, American Chemical Society. ....	15
<b>Figure 1.6</b> Ag/Au alloy electrodeposition model. ....	17
<b>Figure 2.1</b> Bipolar Raman spectroelectrochemistry. Spectral data can be acquired along the potential gradient and the spatial dimension normal to it. In this study, the alloy composition varies along the second dimension. ....	42
<b>Figure 2.2</b> Bipolar electrochemical cell frames. (A) cell frame used for electrodeposition; (B) cell frame used for Raman characterizing. ....	45
<b>Figure 2.3</b> (A) Electrodeposition Bipolar shape and dimension sizes, the red part covered with parafilm, (B) the cut new BPE with alloy side dipped in NTP solution to form self-assembled monolayer, (C) Raman scanning sequence of BPE cartoon. ....	46
<b>Figure 2.4</b> Linear Sweep Voltammogram scanned in 10 mM KAu(CN) <sub>2</sub> and 10mM KAg(CN) <sub>2</sub> with 200mM KCN supporting electrolyte solution, pH=12. Ag/AgCl electrode as reference electrode, Pt grid as counter electrode, stainless-steel as working electrode, scan rate: 100mV/s. ....	49
<b>Figure 2.5</b> Cyclic voltammogram of co-deposition solution (A), scan rate 50 mV/s. SEM image of the Ag/Au alloy (B), bar size: 1 μm. The alloy gradient composition obtained from EDX measurements along the major and minor axes of the BPE cathode (C, D). Error bars indicate the standard deviation of three independent measurements. ....	50
<b>Figure 2.6</b> (A) Solution potential difference ΔE <sub>bpe</sub> between the end of cathode and the end of anode of BPE length at the left edge, middle and right edge in the Raman Bipolar cell (6 V applied voltage on Au driving electrode, and the length of BPE is 26mm). (B) Potential difference ΔE <sub>bpe</sub> as a function of time in the middle major axis line (6 V applied voltage on Au driving electrode, and the length of BPE is 30mm).....	53
<b>Figure 2.7</b> (A) Schematic NTP reduction mechanisms of (1) direct reduction to 4-aminothiophenol (ATP) and (2) through an intermediate 4,4'-dimercaptoazobenzene (DMAB) to ATP. (B) CVs of NTP monolayer on three different substrates: Au, Ag and Ag/Au alloy on stainless-steel, respectively, in 0.1M NaClO <sub>4</sub> solution bubbled with nitrogen, scan rate: 5 mV/s. (C) Raman spectrum of NTP at equilibrium states on Ag/Au alloy. ....	56
<b>Figure 2.8</b> Raman spectra (A) acquired at -625 mV at the indicated alloy compositions. Normalized Raman peak intensity profiles for R (B), I <sub>1335</sub> /I <sub>1080</sub> (C), and I <sub>1434</sub> /I <sub>1080</sub> (D).....	58
<b>Figure 2.9</b> (A) and (B) are normalized Raman peak intensities of I <sub>1335</sub> /I <sub>1080</sub> , (I <sub>1594</sub> -I <sub>1572</sub> )/(I <sub>1594</sub> +I <sub>1572</sub> ) as a function of distance from the BPE cathodic edge measured on Au and Ag	

substrate under 6V applied voltage on the driving electrodes, respectively; (C) and (D) are voltammograms of NTP reduction on different substrates as Ag/AgCl reference electrode in 0.1 M NaClO <sub>4</sub> solution under nitrogen atmosphere with a scan rate of 5 mV/s, Pt grid as counter electrode.....	59
<b>Figure 2.10</b> Solution potential as a function of measuring distance in 0.1M NaClO <sub>4</sub> using the Raman cell frame under 6V applied voltage.....	60
<b>Figure 2.11</b> Normalized Raman peak intensity profiles on pure Au: I <sub>1335</sub> /I <sub>1080</sub> (A); R (C). Raman spectra (B) acquired along the red-dashed line in (A). .....	62
<b>Figure 2.12</b> Normalized Raman peak intensity profiles on pure Ag: I <sub>1335</sub> /I <sub>1080</sub> (A); (I <sub>1594</sub> -I <sub>1572</sub> )/(I <sub>1594</sub> +I <sub>1572</sub> ) (C); and I <sub>1434</sub> /I <sub>1080</sub> (D). Raman spectra (B) acquired along the red-dashed line in (A). .....	63
<b>Figure 3.1</b> Electric field strength illustrated in three cell frames, (A) open cell frame, (B) closed cell frame and (C) channel cell frame.....	74
<b>Figure 3.2</b> (A), (B) and (C) are open cell frame, closed cell frame and channel cell frame, respectively. ....	75
<b>Figure 3.3</b> (A) is a picture of Self-made reference electrode. (B) Cyclic Voltammograms of two self-made Ag/AgCl reference electrodes, Pt electrode as counter electrode, Au electrode as working electrode, scan in 2 mM Potassium Ferricyanide (III) solution from 0.5 volt to (-0.1) volt with 0.5 M KNO <sub>3</sub> as supporting electrolyte, scan rate: 50 mv/s (Red and blue CV scanned using two self-made electrodes).....	77
<b>Figure 3.4</b> (A) Solution potential measurement scheme; (B) solution potential profile of closed cell frames vs open cell frames; (C) solution potential profile of closed cell frames vs open cell frames at different applied voltage under 30 mm measuring distance. ....	79
<b>Figure 3.5</b> (A) Solution potential as a function of measuring distance under different applied voltage using closed cell frames; (B) dropped potential at different applied voltage in the closed cell frame;(D) potential profile in different closed cell frame width under different applied voltage measured at 30mm distance using (C) cell frame design.....	80
<b>Figure 3.6</b> (A) Potential profile of different measuring tip depth under different applied voltage at a fixed measuring distance; (B) potential profile of different concentrated electrolyte under different applied voltage at same measuring distance. ....	82
<b>Figure 3.7</b> (D) Channel potential as function of channel position under different applied voltage by using (A), (B) and (C) cell frames, channel with 30mm length × 2mm width.....	83
<b>Figure 3.8</b> (B) Potential profile along the red line using (A) cell frame under 7V applied voltage, channel with 30mm length × 2mm width; (C) Scheme of BPE (green color) placed in three different channel cell frames, BPE length is larger, equal, and smaller than that of the channel, respectively; (D) BPE (5mm) potential as a function of channel width with different channel length (5mm, 15mm, 30mm and 40mm, respectively) under 7V applied voltage (CL x/y meaning potential across x mm channel divided by y).....	84
<b>Figure 3.9</b> (A) Potential profile across the channel as function of normalized channel width under different channel length with 7V applied voltage; (B) Potential profile across the channel as function of normalized channel length under different channel width with 7V applied voltage; (C) Measured potential profile across the channel (top view) as function of normalized channel width and length with 7V applied voltage. ....	86
<b>Figure 3.10</b> (A) Potential profile (across 30mm channel length, measured close to channel edges and located the middle of channel) as a function of channel width under different applied	

voltage; (B) Potential profile measured at different position across the channel of 32mm channel width under 7V applied potential.....	87
<b>Figure 3.11</b> (C) Channel potential profile as a function of normalized channel length using (A), (B) types of cell frames, and four calculation methods, channel width 2mm with 7V applied voltage; (D) Simple scheme used for describing potential modeling calculation of ellipse.....	93
<b>Figure 3.12</b> (A) ECL intensity at different applied voltage by using closed cell frame (B) and channel cell frame (C), 2mm channel width and 30 mm length, Au foil BPE with a length of 30mm; (B) and (C) is closed cell frame and channel cell frame under 4V applied voltage, respective, and (D) and (E) is the corresponding surface plot of gray value (or ECL intensity) crossing the anodic driving electrode. ....	95
<b>Figure 3.13</b> (C) Potential profile as a function of applied voltage using cell frame (A) (three channels 2mm width $\times$ 6mm length, two rectangular reservoirs both with a 6mm length) and (B) (channel 2mm width $\times$ 30mm length); (C-30)/5 defines potential of channel (B) divided by 5; Small C-6 defines potential across center channel from cell frame (A) (red and blue dots); Small R-6 defines potential across small rectangular reservoir from (A) (black and red dots).....	97
<b>Figure 3.14</b> (C) Potential measured at different channel position under different applied voltage by using cell frame (A) (channel evenly separated) and (B), all the channels 2mm width $\times$ 30mm length, A-L(M/R) defines left (middle/right) channel from cell frame (A), C-L(M/R) defines left (middle/right) channel from cell frame (B). ....	98
<b>Figure 4.1</b> Cathodic ECL Glucose biosensor Mechanism in Closed BPE system. ....	105
<b>Figure 4.2</b> (A)-(F) experimental setup: three GCEs binding together dipping in ECL solution (0.5mM Ru(bpy) <sub>3</sub> 2 <sup>+</sup> , 10mM K <sub>2</sub> S <sub>2</sub> O <sub>8</sub> ), one connected positive DC power supply, one connected the negative and the last one connected nothing as comparison for the other two electrodes. (A) and (B) are the camera screenshot of experimental setup before and after measurement; (C)-(E) collected after experiment begins 10 sec, 60 sec and 120 sec under 3.3V applied DC voltage, respectively, in ECL solution contains 35% acetonitrile, while (F) collected under same condition but with ECL solution without acetonitrile; (G) collected using cyclic voltammetry scanned from (-0.5)V to (-1.5)V, (-1.6)V and (-1.7)V, respectively, ECL solution used contains 35% acetonitrile for the first two measurements (yellow area) while the last one does not contain it (pink area), scan rate is 50mV/s, GCE as working electrode, Ag wire as quasi-reference electrode, Pt grid as counter electrode. ....	111
<b>Figure 4.3</b> (A)-(C) collected using chronoamperometry at different potential for 10 sec in ECL solution (0.25mM Ru(bpy) <sub>3</sub> 2 <sup>+</sup> , 0.5mM K <sub>2</sub> S <sub>2</sub> O <sub>8</sub> in 0.1M PBS buffer contains 35% acetonitrile, pH=8) with/without bubbling N <sub>2</sub> , GCE as working electrode, Ag wire as quasi-reference electrode, Pt grid as counter electrode. (D) collected C-ECL-C-BPE glucose biosensor used commercial glucose blood test strip measured 12 mM glucose with ECL solution (62.5uM Ru(bpy) <sub>3</sub> 2 <sup>+</sup> , 0.125mM K <sub>2</sub> S <sub>2</sub> O <sub>8</sub> ) with/without bubbling N <sub>2</sub> in the reporting cell under 3.6V applied DC voltage with 5 sec for each measurement. ....	113
<b>Figure 4.4</b> Cyclic voltammograms of GCE, (A) scanned in 0.1M PBS buffer (contains 35% acetonitrile) bubbled N <sub>2</sub> and 1mM K <sub>2</sub> S <sub>2</sub> O <sub>8</sub> in 0.1M PBS buffer (contains 35% acetonitrile) bubbled N <sub>2</sub> ; (B) scanned in ECL solution (0.5mM Ru(bpy) <sub>3</sub> 2 <sup>+</sup> , 1mM K <sub>2</sub> S <sub>2</sub> O <sub>8</sub> ) with/without bubbling N <sub>2</sub> . Scan rate is 30mV/s, Ag wire as quasi-reference electrode, Pt grid as counter electrode.....	114
<b>Figure 4.5</b> (A) Cyclic voltammograms of modified GCEs/GO <sub>x</sub> /GA/Nafion electrode scanned in different concentrated glucose solution contains 1mM hydroquinone, Ag/AgCl as reference electrode, and Pt grid as counter electrode, scan rate 20 mV/s; (B) the calibration curves of cyclic	

voltammograms from GCEs/GO <sub>x</sub> /GA/Nafion electrode, each color curve represent from one individual modified GCEs/GO <sub>x</sub> /GA/Nafion electrode measurement;(C) same as (B) except the electrode modified with GCEs/GO <sub>x</sub> /GA/MWCNTs/Nafion. ....	116
<b>Figure 4.6</b> (A) ECL intensity curves from C-ECL-C-BPE method using GCEs/GO <sub>x</sub> /GA/Nafion electrode as BPE anode as the applied voltage employed from 4500mV to 5580mV; (B) Initiated ECL voltage from two sets of ECL intensity curves employed C-ECL-C-BPE method using GCEs/GO <sub>x</sub> /GA/Nafion electrode as BPE anode.....	117
<b>Figure 4.7</b> (A) Commercial contour next EZ blood glucose meter; (B) and (C) are un-used glucose test strip and used one, respectively; (D) is inside structure of un-used test strips, and (E) is the used one. Note that the white line on the test strip is insulating. ....	119
<b>Figure 4.8</b> (A) ECL signal calibration curve as a function of glucose concentration, L1 is BPE anode, and L2 as driving cathode, ECL solution (62.5uM Ru(bpy) <sub>3</sub> 2 <sup>+</sup> , 0.125mM K <sub>2</sub> S <sub>2</sub> O <sub>8</sub> ), applied voltage 4800mV; (B) is ECL intensity spectra corresponding to (A); (C) is ECL intensity spectrum scanned in serum sample.....	120
<b>Figure 4.9</b> (A) collected four individual cathodic ECL intensity measurement of 5mM and 12 mM glucose in closed BPE system, commercial glucose blood test strip used to measure in the sensing cell and two GCEs in the reporting cell with Q =(62.5uM Ru(bpy) <sub>3</sub> 2 <sup>+</sup> , 0.125mM K <sub>2</sub> S <sub>2</sub> O <sub>8</sub> ) ECL solution; (B) is the ECL intensity (V) calibration curve of glucose measurement using C-ECL-C-BPE glucose biosensor method with Q concentrated ECL solution as function of concentration; red line is the logistic fit of the data, blue line in the yellow area is the linear fitting of the data; (C) is the ECL intensity signals corresponding to calibration curve of (B); (D) is the calibration curves of ECL intensity at different concentration as function of glucose concentration using C-ECL-C-BPE glucose biosensor method. All the measurements obtained under 3.6V applied DC voltage and 5 sec except for 4Q curve achieved under 3635mV, each data point measured at least three times. ....	122
<b>Figure 4.10</b> (A) and (C) are ECL Signal intensity curves as function of measuring glucose concentration using different concentrated ECL solution, each data point measured at least three times; (B) and (D) are the ECL signal responses at different glucose concentration corresponding (A) and (C), respectively. Two GCEs used in the sensing cell under 4.6V applied voltage and 5 sec for each measurement. ....	124
<b>Figure 4.11</b> (A), (B) and (C) are ECL signal intensity (V) responses at different glucose concentrations using C-ECL-C-BPE glucose biosensor method with 0.5Q, 2Q and 4Q concentrated ECL solution, respectively. ....	127
<b>Figure 4.12</b> Comparison of methods for determining glucose concentrations in human serum samples. Black data measured using proposed C-ECL-C-BPE method; blue data is the correction of black data; red data measured using commercial Contour NEXT EZ blood Glucose Meter. Each data point measured at least three times. ....	130

## Lists of Tables

<b>Table 1</b> Information of Human Serum Samples.....	129
<b>Table 2</b> Comparison between C-ECL-C-BPE method with Contour NEXT EZ Blood Glucose Meter for glucose measurement. ....	130

# Chapter 1

## Introduction

### 1.1 Bipolar electrochemistry

#### 1.1.1 Background of Bipolar electrochemistry

Bipolar electrochemistry, an untraditional technique generates asymmetric reactions on the surfaces of two poles of conductive objects (BPEs) in a wireless manner,<sup>1-2</sup> has attracted great attention recently and widely used in a variety of fields including wastewater treatment,<sup>3</sup> energy,<sup>4</sup> material catalysis,<sup>5</sup> cation enrichment,<sup>6</sup> analytical sensors,<sup>7</sup> screening/grafting,<sup>8-9</sup> etc.

#### 1.1.2 Principles of Bipolar electrochemistry

Bipolar Electrode (BPE), which is a conductor immersed in an ionic solution without direct connection to the external power source. When the electric field generated by the potential applied by the two driving electrodes large enough to cause faradaic reaction, oxidation and reduction would happen simultaneously on each pole of the BPE.<sup>10</sup> Compared to conventional electrochemistry, which based on a three electrode system composed of working, counter (or auxiliary), and reference electrodes, and the working electrode directly connected to a power source that allows a potential difference to be applied between the working electrode and counter electrode, the BPE polarized with respect to solution and as a result redox reactions occur at the electrode/solution interface of two poles of BPE simultaneously.<sup>11</sup>

A simple design of bipolar electrochemistry experiment can be easily achieved by immersing a conductive object (BPE) into electrolyte solution, with sufficient voltage applied on the two driving electrodes, as illustrated in Figure 1.1, which is typical cartoon configuration used for bipolar electrochemistry, the driving electrodes apply a uniform electric field across the electrolyte

solution, and the resulting faradaic electrochemical reactions at the BPE are shown, occurring oxidation at the anodic (blue arrow) pole and reduction at the cathodic (red arrow) pole of the BPE. Since the interfacial potential between the solution and BPE is highest at the ends part, the faradaic processes are always start there first. Specifically, the applied voltage to the driving electrodes results in an electric field that causes the BPE floating to an equilibrium potential depends on its position in the field and composition of electrolyte solution,<sup>12</sup> due to the electric field in solution, the interfacial potential between the BPE and solution varies with its length, and the corresponding anodic and cathodic overpotential,  $\eta_{an}$  and  $\eta_{cat}$ , respectively, which drives the redox reaction happens at the two poles of BPE, and the position of zero overpotential on the BPE with respect to the solution, which defines as  $x_0$ , depends on the nature of faradaic processes occurring at the poles of BPE.<sup>13</sup> And the potential across the BPE ( $\Delta E_{BPE}$ ) could be roughly estimated from the equation (1.1):<sup>14-15</sup>

$$\Delta E_{BPE} = E_{tot} \left( \frac{l_{BPE}}{l_0} \right) \quad (1.1)$$

where  $E_{tot}$  is the voltage applied on the driving electrodes,  $l_{BPE}$  is the length of BPE,  $l_0$  is the distance between two driving electrodes. Note that equation (1.1) does not account for any potential loss at the interface between driving electrode and solution. The fractional loss of  $E_{tot}$  within electrochemical double layer can be significant under some conditions. In that case, equation (1.1) would not be appropriate to use.<sup>15</sup> For instance, electrolytic solution contains a very high concentrated supporting electrolyte, a voltage applied to the driving electrodes generates a electrochemical double layer upon accumulating ions at the interfaces between electrode and solution, a significant steep electric field would generate within the range of double layers (normally a couple of nanometers thickness), which means a large potential loss at the driving electrode surfaces from applied voltage, thus, less voltage would contribute the formation of

electric field across the solution between two driving electrodes.<sup>16</sup> Thus the nature of electric field formed in the solution between two driving electrodes depends on driving electrode materials, bipolar cell frames geometry and conductivity of electrolyte solution, more information refers to chapter 3.

The principle of two-dimensional (2D) bipolar electrochemistry was also reported based on the use of a 2D BPE surface addressed with two sets of feeder electrode arrays, which allows electrochemical reactions can be localized at particular locations on the perimeter of a two-dimensional BPE that configured at the inter-section of two orthogonal microfluidic channels.<sup>17</sup>

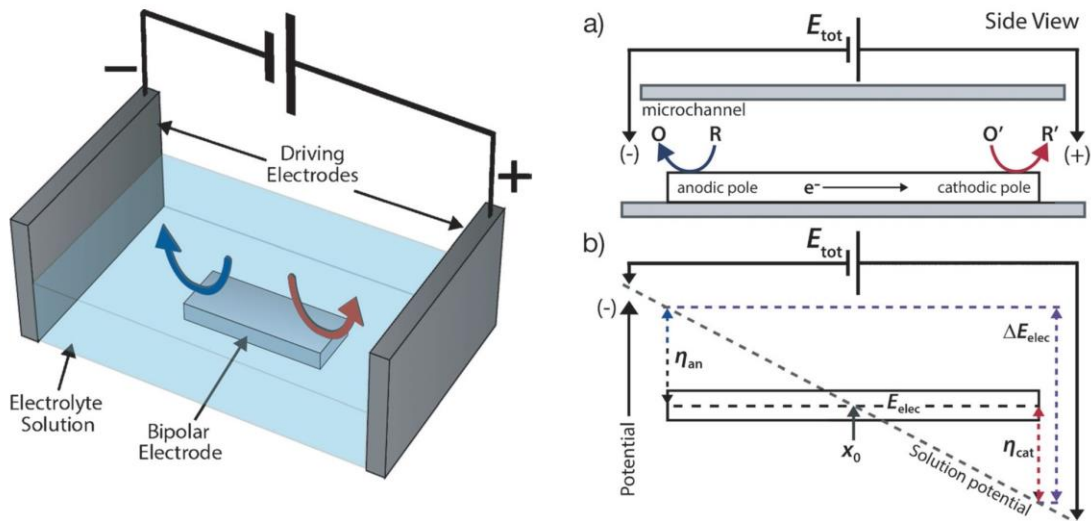


**Figure 1.1** Basic Bipolar device and illustration of potential profile and redox reaction of the bipolar electrode in open configuration<sup>15</sup>, adapted with permission from Copyright © 2013 WILEY-VCH Verlag GmbH & Co. KGaA, Weinheim.

### 1.1.3 Open BPE system and Closed BPE system

According to the differences of configuration, bipolar electrochemistry systems could be divided into two categories, open BPE system and closed BPE system, as illustrated in Figure 1.2. And the potential across the BPE ( $\Delta E_{BPE}$ ) mentioned above is based on the open BPE system. One



of the most important differences and advantages of open BPE system is the potential gradient in the solution between two driving electrodes. For example, the modification of an electrode surface with a molecular gradient has been reported via the bipolar reduction of aryl diazonium salts to analyze the in-plane molecular distribution;<sup>18</sup> A 3D gradient polymer brush generated by a concentration gradient of eATRP that formed due to the potential gradient of BPE electrochemistry.<sup>19</sup> In terms of closed BPE system, multiple advantages exhibits as below:

1) Compared with open BPE system, the closed BPE system is comprised of two cells, one is reporting cell, and the other one is sensing cell used for detecting interested analytes, which makes the reporting molecules not interfere the interested analyte during detecting performance.

2) another main advantage of closed BPE system is the current passes through the whole system is same due to the connection between BPE with solutions in series, which could increase the current efficiency on the BPE and lower the external applied voltage, and a lower applied voltage could further lower byproducts generation on the driving electrodes and may lead to increase the stability and sensitivity of measurement.

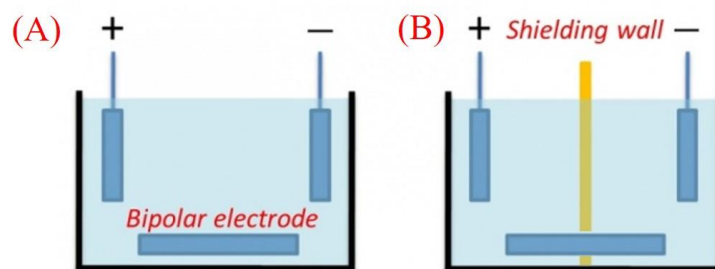


**Figure 1.2** Two kinds of bipolar electrochemistry systems: (A) an open configuration and (B) a closed configuration.

3) furthermore, the anodic driving electrode and cathodic driving electrode often immersed in the same cell of open BPE system, the interested analytes preferentially consumed at the surfaces of driving electrodes is huge, while in closed BPE system, two driving electrodes are separated in

different cells, which could alleviate the amount of consumption of interested analytes happened on the driving electrode.

For instance, to evaluate cellular respiration of individual cell aggregates, a closed BPE array that could separate electrochemiluminescence (ECL) chemicals from cell aggregates was employed for on-chip analysis.<sup>20</sup>

## **1.2 ECL (Electrochemiluminescence)**

### 1.2.1 Fundamentals of ECL

CL (chemiluminescence), which is the emission of light initiated by the homogeneous chemical reaction between at least two reagents. Most of CL results from vigorous oxidative reduction reactions, which consequently lead to CL has general problems including instability of reagents, difficulties in spatial and temporal control, etc.<sup>21</sup> ECL (electrochemiluminescence), also called electrogenerated chemiluminescence, is the generation of light initiated by excited states luminophore species formed at or near the electrode surfaces during electrochemical reactions.<sup>22-</sup>  
<sup>23</sup> It is the combination of CL and electrochemistry, and the initial electrochemical step is triggering a cascade of chemical reactions to form reactive intermediates, which then would undergo highly homogeneous electron-transfer (ET) reactions to generate excited state of luminophore (or electrochemiluminophore), and following by relaxing to the ground states to emit light.<sup>24</sup> ECL is also different from photoluminescence (typically, fluorescence and phosphorescence) as a result of absorption of light or electromagnetic radiation, and electroluminescence as a production of direct conversion of electric energy to light. Compared to photoluminescence, ECL does not need light source that may interfere the collection of ECL signal; compared to electroluminescence, ECL is related to chemical and electrochemical reactions.<sup>24-25</sup> ECL, as one kind of electrochemical techniques that ECL signal has a quantitative relationship with the concentration of interested

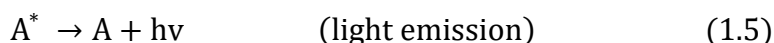
analytes, has been widely used in biomolecule detection,<sup>26-27</sup> food<sup>28-29</sup> and drug analysis,<sup>30</sup> clinical diagnosis,<sup>31</sup> and environmental monitoring,<sup>32</sup> due to its high sensitivity, broad linear range, and rapid analysis with a low background.<sup>33-34</sup>

## 1.2.2 General Reaction Mechanisms

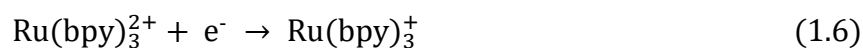
Since the first ECL observation of Grignard compounds<sup>35</sup> and luminol (5-amino-2,3-dihydro-1,4-phthalazinedione)<sup>36</sup> in 1920s published, more and more ECL luminophores had been reported and detailed ECL working principle been offered.<sup>37-40</sup> And the general ECL mechanisms mainly including ion annihilation process and co-reagent process.

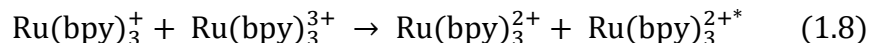
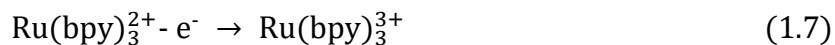
### 1.2.2.1 Annihilation ECL

In annihilation, the ECL luminophore species are electrochemically oxidized and reduced by applying an alternating pulsed potential to generate the oxidized species and reduced species, both of which species would react to undergo electron transfer to produce excited states luminophore, which relaxes to ground state and emits the ECL light.<sup>23</sup> And a typical system would contain reagent A and B in solution with supporting electrolyte, the general mechanism is illustrated below:<sup>41</sup>



Where A and B could be the same species. A good example is bard group using Ru(bpy)<sub>3</sub><sup>2+</sup> to generate ECL by alternatively pulsing of an electrode potential in acetonitrile, the mechanisms showed below:<sup>42</sup>



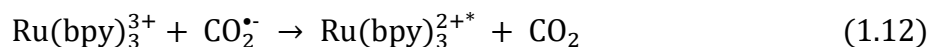
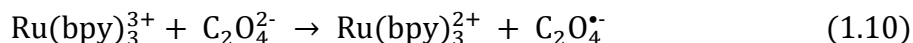


Another classic example involves rubrene, ECL observed when a double potential step applied to the electrode (such as gold, platinum or glassy carbon).<sup>43-44</sup>

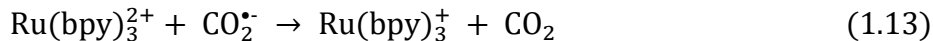
A successful annihilation ECL process should include a stable chemical or a long lifetime of electrogenerated species, if these species react with solvent or other compound from the solution, ECL intensity signal would be decreased or quenched, therefore, the lifetime of electrogenerated species should be long enough to react and produce the excited states luminophore.<sup>45-46</sup>

#### 1.2.2.2 Co-reagent ECL

In the ECL co-reagent process, ECL emissions generated in a single potential step at an electrode immersed in a solution containing luminophore and co-reagent. Both the luminophore and co-reagent can be oxidized or reduced first, and the intermediates formed from the oxidized or reduced co-reagent decomposed to produce strong oxidizing or reducing species, following the chemical reaction between the oxidizing/reducing species and reduced/oxidized luminophore occurs to produce the excited state luminophore complex, which initiates light.<sup>25</sup> To better illustrate the general mechanisms of co-reagent ECL, oxalate, which was the first co-reagent discovered,<sup>47-48</sup> used to as an example, and  $\text{Ru}(\text{bpy})_3^{2+}$  as the luminophore, and the ECL mechanisms showed below:<sup>21, 49</sup>



Or



From the mechanisms we can clearly see that annihilation also occurs along with the co-reagent ECL electrochemical reactions happening. Moreover, the ECL only be observed at or near the anodic electrode surface when using oxalate as co-reagent, and this behavior as anodic ECL. Similar behavior also observed when using tri-n-propylamine (TPrA) as co-reagent.<sup>50</sup> Alternatively, persulfate was used as co-reagent to electro-generate an oxidizing agent, in which persulfate would be reduced to give off sulfate anion radical, which is a strong oxidant, and reacts with the reduced luminophore to generate the excited states, which emits light.<sup>51</sup> And, when persulfate used as co-reagent, ECL generated can be observed at or near the cathodic electrode surface, which phenomenon named as cathodic ECL.<sup>52-53</sup> Similar cathodic light emission has also been observed at oxide covered metal electrode (such as aluminum, tantalum) under some conditions.<sup>54-55</sup>

However, it is difficult to oxidize some co-reagents either by the oxidized luminophore or at the electrode. For example, the ECL cannot be initiated in the presence of pyruvate, which is the co-reagent, and  $\text{Ru}(\text{bpy})_3^{2+}$ , in this case, Cerium (III) salt was added to the solution to generate ECL, because pyruvate can be oxidized by the electrogenerated Cerium (IV).<sup>56</sup>

Generally, for inorganic luminophores, the excited states generation through electron transfer without involving bonding breaking, while for some organic luminophores, the ECL mechanisms is a little different for involving bond breaking. For example, the ECL generation using luminol as luminophore, as demonstrated in Figure 1.3, luminol is oxidized at electrode surface and forms

diazoquinone intermediate under aqueous alkaline condition, then the intermediate further reacts with hydrogen peroxide to generate luminol endoperoxide, which continues produce to 3-aminophthalate in an excited state by bond cleavage, and finally emits the 425nm blue light.<sup>57</sup>

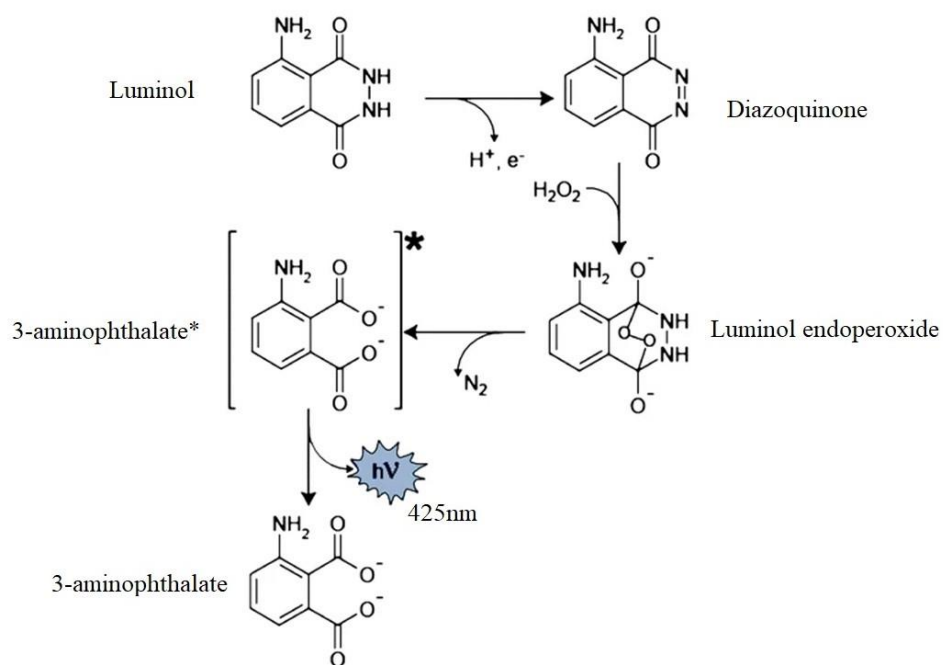


**Figure 1.3** ECL mechanism of luminol with hydrogen peroxide.<sup>57</sup> Adapted with permission from Copyright © 2007, Springer Nature.

### 1.2.3 ECL Luminophores and Co-reagents

Luminophores used for generation of ECL mainly divided into two categories, inorganic complexes, and organic molecules.

In terms of inorganic luminophores, considering many metal complexes and clusters served as ECL luminophores applied in electrochemical and spectroscopic qualities, the ECL complexes or clusters mainly including aluminum,<sup>58</sup> cadmium,<sup>59</sup> chromium,<sup>52</sup> copper,<sup>60</sup> europium,<sup>61</sup> gold,<sup>62</sup> iridium,<sup>63</sup> osmium,<sup>64</sup> molybdenum,<sup>65</sup> platinum,<sup>66</sup> rhenium,<sup>67</sup> ruthenium,<sup>68</sup> silver,<sup>69</sup> etc.. Surprisingly,  $Ru(bpy)_3^{2+}$  complexes has been proved to be the most valuable in both fundamental research studies and commercial applications. It probably due to its high efficiency luminescence,

easy to dissolve in both aqueous and organic solvent at room temperature, and ability to occur reversible one electron transfer at easily obtained potentials. For example, researchers discovered that  $\text{Ru}(\text{bpy})_3^{2+}$  ECL efficiency is 0.05 and that the efficiency of emitting charge transfer state produced from annihilation reactions approaching 100%.<sup>70-71</sup> Moreover, the strategy of ECLIA (ECL immunoassays) take advantage of ruthenium ECL labeling since Bard and Whitesides presented the ground breaking idea.<sup>72</sup> Thus, it lead to a wide applications of  $\text{Ru}(\text{bpy})_3^{2+}$ , for example, one predominant format of ECL bioassays for targeting many different biomolecules and antibodies commercially available based on ruthenium ECL labeling combined with magnetic solid support, as illustrated in Figure 1.4, which showed the synthetic route for  $\text{Ru}(\text{bpy})_3^{2+}$ -labeled antibody and  $\text{Ru}(\text{bpy})_3^{2+}$ -labeled oligonucleotide probes, together with the configuration of the sandwich immunoassay and nucleic acid assays.<sup>73</sup> Furthermore, ruthenium ECL also used in areas including DNA detection,<sup>74</sup> protein determination from human plasma or serum,<sup>75</sup> etc..

As for organic luminophores, mainly including acenaphthalene,<sup>76</sup> binaphthyl,<sup>63</sup> bis(2,4,6-trichlorophenyl)peroxyoxalate,<sup>77</sup> DPBF,<sup>78</sup> luminol,<sup>79</sup> lucigenin,<sup>80</sup> poly(9,9-dioctylfluorene) polymer,<sup>81</sup> pyrene/phenothiazine-substituted peptides,<sup>82</sup> tri-carbocyanine dye IR125 & IR144,<sup>83</sup> aromatic hydrocarbons-tetrathiafulvalene,<sup>84</sup> rubrene,<sup>85</sup> indole/tryptophan,<sup>86</sup> etc.. Among these organic luminophores, luminol and its derivatives are widely used due to their high luminescence efficiency and solubility in aqueous or non-aqueous medium. For instance, a dual-signaling ECL ratio-metric sensing approach for the detection of HL-60 cancer cells proposed by using luminol modified Ag-PAMAM nanocomposites and G-C<sub>3</sub>N<sub>4</sub> nanosheets serving oxidative–reductive and reductive–oxidative ECL emitters respectively.<sup>87</sup> Similarly, ECL immunosensor for Amyloid- $\beta$  detection was reported by using luminol that constructed by ceria doped ZnO nanomaterials with flower-structure.<sup>88</sup> In a similar way, an ECL enzyme immunoassay for 2,4,6-trinitrotoluene (TNT)

was demonstrated, specifically, the deposition of a re-usable immunosorbent dextran surface that anchored to an Au surface in the flow cell through thiol groups serves as sensing layer, antibodies labelled with glucose oxidase used in competitive immunoassays, where the separation step was carried out via concentrating unbound antibodies on the immunosorbent surface, hydrogen peroxide would be generated by the antibodies labelled glucose oxidase when glucose pumped through and luminol ECL would be initiated, the ECL signal was inversely proportional the TNT concentration.<sup>89</sup>

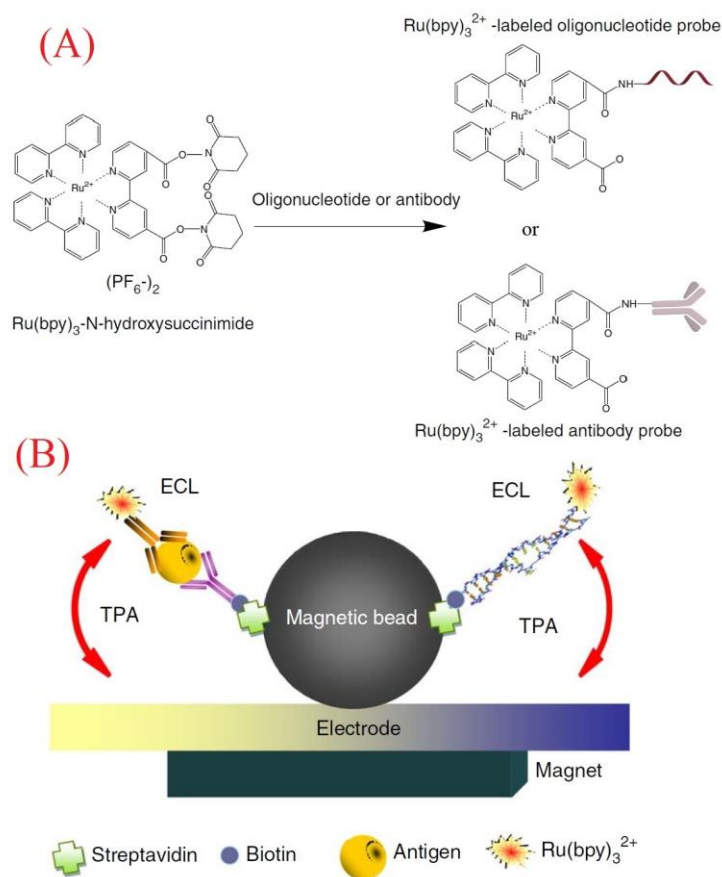


**Figure 1.4** (A) Synthetic route for  $\text{Ru}(\text{bpy})_3^{2+}$ -labeled antibody and  $\text{Ru}(\text{bpy})_3^{2+}$ -labeled oligonucleotide probes; (B) Schematic of the sandwich immunoassay and nucleic acid assays (the antibody or nucleic acid probes are labeled with biotin and  $\text{Ru}(\text{bpy})_3^{2+}$ ).<sup>73</sup> Adapted with permission from Copyright © 2014, Springer Nature.



The co-reagents used for the ECL mainly contains oxalate,<sup>90</sup> tri-n-propylamine (TPrA),<sup>91</sup> persulfate,<sup>92</sup> hydrogen peroxide,<sup>93</sup> amines,<sup>50</sup> acridine orange,<sup>94</sup> 2-(dibutyl-amino)ethanol (DBAE),<sup>95</sup> oxygen,<sup>96</sup> benzoyl peroxide,<sup>97</sup> etc..

More luminophores and co-reagents refers to review paper.<sup>41</sup>

### **1.3 Applications of Bipolar electrochemistry**

#### **1.3.1 Bipolar Electrochemistry in Analytical Sensing**

Since the concept of BPE was first proposed by Fleischmann and co-worker in 1960s,<sup>98</sup> bipolar fluidized bed electrodes have been used in applications enhancing the efficiency of electrosynthesis,<sup>99</sup> batteries<sup>100</sup> and photoelectrochemical cells.<sup>101</sup> As a wireless technique, it is hard to directly monitor the faradaic current promoted by the differences between the BPE and solution, which may limit the analytical applications of bipolar electrochemistry. The first time ECL was introduced to bipolar electrochemistry in 2001 by Manz et al. applied for micellar electro-kinetic chromatographic separation of dichloro-tris(2,2'-bipyridyl)ruthenium(II) hydrate ( $\text{Ru}(\text{bpy})_3^{2+}$ ) and dichloro-tris(1,10-phenanthroline)ruthenium-(II) hydrate ( $\text{Ru}(\text{phen})_3^{2+}$ ) on a microfabricated glass device, which consists of a microfabricated 'U' shape floating platinum electrode placed across the separation channel.<sup>102</sup> The applications of bipolar electrochemistry expands widely areas. Subsequently, the Crooks group proposed a microfluidic-base system, which used the basic principle of bipolar electrochemistry, generating electrochemical coupling between a sensing reaction and a reporting one that could be for instant ECL, which could imply the faradaic processes happened at the two poles of BPE.<sup>103</sup> Up to now, a great variety of analytical techniques have been brought in bipolar electrochemistry, such as ECL,<sup>104-105</sup> visual assay based on electrochromic materials<sup>106-107</sup> or metal electro-dissolution/deposition,<sup>9, 108</sup> fluorescence,<sup>109-110</sup> directly current recording with ammeter<sup>111</sup> or LED (light emitting diode) in split BPE system,<sup>112</sup> and

electromechanical readout.<sup>113</sup> Among all the detection techniques, ECL matches well with the wireless nature of BPE system, which offering a powerful tool for analytical sensing applications.<sup>114</sup> Furthermore, the variety of ECL luminophores and detector devices including PMT (photomultiplier tube), CCD (charge-coupled device), smart cell phones, makes BPE-ECL system attracts great attention in sensing platforms.<sup>115</sup> For example, Seol Baek, etc.<sup>116</sup> reported a miniaturized reverse electro dialysis-powered biosensor using ECL on bipolar electrode to detect glucose and achieved a detection in the range of 0.5–10 mM by observing ECL emissions with naked eyes. Xu group<sup>117</sup> suggested a bipolar electrode based multicolor ECL biosensor for the visualized sensing of prostate-specific antigen (PSA) in human blood serum, as the emission color of concomitant electro-chemiluminophores is potential resolved, Ru(bpy)<sub>3</sub><sup>2+</sup> and [Ir(ppy)<sub>3</sub>] mixture were used as ECL emission and the cutoff values (4.0 and 10.0 ng/mL) of human PSA could be recognized with naked eyes by the green–yellow–red ECL emission changing.

#### 1.3.1.1 Detection of biomolecules

DNA and RNA sensing by bipolar electrochemistry plays an important role for genetic assays and diagnosis. For instance, an ultrasensitive wireless BPE-ECL protocol for detection of c-Myc mRNA in MCF-7 cells (breast cancer cell line) on a ITO (indium tin oxide) BPE presented.<sup>118</sup> Specifically, this method based on the modification of anodic pole of BPE with antisense DNA that as recognition element, RuSi@ Ru(bpy)<sub>3</sub><sup>2+</sup>(Ru(bpy)<sub>3</sub><sup>2+</sup>-conjugated silica nanoparticles) as signal emitter, which employs the hybridization- induced changes of ECL signal for the detection of reporter DNA, as illustrated in Figure 1.5, prior ECL detection, the CdSe@ZnS quantum dot-antisense DNA would conjugate with reporter DNA, followed by transfecting through the tube cell in which c-Myc mRNA would replace reporter DNA for its higher hybridization, the replaced reporter DNA would combine with antisense DNA that labelled with RuSi@ Ru(bpy)<sub>3</sub><sup>2+</sup> ECL

emitter and decrease the signal, and the reversely ECL signal is proportional with the concentration of c-Myc mRNA. Similarly, a paper-based Au-BPE ECL sensing platform for detection of miRNA-155 proposed.<sup>119</sup> As well as for the detection of pathogenic DNAs, different paper-based BPE configurations are fabricated and employed.<sup>120-121</sup> Moreover, to detect cancer cell, a visual ECL sensing platform based on dual-BPE array chip developed, specifically, the chip contains two BPEs and three reservoirs, which filled with buffer, luminol, and Ru(bpy)<sub>3</sub><sup>2+</sup>-TPrA solutions, respectively, by applying voltage, a set of orange ECL signals belongs to Ru(bpy)<sub>3</sub><sup>2+</sup> turned on, after adding DNAzyme and hydrogen peroxide to luminol and Ru(bpy)<sub>3</sub><sup>2+</sup> reservoirs, the orange signals would decrease until vanish by the quenching effect; meanwhile, the blue signals from luminol turned on due to reaction with H<sub>2</sub>O<sub>2</sub>; owing to H<sub>2</sub>O<sub>2</sub> could be formed by stimulating HL-60 cancer cells with PMA, and DNAzyme can be generated from extended primer DNA by telomerase, which also can be extracted from the cancer cells, based on this approach, the HL-60 cancer cell could be detected.<sup>122</sup>

In addition, antibodies or proteins from cells also have being widely detected using bipolar electrochemistry. To measure the cancer cell surface protein, a hybrid BPE ECL biosensor reported, prior to ECL measurement, anodic BPE modified with capture DNA, which would hybridize a ferrocene (Fc) labelled aptamer and lead to a very week ECL signal for Fc inhibiting the oxidation of Ru(bpy)<sub>3</sub><sup>2+</sup> and Fc<sup>+</sup> quenching the ECL efficiency,<sup>3</sup> however, when the Fc labeled aptamer mixed with cancer cells solution added to the cell, ECL signal would enhanced due to mucin-1 protein expressed on the surface of cancer cells (MCF-7) would combine with part of Fc-aptamer, using this principle, the mucin-1 protein on the surface of MCF-7 cells could be quantified.<sup>123</sup> In similar way, tetracycline,<sup>124</sup> folic acid,<sup>125</sup> adenosine aptamer,<sup>126</sup> prostate-sepcific-antigen (PSA),<sup>127</sup> and MCF-7 and A549 aptamers<sup>128</sup> were detected using BPE system. Moreover,

glucose concentration in blood also play a critical role for influencing human health, based on BPE technique, various of glucose detection approaches were reported.<sup>129-130</sup>

Cellular respiration can be monitored using conventional electrochemical techniques,<sup>131-132</sup> bipolar technique could also be used in measurement of cell respiratory activities.<sup>20</sup> During measurement, the oxygen would be reduced at the cathodic pole of BPE, while the luminophore would be oxidized at the anodic pole of BPE to produce ECL emission, therefore, the ECL intensity depends on oxygen concentration. For cell respiration, the cell aggregates were placed in the cathodic pole of BPE, and a low ECL signal would be obtained when the cell aggregates consumed the dissolved oxygen in the solution. Owing to this behavior, the cell respiratory activities could be monitored. In Similar way, the hydrogen peroxide from cells can also be detected.<sup>133</sup>

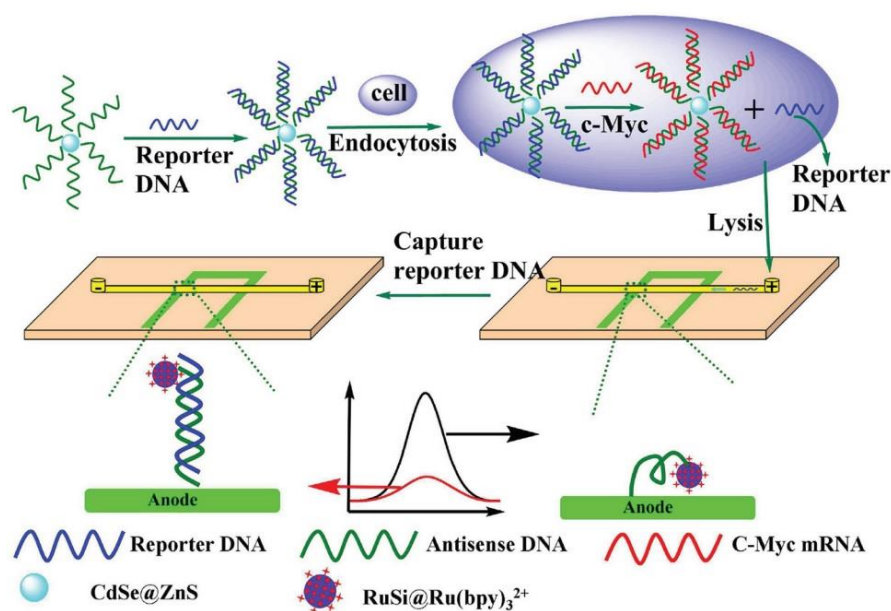


**Figure 1.5** Schematic representation of intracellular c-Myc mRNA detection using BPE- ECL biosensor.<sup>118</sup> Adapted permission from Copyright © 2012, American Chemical Society.

### 1.3.1.2 Others

Some compounds or ions have quenching effect for ECL happened at the vicinity surface of electrode, such as  $\text{Fc}^+$ ,<sup>123</sup> brilliant blue FCF,<sup>134</sup> ribavirin,<sup>135</sup> etc.. And this quenching phenomenon

could be considered as a quite general strategy for detecting molecules. In fact, this ECL quenching effect already combined with BPE for quencher molecules measurement. For example, small molecules, like ferrocene-methanol and oxygen, which are capable of efficiently quenching of the  $\text{Ru}(\text{bpy})_3^{2+}$  excited state via energy or electron transfer, detected in the bipolar electrochemical cell.<sup>136</sup> Halide ion turned out also have the ability to quench ECL signal on a critical threshold concentration,<sup>137</sup> which also could be measured using BPE ECL system.

### 1.3.2 Bipolar Electrochemistry in Materials Science

Bipolar electrochemistry widely used in materials science due to its interesting features including: 1) wireless nature of BPE, 2) gradient potential distribution, 3) availability of electrophoresis.<sup>16</sup>

#### 1.3.2.1 Gradient Material Synthesis

One of beneficial properties of BPEs is that they have an electrical potential gradient distribution, derived as linear IR drop in solution, and the slope could be manipulated by changing the applied voltage on the driving electrodes. Thus, it can be used for different applications.

##### (1) Gradient electrodeposition

By taking advantage of the potential gradient in the solution using bipolar chemistry through the interfacial polarization between a conducting substrate and an electrolyte solution, a metal density gradient or bimetallic alloy composition gradient can be achieved on the cathodic side of bipolar. To better understand of this, a model for Ag/Au alloy electrodeposition using linear sweep voltammetry showed in Figure 1.6, when the interfacial potential between the electrode and electrolyte solution reaches to the onset reduction potential of Ag ions, the Ag deposition starts, and the Ag reducing rate increases with the increasing of more negative potential until reaches an equilibrium states (constant value) that governs by the maximal mass migration and diffusion of

Ag ions; as the negative potential reaches the onset reduction potential of Au ions, the Au deposition starts and the reducing rate also increases with the increasing of more negative potential until reaches the equilibrium state of Au ions deposition, and the alloy composition region is located within the range, as illustrated of part II in Figure 1.6; part III is a region both Ag and Au reach their equilibrium states, which means the composition of Ag and Au stays at a constant value. All these three parts could be achieved by changing the potential along with BPE, which exhibits a potential gradient with the position of BPE. For example, Bouffier group<sup>138</sup> reported a straightforward, single-step generation of metal composition gradients on cylindrical carbon fibers by using bipolar chemistry. In specifically, they demonstrated with monometallic layers as well as a bimetallic composite layer based on copper and nickel on BPE, and screened the morphologies of different metal depositions along a BPE by using SEM. In our previous work, we have successfully formed CdS on Au substrate<sup>139</sup> and Au-Ag alloy gradient on stainless steel by using bipolar electrodeposition, a technique based on the existence of a potential gradient at the interface of a BPE and an electrolytic solution.<sup>140</sup>

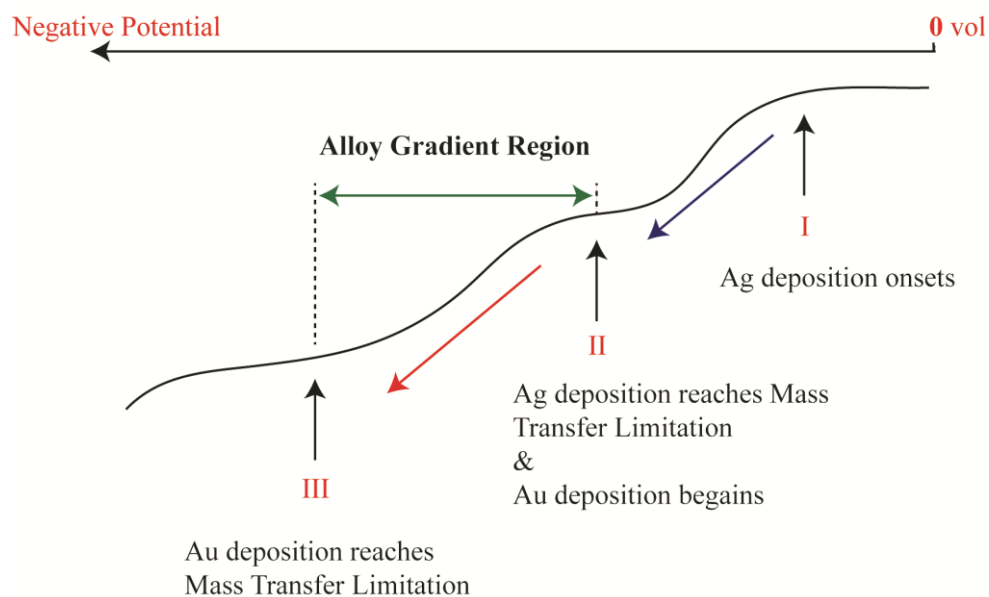


**Figure 1.6** Ag/Au alloy electrodeposition model.

## (2) Fabrication of gradient polymer brushes

Once we digest the gradient electrodeposition principle, it would be much easy to understand the fabrication of gradient polymer brushes. One way to fabricate the gradient polymer brushes is electrochemically generated Cu(I) used as the catalyst of ATRP (atom-transfer radical polymerization), in the electrochemically mediated ATRP (eATRP), the living radical polymerization can be controlled by tuning the potential gradient, and polymerization rate of ATRP is generally proportional to the ratio of  $[Cu(I)]/[Cu(II)]$ , therefore, the polymerization rate can be tuned by changing this ratio, under the BPE conditions, generation of Cu(I) is increasing as position varies close to the cathodic edge, consequently, the gradient of  $[Cu(I)]/[Cu(II)]$  is established in the space within the micro-gap. Therefore, the rate of surface initiated ATRP depends on the BPE positions to give a polymer brush with a gradient height profile.<sup>19, 141</sup> In another study, Kuhn and co-workers employed electro-polymerization using BPE technique for poly-pyrrole deposition.<sup>142</sup> Also, they achieved deposits of Au at the cathodic end of BPE (carbon microfiber) along with a concomitant electro-polymerization of polythiophene at the anodic BPE pole.<sup>143</sup>

## (3) others

Electron transfer reactions of a conducting polymer generate polaron or bi-polaron in its repeating unit (known as electrochemical doping), which vary the physical properties of polymers. The electrochemical doping imparts electrical conductivity along with a significant color difference.<sup>144</sup>

### 1.3.2.2 Modification of Conductive Objects

One neat example about modification of conductive objects is using bipolar electrochemistry to synthesize Janus particles, where one hemisphere has a distinct property to the other side.<sup>145-146</sup>

BPEs were used carbon beads, and the key point of this technique is to fix BPEs in an electrolyte to suppress BPEs movement during electrolysis. Agarose-based hydrogel was found to be useful and used for fixing carbon beads in a glass capillary. Based on this concept, the modification of SiO<sub>2</sub> and TiO<sub>2</sub> reported by electrogenerated acid-induced sol–gel reaction,<sup>147</sup> the introduction of covalently bonded organic groups via the diazonium salts electro-grafting and metal deposition.<sup>146</sup>

Janus particles generated by bipolar electrodeposition containing a catalytic or a magnetic extremity can be used as synthetic motors. For example, carbon microtubes with an electrochemically generated Pt tip on one side have been moved in hydrogen peroxide solutions.<sup>148</sup> The motion was contributed to the generation and releasing of oxygen bubbles, which come from the catalytic decomposition of hydrogen peroxide at the Pt surface.

A direct electric connection between two separated BPEs can be achieved using bipolar electrochemistry. Bradley and co-workers demonstrated that two separated Cu particles that considered as BPEs could electrically contact by directional growth of Cu microwires. Initially, the faradaic processes at both Cu particles would cause electro-dissolution of Cu at anodic poles and water reduction at the cathodic poles, when the electrogenerated copper ions reach the cathodic side of the other particle, electrodeposition of Cu would happen and Cu dendrites would be formed.<sup>149-151</sup>

### 1.3.3 Other Fields

Bipolar electrochemistry is also using in analytical purpose including separation,<sup>152</sup> electric field focusing,<sup>153</sup> pre-concentration<sup>154</sup>, batteries,<sup>155-156</sup> and so on. One of the interesting applications of bipolar electrochemistry is used for seawater desalination, specifically, a flow of seawater is separated into desalted and brine water streams at the junction of a branched microchannel where a BPE placed, the anodic pole of the BPE produces an ion depletion zone,



and thus, a local electric field gradient redirects ions present in seawater to the brine channel.<sup>157</sup>

Undoubtedly, bipolar electrochemistry is a powerful tool employed in a great variety of fields.

## References

1. Loget, G.; Zigah, D.; Bouffier, L.; Sojic, N.; Kuhn, A., Bipolar electrochemistry: from materials science to motion and beyond. *Accounts of Chemical Research* **2013**, *46* (11), 2513-2523.
2. Phuakkong, O.; Sentic, M.; Li, H.; Warakulwit, C.; Limtrakul, J.; Sojic, N.; Kuhn, A.; Ravaine, V. r.; Zigah, D., Wireless synthesis and activation of electrochemiluminescent thermoresponsive janus objects using bipolar electrochemistry. *Langmuir* **2016**, *32* (49), 12995-13002.
3. Qi, Z.; You, S.; Liu, R.; Chuah, C. J., Performance and mechanistic study on electrocoagulation process for municipal wastewater treatment based on horizontal bipolar electrodes. *Frontiers of Environmental Science & Engineering* **2020**, *14* (3), 1-10.
4. Lacina, K.; Kazda, T.; Srový, T.; Trnková, L.; Vanýsek, P.; Skládal, P., Asymmetric bipolar electrochemistry: Detailed empirical description and determination of output characteristics of a galvanic system with multiple short-circuited cells in one electrolyte. *Electrochimica Acta* **2019**, *307*, 269-274.
5. Shannon, C.; Wang, B.; Yu, S., Reduction of 4-Nitrothiophenol on Ag/Au Bimetallic Alloy Surfaces Studied Using Bipolar Raman Spectroelectrochemistry. *ChemElectroChem* **2020**.
6. Sheridan, E.; Hlushkou, D.; Knust, K. N.; Tallarek, U.; Crooks, R. M., Enrichment of cations via bipolar electrode focusing. *Analytical chemistry* **2012**, *84* (17), 7393-7399.
7. Rafatmah, E.; Hemmateenejad, B., Colorimetric and visual determination of hydrogen peroxide and glucose by applying paper-based closed bipolar electrochemistry. *Microchimica Acta* **2019**, *186* (11), 684.
8. Kumsapaya, C.; Limtrakul, J.; Kuhn, A.; Zigah, D.; Warakulwit, C., Bipolar electrografting on the inner wall of carbon nanotubes. *ChemElectroChem* **2016**, *3* (3), 410-414.

9. Fosdick, S. E.; Crooks, R. M., Bipolar electrodes for rapid screening of electrocatalysts. *Journal of the American Chemical Society* **2012**, *134* (2), 863-866.
10. Ibañez, D.; Heras, A.; Colina, A., Bipolar Spectroelectrochemistry. *Analytical Chemistry* **2017**, *89* (7), 3879-3883.
11. Bouffier, L.; Arbault, S.; Kuhn, A.; Sojic, N., Generation of electrochemiluminescence at bipolar electrodes: concepts and applications. *Analytical and bioanalytical chemistry* **2016**, *408* (25), 7003-7011.
12. Crooks, R. M., Principles of bipolar electrochemistry. *ChemElectroChem* **2016**, *3* (3), 357-359.
13. Mavré, F.; Chow, K.-F.; Sheridan, E.; Chang, B.-Y.; Crooks, J. A.; Crooks, R. M., A theoretical and experimental framework for understanding electrogenerated chemiluminescence (ECL) emission at bipolar electrodes. *Analytical Chemistry* **2009**, *81* (15), 6218-6225.
14. Mavré, F. o.; Anand, R. K.; Laws, D. R.; Chow, K.-F.; Chang, B.-Y.; Crooks, J. A.; Crooks, R. M., Bipolar electrodes: a useful tool for concentration, separation, and detection of analytes in microelectrochemical systems. ACS Publications: 2010.
15. Fosdick, S. E.; Knust, K. N.; Scida, K.; Crooks, R. M., Bipolar electrochemistry. *Angewandte Chemie International Edition* **2013**, *52* (40), 10438-10456.
16. Shida, N.; Zhou, Y.; Inagi, S., Bipolar Electrochemistry: A Powerful Tool for Electrifying Functional Material Synthesis. *Accounts of Chemical Research* **2019**, *52* (9), 2598-2608.
17. Fosdick, S. E.; Crooks, J. A.; Chang, B.-Y.; Crooks, R. M., Two-dimensional bipolar electrochemistry. *Journal of the American Chemical Society* **2010**, *132* (27), 9226-9227.

18. Shida, N.; Kitamura, F.; Fuchigami, T.; Tomita, I.; Inagi, S., Signal-Amplified Analysis of Molecular Layers Prepared through Bipolar Electrochemistry. *ChemElectroChem* **2016**, *3* (3), 465-471.
19. Shida, N.; Koizumi, Y.; Nishiyama, H.; Tomita, I.; Inagi, S., Electrochemically mediated atom transfer radical polymerization from a substrate surface manipulated by bipolar electrolysis: Fabrication of gradient and patterned polymer brushes. *Angewandte Chemie International Edition* **2015**, *54* (13), 3922-3926.
20. Ino, K.; Yaegaki, R.; Hiramoto, K.; Nashimoto, Y.; Shiku, H., Closed bipolar electrode array for on-chip analysis of cellular respiration by cell aggregates. *ACS sensors* **2020**, *5* (3), 740-745.
21. Hai-Juan, L.; Shuang, H.; Lian-Zhe, H.; Guo-Bao, X., Progress in Ru (bpy) 32+ Electrogenerated Chemiluminescence. *Chinese Journal of Analytical Chemistry* **2009**, *37* (11), 1557-1565.
22. Hesari, M.; Ding, Z., Electrogenerated chemiluminescence: light years ahead. *Journal of The Electrochemical Society* **2015**, *163* (4), H3116.
23. Bard, A. J., *Electrogenerated chemiluminescence*. CRC Press: 2004.
24. Bouffier, L.; Sojic, N., Introduction and Overview of Electrogenerated Chemiluminescence. **2019**.
25. Qi, H.; Zhang, C., *Electrogenerated chemiluminescence biosensing*. ACS Publications: 2020.
26. Deng, B.; Lu, H.; Li, L.; Shi, A.; Kang, Y.; Xu, Q., Determination of the number of binding sites and binding constant between diltiazem hydrochloride and human serum albumin by

ultrasonic microdialysis coupled with online capillary electrophoresis electrochemiluminescence. *Journal of Chromatography A* **2010**, *1217* (28), 4753-4756.

27. Ji, Y.; Ma, Y.; Sun, X., Determination of glutathione in individual Ramos cells by capillary electrophoresis with electrochemiluminescence detection. *Analytical Methods* **2013**, *5* (6), 1542-1547.

28. Cai, C.; Cheng, H.; Wang, Y., Determination of pretilachlor in soil and rice using matrix solid-phase dispersion extraction by capillary electrophoresis with field amplified sample injection and electrochemiluminescence detection. *Analytical Methods* **2014**, *6* (8), 2767-2773.

29. An, D.; Chen, Z.; Zheng, J.; Chen, S.; Wang, L.; Huang, Z.; Weng, L., Determination of biogenic amines in oysters by capillary electrophoresis coupled with electrochemiluminescence. *Food chemistry* **2015**, *168*, 1-6.

30. Lahuerta-Zamora, L.; Mellado-Romero, A. M., Video approach to chemiluminescence detection using a low-cost complementary metal oxide semiconductor (CMOS)-based camera: determination of paracetamol in pharmaceutical formulations. *Analytical and bioanalytical chemistry* **2017**, *409* (15), 3891-3898.

31. Xu, L.; Li, L.; Huang, J.; You, T., Analysis of perphenazine and fluphenazine by capillary electrophoresis coupled with tris (2, 2'-bipyridyl) ruthenium (II) electrochemiluminescence detection. *Talanta* **2014**, *118*, 1-6.

32. Deng, B.; Liu, Y.; Yin, H.; Ning, X.; Lu, H.; Ye, L.; Xu, Q., Determination of ultra-trace formaldehyde in air using ammonium sulfate as derivatization reagent and capillary electrophoresis coupled with on-line electrochemiluminescence detection. *Talanta* **2012**, *91*, 128-133.

33. Yao, J.; Li, L.; Li, P.; Yang, M., Quantum dots: from fluorescence to chemiluminescence, bioluminescence, electrochemiluminescence, and electrochemistry. *Nanoscale* **2017**, *9* (36), 13364-13383.
34. Lara, F. J.; Airado-Rodríguez, D.; Moreno-González, D.; Huertas-Pérez, J. F.; García-Campaña, A. M., Applications of capillary electrophoresis with chemiluminescence detection in clinical, environmental and food analysis. A review. *Analytica Chimica Acta* **2016**, *913*, 22-40.
35. Dufford, R.; Nightingale, D.; Gaddum, L., Luminescence of Grignard compounds in electric and magnetic fields, and related electrical phenomena. *Journal of the American Chemical Society* **1927**, *49* (8), 1858-1864.
36. Harvey, N., Luminescence during electrolysis. *The Journal of Physical Chemistry* **1929**, *33* (10), 1456-1459.
37. Hercules, D. M., Chemiluminescence resulting from electrochemically generated species. *Science* **1964**, *145* (3634), 808-809.
38. Visco, R. E.; Chandross, E. A., Electroluminescence in solutions of aromatic hydrocarbons. *Journal of the American Chemical Society* **1964**, *86* (23), 5350-5351.
39. Santhanam, K.; Bard, A. J., Chemiluminescence of electrogenerated 9, 10-Diphenylanthracene anion radical. *Journal of the American Chemical Society* **1965**, *87* (1), 139-140.
40. Leland, J. K.; Powell, M. J., Electrogenerated chemiluminescence: an oxidative-reduction type ECL reaction sequence using tripropyl amine. *Journal of the Electrochemical Society* **1990**, *137* (10), 3127.
41. Richter, M. M., Electrochemiluminescence (ecl). *Chemical Reviews* **2004**, *104* (6), 3003-3036.

42. Tokel, N. E.; Bard, A. J., Electrogenerated chemiluminescence. IX. Electrochemistry and emission from systems containing tris (2, 2'-bipyridine) ruthenium (II) dichloride. *Journal of the American Chemical Society* **1972**, *94* (8), 2862-2863.
43. Bezman, R.; Faulkner, L. R., Mechanisms of chemiluminescent electron-transfer reactions. V. Absolute measurements of rubrene luminescence in benzonitrile and N, N-dimethylformamide. *Journal of the American Chemical Society* **1972**, *94* (18), 6324-6330.
44. Maricle, D. L.; Maurer, A., Pre-annihilation electrochemiluminescence of rubrene. *Journal of the American Chemical Society* **1967**, *89* (1), 188-189.
45. Miao, W.; Choi, J.-P.; Bard, A. J., Electrogenerated chemiluminescence 69: The Tris (2, 2'-bipyridine) ruthenium (II),(Ru (bpy)  $32+$ )/Tri-n-propylamine (TPrA) system revisited A new route involving TPrA $\bullet+$  Cation Radicals. *Journal of the American Chemical Society* **2002**, *124* (48), 14478-14485.
46. Crusier, S. A.; Bard, A. J., Electrogenerated chemiluminescence. III. Intensity-time and concentration-intensity relation and the lifetime of radical cations of aromatic hydrocarbons in N, N-dimethylformamide solution. *Journal of the American Chemical Society* **1969**, *91* (2), 267-275.
47. Chang, M.-M.; Saji, T.; Bard, A. J., Electrogenerated chemiluminescence. 30. Electrochemical oxidation of oxalate ion in the presence of luminescers in acetonitrile solutions. *Journal of the American Chemical Society* **1977**, *99* (16), 5399-5403.
48. Rubinstein, I.; Bard, A. J., Polymer films on electrodes. 4. Nafion-coated electrodes and electrogenerated chemiluminescence of surface-attached tris (2, 2'-bipyridine) ruthenium (2+). *Journal of the American Chemical Society* **1980**, *102* (21), 6641-6642.

49. Ege, D.; Becker, W. G.; Bard, A. J., Electrogenerated chemiluminescent determination of tris (2, 2'-bipyridine) ruthenium ion (Ru(bpy)<sub>3</sub><sup>2+</sup>) at low levels. *Analytical chemistry* **1984**, *56* (13), 2413-2417.
50. Liu, X.; Shi, L.; Niu, W.; Li, H.; Xu, G., Environmentally Friendly and Highly Sensitive Ruthenium (II) Tris (2, 2'-bipyridyl) Electrochemiluminescent System Using 2-(Dibutylamino) ethanol as Co-Reactant. *Angewandte Chemie International Edition* **2007**, *46* (3), 421-424.
51. White, H. S.; Bard, A. J., Electrogenerated chemiluminescence. 41. Electrogenerated chemiluminescence and chemiluminescence of the Ru (2, 2'-bpy) <sup>2+</sup>-S<sub>2</sub>O<sub>8</sub><sup>2-</sup>-system in acetonitrile-water solutions. *Journal of the American Chemical Society* **1982**, *104* (25), 6891-6895.
52. Bolleta, F.; Ciano, M.; Balzani, V.; Serpone, N., Polypyridine transition metal complexes as light emission sensitizers in the electrochemical reduction of the persulfate ion. *Inorganica Chimica Acta* **1982**, *62*, 207-213.
53. Gorman, B. A.; Francis, P. S.; Barnett, N. W., Tris (2, 2'-bipyridyl) ruthenium (II) chemiluminescence. *Analyst* **2006**, *131* (5), 616-639.
54. Kulmala, S.; Ala-Kleme, T.; Heikkilä, L.; Väre, L., Energetic electrochemiluminescence of (9-fluorenyl) methanol induced by injection of hot electrons into aqueous electrolyte solution. *Journal of the Chemical Society, Faraday Transactions* **1997**, *93* (17), 3107-3113.
55. Gaillard, F.; Sung, Y.-E.; Bard, A. J., Hot electron generation in aqueous solution at oxide-covered tantalum electrodes. Reduction of methylpyridinium and electrogenerated chemiluminescence of Ru (bpy) <sup>2+</sup>. *The Journal of Physical Chemistry B* **1999**, *103* (4), 667-674.
56. Knight, A. W.; Greenway, G. M., Electrogenerated chemiluminescent determination of pyruvate using tris (2, 2'-bipyridine) ruthenium (II). *Analyst* **1995**, *120* (10), 2543-2547.



57. Marquette, C. A.; Blum, L. J., Electro-chemiluminescent biosensing. *Analytical and Bioanalytical Chemistry* **2008**, *390* (1), 155-168.
58. Gross, E.; Anderson, J.; Slaterbeck, A.; Thayumanavan, S.; Barlow, S.; Zhang, Y.; Marder, S.; Hall, H.; Nabor, M. F.; Wang, J.-F., Electrogenerated chemiluminescence from derivatives of aluminum quinolate and quinacridones: Cross-reactions with triarylamine lead to singlet emission through triplet-triplet annihilation pathways. *Journal of the American Chemical Society* **2000**, *122* (20), 4972-4979.
59. Taverna, P. J.; Mayfield, H.; Andrews, A. R., Determination of cadmium ions in water by a novel electrochemiluminescence method. *Analytica chimica acta* **1998**, *373* (2-3), 111-117.
60. Vogler, A.; Kunkely, H., Electrochemiluminescence of organometallics and other transition metal complexes. ACS Publications: 1987.
61. Richter, M. M.; Bard, A. J., Electrogenerated chemiluminescence. 58. Ligand-sensitized electrogenerated chemiluminescence in europium labels. *Analytical chemistry* **1996**, *68* (15), 2641-2650.
62. Bruno, J. G.; Cornette, J. C., An Electrochemiluminescence Assay Based on the Interaction of Diaminotoluene Isomers with Gold (I) and Copper (II) Ions. *Microchemical journal* **1997**, *56* (3), 305-314.
63. Fleet, B.; Kirkbright, G.; Pickford, C., Application of electroluminescence techniques to the determination of aromatic hydrocarbons. *Talanta* **1968**, *15* (6), 566-570.
64. Abruña, H. D., Electrogenerated chemiluminescence of bipyridine and phenanthroline complexes of osmium. *Journal of electroanalytical chemistry and interfacial electrochemistry* **1984**, *175* (1-2), 321-326.

65. Ouyang, J.; Zietlow, T. C.; Hopkins, M. D.; Fant, F. R. F.; Gray, H. B.; Bard, A. J., Electrochemistry and electrogenerated chemiluminescence of tetrachlorotetrakis (trimethylphosphine) dimolybdenum. *The Journal of Physical Chemistry* **1986**, *90* (16), 3841-3844.
66. Bonafede, S.; Ciano, M.; Bolletta, F.; Balzani, V.; Chassot, L.; Von Zelewsky, A., Electrogenerated chemiluminescence of an ortho-metalated platinum (II) complex. *The Journal of Physical Chemistry* **1986**, *90* (16), 3836-3841.
67. Richter, M. M.; Debad, J. D.; Striplin, D. R.; Crosby, G.; Bard, A. J., Electrogenerated chemiluminescence. 59. Rhenium complexes. *Analytical Chemistry* **1996**, *68* (24), 4370-4376.
68. Richter, M. M.; Bard, A. J.; Kim, W.; Schmehl, R. H., Electrogenerated chemiluminescence. 62. Enhanced ECL in bimetallic assemblies with ligands that bridge isolated chromophores. *Analytical Chemistry* **1998**, *70* (2), 310-318.
69. Bruno, J. G.; Parker, J. E.; Holwitt, E.; Alls, J. L.; Kiel, J. L., Preliminary electrochemiluminescence studies of metal ion–bacterial diazolumelanin (DALM) interactions. *Journal of bioluminescence and chemiluminescence* **1998**, *13* (3), 117-123.
70. Luttmer, J.; Bard, A. J., Electrogenerated chemiluminescence. 38. Emission intensity-time transients in the tris (2, 2'-bipyridine) ruthenium (II) system. *The Journal of Physical Chemistry* **1981**, *85* (9), 1155-1159.
71. Glass, R. S.; Faulkner, L. R., Electrogenerated chemiluminescence from the tris (2, 2'-bipyridine) ruthenium (II) system. An example of S-route behavior. *The Journal of Physical Chemistry* **1981**, *85* (9), 1160-1165.
72. Bard, A. J.; Whitesides, G. M., Luminescent metal chelate labels and means for detection. Google Patents: 1993.

73. Zhou, X.; Zhu, D.; Liao, Y.; Liu, W.; Liu, H.; Ma, Z.; Xing, D., Synthesis, labeling and bioanalytical applications of a tris (2, 2'-bipyridyl) ruthenium (II)-based electrochemiluminescence probe. *nature protocols* **2014**, 9 (5), 1146-1159.
74. Dennany, L.; Forster, R. J.; Rusling, J. F., Simultaneous direct electrochemiluminescence and catalytic voltammetry detection of DNA in ultrathin films. *Journal of the American Chemical Society* **2003**, 125 (17), 5213-5218.
75. Miao, W.; Bard, A. J., Electrogenerated Chemiluminescence. 72. Determination of Immobilized DNA and C-Reactive Protein on Au (111) Electrodes Using Tris (2, 2'-bipyridyl) ruthenium (II) Labels. *Analytical chemistry* **2003**, 75 (21), 5825-5834.
76. Schaper, H., A novel hybrid detection system based on electrochemiluminescence in electrolyte-free solutions. *Journal of Electroanalytical Chemistry and Interfacial Electrochemistry* **1981**, 129 (1-2), 335-342.
77. Brina, R.; Bard, A. J., Electrogenerated chemiluminescence: Part XLVIII. Electrochemistry and electrogenerated chemiluminescence of bis (2, 4, 6-trichlorophenyl) oxalate-luminescer systems. *Journal of electroanalytical chemistry and interfacial electrochemistry* **1987**, 238 (1-2), 277-295.
78. Debad, J. D.; Morris, J. C.; Magnus, P.; Bard, A. J., Anodic coupling of diphenylbenzo [k] fluoranthene: Mechanistic and kinetic studies utilizing cyclic voltammetry and electrogenerated chemiluminescence. *The Journal of organic chemistry* **1997**, 62 (3), 530-537.
79. Sheng, Y.; Yang, H.; Wang, Y.; Han, L.; Zhao, Y.; Fan, A., Silver nanoclusters-catalyzed luminol chemiluminescence for hydrogen peroxide and uric acid detection. *Talanta* **2017**, 166, 268-274.

80. Karasawa, K.; Haraya, S.; Okubo, S.; Arakawa, H., Novel assay of antibacterial components in manuka honey using lucigenin-chemiluminescence-HPLC. *Analytica chimica acta* **2017**, *954*, 151-158.
81. Prieto, I.; Teetsov, J.; Fox, M. A.; Vanden Bout, D. A.; Bard, A. J., A study of excimer emission in solutions of poly (9, 9-dioctylfluorene) using electrogenerated chemiluminescence. *The Journal of Physical Chemistry A* **2001**, *105* (3), 520-523.
82. Strauß, J.; Daub, J., Donor–Acceptor Functionalized Luminescent Hairpin Peptides: Electrochemiluminescence of Pyrene/Phenothiazine-Substituted Optically Active Systems. *Advanced Materials* **2002**, *14* (22), 1652-1655.
83. Lee, S. K.; Richter, M. M.; Streckowski, L.; Bard, A. J., Electrogenerated chemiluminescence. 61. Near-IR electrogenerated chemiluminescence, electrochemistry, and spectroscopic properties of a heptamethine cyanine dye in MeCN. *Analytical Chemistry* **1997**, *69* (20), 4126-4133.
84. Hasegawa, T.; Mattenberger, K.; Takeya, J.; Batlogg, B., Ambipolar field-effect carrier injections in organic Mott insulators. *Physical Review B* **2004**, *69* (24), 245115.
85. Rodríguez-López, J.; Shen, M.; Nepomnyashchii, A. B.; Bard, A. J., Scanning electrochemical microscopy study of ion annihilation electrogenerated chemiluminescence of rubrene and [Ru (bpy) <sub>3</sub>] <sup>2+</sup>. *Journal of the American Chemical Society* **2012**, *134* (22), 9240-9250.
86. Chen, G. N.; Lin, R. E.; Zhao, Z. F.; Duan, J. P.; Zhang, L., Electrogenerated chemiluminescence for determination of indole and tryptophan. *Analytica chimica acta* **1997**, *341* (2-3), 251-256.

87. Wang, Y.-Z.; Hao, N.; Feng, Q.-M.; Shi, H.-W.; Xu, J.-J.; Chen, H.-Y., A ratiometric electrochemiluminescence detection for cancer cells using g-C<sub>3</sub>N<sub>4</sub> nanosheets and Ag-PAMAM-luminol nanocomposites. *Biosensors and Bioelectronics* **2016**, *77*, 76-82.
88. Wang, J.-X.; Zhuo, Y.; Zhou, Y.; Wang, H.-J.; Yuan, R.; Chai, Y.-Q., Ceria doped zinc oxide nanoflowers enhanced luminol-based electrochemiluminescence immunosensor for amyloid- $\beta$  detection. *ACS applied materials & interfaces* **2016**, *8* (20), 12968-12975.
89. Wilson, R.; Clavering, C.; Hutchinson, A., Electrochemiluminescence enzyme immunoassay for TNT. *Analyst* **2003**, *128* (5), 480-485.
90. Jimenez-Ruiz, A.; Grueso, E.; Perez-Tejeda, P.; Muriel-Delgado, F.; Torres-Marquez, C., Electrochemiluminescent (ECL)[Ru (bpy) <sub>3</sub>] <sup>2+</sup>/PAMAM dendrimer reactions: coreactant effect and 5-fluorouracil/dendrimer complex formation. *Analytical and bioanalytical chemistry* **2016**, *408* (25), 7213-7224.
91. Zhang, R.; Zhong, X.; Chen, A.-Y.; Liu, J.-L.; Li, S.-K.; Chai, Y.-Q.; Zhuo, Y.; Yuan, R., Novel Ru (bpy) <sub>2</sub> (cpaphen) <sup>2+</sup>/TPrA/TiO<sub>2</sub> ternary ECL system: an efficient platform for the detection of glutathione with Mn<sup>2+</sup> as substitute target. *Analytical Chemistry* **2019**, *91* (5), 3681-3686.
92. Tang, T.; Hao, Z.; Yang, H.; Nie, F.; Zhang, W., A highly enhanced electrochemiluminescence system based on a novel Cu-MOF and its application in the determination of ferrous ion. *Journal of Electroanalytical Chemistry* **2020**, *856*, 113498.
93. Tian, K.; Li, D.; Tang, T.; Nie, F.; Zhou, Y.; Du, J.; Zheng, J., A novel electrochemiluminescence resonance energy transfer system of luminol-graphene quantum dot composite and its application in H<sub>2</sub>O<sub>2</sub> detection. *Talanta* **2018**, *185*, 446-452.

94. Saqib, M.; Bashir, S.; Kitte, S. A.; Li, H.; Jin, Y., Acridine orange as a coreactant for efficient electrogenerated chemiluminescence of tris (2, 2'-bipyridine) ruthenium (ii) and its use in selective and sensitive detection of thiourea. *Chemical Communications* **2020**, *56* (38), 5154-5157.
95. Parveen, S.; Zhang, W.; Yuan, Y.; Hu, L.; Gilani, M. R. H. S.; ur Rehman, A.; Xu, G., Electrogenerated chemiluminescence of Ru (phen)  $32+/2-$ -(dibutylamino) ethanol system. *Journal of Electroanalytical Chemistry* **2013**, *688*, 45-48.
96. Cao, W.; Xu, G.; Zhang, Z.; Dong, S., Novel tris (2, 2'-bipyridine) ruthenium (ii) cathodic electrochemiluminescence in aqueous solution at a glassy carbon electrode. *Chemical communications* **2002**, (14), 1540-1541.
97. Swanick, K. N.; Ladouceur, S.; Zysman-Colman, E.; Ding, Z., Bright electrochemiluminescence of iridium (III) complexes. *Chemical Communications* **2012**, *48* (26), 3179-3181.
98. Backhurst, J.; Coulson, J.; Goodridge, F.; Plimley, R.; Fleischmann, M., A preliminary investigation of fluidized bed electrodes. *Journal of the Electrochemical Society* **1969**, *116* (11), 1600.
99. Manji, A.; Oloman, C., Electrosynthesis of propylene oxide in a bipolar trickle-bed reactor. *Journal of applied electrochemistry* **1987**, *17* (3), 532-544.
100. Wiesener, K.; Ohms, D.; Benczúr-Ürmössy, G.; Berthold, M.; Haschka, F., High power metal hydride bipolar battery. *Journal of Power Sources* **1999**, *84* (2), 248-258.
101. Cervera-March, S.; Smotkin, E.; Bard, A.; Campion, A.; Fox, M.; Mallouk, T.; Webber, S.; White, J., Modeling of bipolar semiconductor photoelectrode arrays for electrolytic processes. *Journal of the Electrochemical Society* **1988**, *135* (3), 567.

102. Arora, A.; Eijkel, J. C.; Morf, W. E.; Manz, A., A wireless electrochemiluminescence detector applied to direct and indirect detection for electrophoresis on a microfabricated glass device. *Analytical chemistry* **2001**, *73* (14), 3282-3288.
103. Zhan, W.; Alvarez, J.; Crooks, R. M., Electrochemical sensing in microfluidic systems using electrogenerated chemiluminescence as a photonic reporter of redox reactions. *Journal of the American Chemical Society* **2002**, *124* (44), 13265-13270.
104. Moghaddam, M. R.; Carrara, S.; Hogan, C. F., Multi-colour bipolar electrochemiluminescence for heavy metal ion detection. *Chemical Communications* **2019**, *55* (8), 1024-1027.
105. Dauphin, A. L.; Akchach, A.; Voci, S.; Kuhn, A.; Xu, G.; Bouffier, L.; Sojic, N., Tracking Magnetic Rotating Objects by Bipolar Electrochemiluminescence. *The journal of physical chemistry letters* **2019**, *10* (18), 5318-5324.
106. Zhang, X.; Shang, C.; Gu, W.; Xia, Y.; Li, J.; Wang, E., A renewable display platform based on the bipolar electrochromic electrode. *ChemElectroChem* **2016**, *3* (3), 383-386.
107. Xu, W.; Fu, K.; Bohn, P. W., Electrochromic sensor for multiplex detection of metabolites enabled by closed bipolar electrode coupling. *ACS sensors* **2017**, *2* (7), 1020-1026.
108. Hadjixenis, A. P.; Hrbac, J.; Prodromidis, M. I., Bipolar electrochemical detection of reducing compounds based on visual observation of a metal electrodeposited track at the onset driving voltage. *Sensors and Actuators B: Chemical* **2018**, *268*, 529-534.
109. Stefano, J. S.; Conzuelo, F.; Masa, J.; Munoz, R. A.; Schuhmann, W., Coupling electrochemistry with a fluorescence reporting reaction enabled by bipolar electrochemistry. *Journal of Electroanalytical Chemistry* **2020**, 113921.

110. Xu, W.; Ma, C.; Bohn, P. W., Coupling of independent electrochemical reactions and fluorescence at closed bipolar interdigitated electrode arrays. *ChemElectroChem* **2016**, *3* (3), 422-428.
111. Klett, O.; Nyholm, L., Separation high voltage field driven on-chip amperometric detection in capillary electrophoresis. *Analytical chemistry* **2003**, *75* (6), 1245-1250.
112. Zhang, X.; Chen, C.; Yin, J.; Han, Y.; Li, J.; Wang, E., Portable and visual electrochemical sensor based on the bipolar light emitting diode electrode. *Analytical chemistry* **2015**, *87* (9), 4612-4616.
113. Zhang, L.; Gupta, B.; Goudeau, B.; Mano, N.; Kuhn, A., Wireless electromechanical readout of chemical information. *Journal of the American Chemical Society* **2018**, *140* (45), 15501-15506.
114. WANG, J. L. E., Wireless ECL Generation Based on Bipolar Electrochemistry. *Analytical Electrogenerated Chemiluminescence: From Fundamentals to Bioassays* **2019**, *15*, 176.
115. Lu, H.-J.; Zhao, W.; Xu, J.-J.; Chen, H.-Y., Visual electrochemiluminescence ratiometry on bipolar electrode for bioanalysis. *Biosensors and Bioelectronics* **2018**, *102*, 624-630.
116. Baek, S.; Kwon, S.-R.; Yeon, S. Y.; Yoon, S.-H.; Kang, C. M.; Han, S. H.; Lee, D.; Chung, T. D., A Miniaturized Reverse Electrodialysis-Powered Biosensor Using Electrochemiluminescence on Bipolar Electrode. *Analytical chemistry* **2018**.
117. Wang, Y.-Z.; Xu, C.-H.; Zhao, W.; Guan, Q.-Y.; Chen, H.-Y.; Xu, J.-J., Bipolar Electrode Based Multicolor Electrochemiluminescence Biosensor. *Analytical chemistry* **2017**, *89* (15), 8050-8056.



118. Wu, M.-S.; Qian, G.-s.; Xu, J.-J.; Chen, H.-Y., Sensitive electrochemiluminescence detection of c-Myc mRNA in breast cancer cells on a wireless bipolar electrode. *Analytical chemistry* **2012**, *84* (12), 5407-5414.
119. Wang, F.; Fu, C.; Huang, C.; Li, N.; Wang, Y.; Ge, S.; Yu, J., based closed Au-Bipolar electrode electrochemiluminescence sensing platform for the detection of miRNA-155. *Biosensors and Bioelectronics* **2020**, *150*, 111917.
120. Feng, Q.; Chen, H.; Xu, J., Disposable paper-based bipolar electrode array for multiplexed electrochemiluminescence detection of pathogenic DNAs. *Science China Chemistry* **2015**, *58* (5), 810-818.
121. Liu, H.; Zhou, X.; Liu, W.; Yang, X.; Xing, D., based bipolar electrode electrochemiluminescence switch for label-free and sensitive genetic detection of pathogenic bacteria. *Analytical chemistry* **2016**, *88* (20), 10191-10197.
122. Zhang, H.-R.; Wang, Y.-Z.; Zhao, W.; Xu, J.-J.; Chen, H.-Y., Visual color-switch electrochemiluminescence biosensing of cancer cell based on multichannel bipolar electrode chip. *Analytical chemistry* **2016**, *88* (5), 2884-2890.
123. Wu, M.-S.; Yuan, D.-J.; Xu, J.-J.; Chen, H.-Y., Sensitive electrochemiluminescence biosensor based on Au-ITO hybrid bipolar electrode amplification system for cell surface protein detection. *Analytical chemistry* **2013**, *85* (24), 11960-11965.
124. Jin, L.; Qiao, J.; Chen, J.; Xu, N.; Wu, M., Combination of area controllable sensing surface and bipolar electrode-electrochemiluminescence approach for the detection of tetracycline. *Talanta* **2020**, *208*, 120404.
125. Wu, M. S.; Liu, Z.; Xu, J. J.; Chen, H. Y., Highly specific electrochemiluminescence detection of cancer cells with a closed bipolar electrode. *ChemElectroChem* **2016**, *3* (3), 429-435.

126. Shi, H.-W.; Wu, M.-S.; Du, Y.; Xu, J.-J.; Chen, H.-Y., Electrochemiluminescence aptasensor based on bipolar electrode for detection of adenosine in cancer cells. *Biosensors and Bioelectronics* **2014**, *55*, 459-463.
127. Wu, M.-S.; Yuan, D.-J.; Xu, J.-J.; Chen, H.-Y., Electrochemiluminescence on bipolar electrodes for visual bioanalysis. *Chemical Science* **2013**, *4* (3), 1182-1188.
128. Shi, H.-W.; Zhao, W.; Liu, Z.; Liu, X.-C.; Xu, J.-J.; Chen, H.-Y., Temporal sensing platform based on bipolar electrode for the ultrasensitive detection of cancer cells. *Analytical Chemistry* **2016**, *88* (17), 8795-8801.
129. Eßmann, V.; Jambrec, D.; Kuhn, A.; Schuhmann, W., Linking glucose oxidation to luminol-based electrochemiluminescence using bipolar electrochemistry. *Electrochemistry Communications* **2015**, *50*, 77-80.
130. Sentic, M.; Arbault, S.; Goudeau, B.; Manojlovic, D.; Kuhn, A.; Bouffier, L.; Sojic, N., Electrochemiluminescent swimmers for dynamic enzymatic sensing. *Chemical Communications* **2014**, *50* (71), 10202-10205.
131. Hiramoto, K.; Pai, H.-J.; Ino, K.; Nashimoto, Y.; Shiku, H., Electrochemical measurement of respiratory activity for evaluation of fibroblast spheroids containing endothelial cell networks. *Electrochimica Acta* **2020**, 135979.
132. Ino, K.; Onodera, T.; Kanno, Y.; Suda, A.; Kunikata, R.; Matsue, T.; Shiku, H., Electrochemicolor imaging of endogenous alkaline phosphatase and respiratory activities of mesenchymal stem cell aggregates in early-stage osteodifferentiation. *Electrochimica Acta* **2018**, *268*, 554-561.
133. Ge, S.; Zhao, J.; Wang, S.; Lan, F.; Yan, M.; Yu, J., Ultrasensitive electrochemiluminescence assay of tumor cells and evaluation of H<sub>2</sub>O<sub>2</sub> on a paper-based closed-

bipolar electrode by in-situ hybridization chain reaction amplification. *Biosensors and Bioelectronics* **2018**, *102*, 411-417.

134. Chen, X.; Yin, J.; Zhang, C.; Lu, N.; Chen, Z., Determination of Brilliant Blue FCF by a Novel Solid-state ECL Quenching Sensor of Ru (bpy)  $32+$ -poly (sulfosalicylic acid)/GCE. *Analytical Sciences* **2017**, *33* (10), 1123-1128.

135. Kong, D.; Liu, Y.; Wang, Z.; Jiang, L.; Cheng, J.; Xu, L.; Zhuang, Q.; Lu, C.-H.; Chi, Y.; Wei, Q.-h., Establishment of an electrochemiluminescence quenching method for ribavirin detection in Ru (bpy)  $32+$ /TEA system. *Journal of Electroanalytical Chemistry* **2017**, *801*, 1-6.

136. Wang, T.; Fan, S.; Erdmann, R.; Shannon, C., Detection of ferrocenemethanol and molecular oxygen based on electrogenerated chemiluminescence quenching at a bipolar electrode. *Langmuir* **2013**, *29* (51), 16040-16044.

137. Fan, S.; Shannon, C., Electrochemiluminescence quenching by halide ions at bipolar electrodes. *Electroanalysis* **2016**, *28* (3), 533-538.

138. Tisserant, G.; Gillion, J.; Lannelongue, J.; Fattah, Z.; Garrigue, P.; Roche, J.; Zigah, D.; Kuhn, A.; Bouffier, L., Single-Step Screening of the Potential Dependence of Metal Layer Morphologies along Bipolar Electrodes. *ChemElectroChem* **2016**, *3* (3), 387-391.

139. Ramakrishnan, S.; Shannon, C., Display of solid-state materials using bipolar electrochemistry. *Langmuir* **2010**, *26* (7), 4602-4606.

140. Ramaswamy, R.; Shannon, C., Screening the Optical Properties of Ag– Au Alloy Gradients Formed by Bipolar Electrodeposition Using Surface Enhanced Raman Spectroscopy. *Langmuir* **2010**, *27* (3), 878-881.

141. Magenau, A. J.; Strandwitz, N. C.; Gennaro, A.; Matyjaszewski, K., Electrochemically mediated atom transfer radical polymerization. *Science* **2011**, *332* (6025), 81-84.

142. Kong, S.; Fontaine, O.; Roche, J. r. m.; Bouffier, L.; Kuhn, A.; Zigah, D., Electropolymerization of polypyrrole by bipolar electrochemistry in an ionic liquid. *Langmuir* **2014**, *30* (11), 2973-2976.
143. Ongaro, M.; Gambirasi, A.; Favaro, M.; Kuhn, A.; Ugo, P., Asymmetrical modification of carbon microfibers by bipolar electrochemistry in acetonitrile. *Electrochimica Acta* **2014**, *116*, 421-428.
144. Beaujuge, P. M.; Reynolds, J. R., Color control in  $\pi$ -conjugated organic polymers for use in electrochromic devices. *Chemical reviews* **2010**, *110* (1), 268-320.
145. Loget, G.; Roche, J. r.; Gianessi, E.; Bouffier, L.; Kuhn, A., Indirect bipolar electrodeposition. *Journal of the American Chemical Society* **2012**, *134* (49), 20033-20036.
146. Loget, G.; Roche, J.; Kuhn, A., True bulk synthesis of Janus objects by bipolar electrochemistry. *Advanced materials* **2012**, *24* (37), 5111-5116.
147. Koizumi, Y.; Nishiyama, H.; Tomita, I.; Inagi, S., Templated bipolar electrolysis for fabrication of robust Co and Pt nanorods. *Chemical Communications* **2018**, *54* (74), 10475-10478.
148. Fattah, Z.; Loget, G.; Lapeyre, V.; Garrigue, P.; Warakulwit, C.; Limtrakul, J.; Bouffier, L.; Kuhn, A., Straightforward single-step generation of microswimmers by bipolar electrochemistry. *Electrochimica acta* **2011**, *56* (28), 10562-10566.
149. Bradley, J. C.; Crawford, J.; Ernazarova, K.; McGee, M.; Stephens, S. G., Wire formation on circuit boards using spatially coupled bipolar electrochemistry. *Advanced Materials* **1997**, *9* (15), 1168-1171.
150. Bradley, J.; Dengra, S.; Gonzalez, G.; Marshall, G.; Molina, F., Ion transport and deposit growth in spatially coupled bipolar electrochemistry. *Journal of Electroanalytical Chemistry* **1999**, *478* (1-2), 128-139.

151. Bradley, J.-C.; Babu, S.; Carroll, B.; Mittal, A., A study of spatially coupled bipolar electrochemistry on the sub-micrometer scale: colloidal particles on surfaces and cylinders in nuclear-track etched membranes. *Journal of Electroanalytical Chemistry* **2002**, *522* (1), 75-85.
152. Sheridan, E.; Knust, K. N.; Crooks, R. M., Bipolar electrode depletion: membraneless filtration of charged species using an electrogenerated electric field gradient. *Analyst* **2011**, *136* (20), 4134-4137.
153. Hlushkou, D.; Perdue, R. K.; Dhopeswarkar, R.; Crooks, R. M.; Tallarek, U., Electric field gradient focusing in microchannels with embedded bipolar electrode. *Lab on a Chip* **2009**, *9* (13), 1903-1913.
154. Anand, R. K.; Sheridan, E.; Hlushkou, D.; Tallarek, U.; Crooks, R. M., Bipolar electrode focusing: tuning the electric field gradient. *Lab on a chip* **2011**, *11* (3), 518-527.
155. Hagg, C. M.; Skyllas-Kazacos, M., Novel bipolar electrodes for battery applications. *Journal of applied electrochemistry* **2002**, *32* (10), 1063-1069.
156. Zhu, L.; Lei, A.; Cao, Y.; Ai, X.; Yang, H., An all-organic rechargeable battery using bipolar polyparaphenylene as a redox-active cathode and anode. *Chemical Communications* **2013**, *49* (6), 567-569.
157. Knust, K. N.; Hlushkou, D.; Anand, R. K.; Tallarek, U.; Crooks, R. M., Electrochemically mediated seawater desalination. *Angewandte Chemie* **2013**, *125* (31), 8265-8268.

## Chapter 2

### **Reduction of 4-nitrothiophenol on Ag/Au Bimetallic Alloy Surfaces Studied Using Bipolar Raman Spectroelectrochemistry**

#### **2.1 Introduction**

Spectroelectrochemical methods are widely used in analytical chemistry, materials science, and chemical biology/biophysics, and the field recently has been reviewed.<sup>1</sup> While this family of analytical methods encompasses a wide range of possible measurements, typically, voltammetry, amperometry or electrochemical impedance spectroscopy, are coupled with UV-vis, fluorescence, Fourier transform infrared (FTIR), or surface enhanced Raman spectroscopy (SERS) to acquire information-rich, multidimensional data sets.

Since its discovery in 1974, SERS has become a powerful and widely employed tool to study surface-mediated chemical processes due to its high sensitivity and selectivity.<sup>2-5</sup> In particular, the use of laser excitation allows SERS to be applied in diverse environments ranging from ultrahigh vacuum to the liquid-solid interface as well as to acquire spectroscopic data from local regions of interest on a surface.

Bipolar electrochemistry has attracted significant attention recently as a platform to study fundamental aspects of electron transfer<sup>6</sup>, electrodeposition<sup>7-8</sup>, and chemical sensing<sup>9-10</sup>. In a bipolar electrochemical circuit, the working electrode is interrogated using an externally applied voltage that generates a gradient of interfacial potential in one direction along the working electrode, providing a ‘snapshot’ of the system’s voltammetric behavior that can be read out using spectroscopic techniques.<sup>11</sup> Thus, leveraging the ability of Raman microscopy to probe local regions of the surface with the snapshot aspect of a bipolar circuit, makes the development of

bipolar Raman spectroelectrochemistry an obvious direction to expand the toolkit for surface analytical measurements (Figure 2.1).<sup>12</sup>

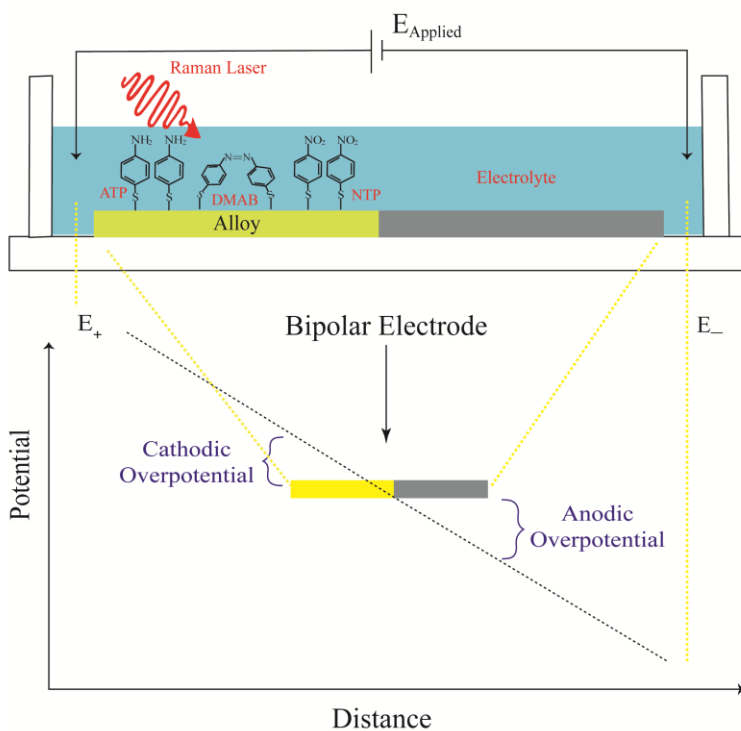


**Figure 2.1** Bipolar Raman spectroelectrochemistry. Spectral data can be acquired along the potential gradient and the spatial dimension normal to it. In this study, the alloy composition varies along the second dimension.

Bimetallic alloys are a category of materials in which two metals with different physical and chemical properties are combined, leading to enhanced or unique optical<sup>13</sup>, catalytic<sup>14</sup>, electronic<sup>15</sup>, and photochemical<sup>16</sup> behaviors. Noble metals, especially Au and Ag, can not only enhance Raman signal due to their plasmon resonance, but also act as catalysts<sup>17-20</sup> and are thus of interest as a testbed for developing bipolar Raman spectroelectrochemistry (BRSE). In general, Au particles with diameters smaller than 10 nm show remarkable catalytic activities but poor SERS, while diameters larger than 20 nm exhibit good SERS but poor catalytic activities. Silver particles provide stronger SERS signal than Au particles, but worse stability.<sup>21-23</sup> Therefore, researches on

SERS<sup>14, 24</sup> and catalysis<sup>25-27</sup> using the Au/Ag bimetallic synergistic effect have become widespread. Yin, et al.<sup>25</sup> synthesized hybrid Au–Ag alloy particles and nanochains (NCs) to better harvest visible light energy for selective hydrogenation reactions. The results show the conversion and turnover frequency (TOF) of individual Au/Ag particles with Au25 (25nm Au particles) cores, are approximately 8 and 10 times higher than those of Au25 particles. Crooks group<sup>28</sup> studied the catalytic activity trends of random PtAu and PdAu alloy dendrimer-encapsulated particles with an average size of ~1.6 nm towards allyl alcohol hydrogenation. Specifically, PtAu alloy particles had a linear increase in activity with increasing Pt ratio, while PdAu dendrimer-encapsulated particles show a maximum activity at a Pd composition of ~60%. This behavior was ascribed to the differences in H binding strength on the PtAu and PdAu alloy surfaces. Moreover, by taking advantage of the interfacial polarization under bipolar chemistry, a bimetallic alloy composition gradient can be achieved on the cathode side of the bipolar electrode (BPE). For example, the Bouffier group<sup>29</sup> reported a straightforward, single-step generation of metal composition gradients in both a monometallic layer and a bimetallic composite layer based on copper and nickel, on cylindrical carbon fibers using bipolar chemistry. In previous work, our group has successfully formed CdS on Au substrate<sup>30</sup> and Au-Ag alloy gradient on stainless steel under bipolar electrodeposition, exploiting the gradient of interfacial potential at the interface of the BPE and electrolytic solution.<sup>31</sup>

In this paper, we present a method for the real-time, *in situ* characterization of surface processes on electrode surfaces that employs Raman spectroscopy and a bipolar electrochemical circuit. Bimetallic alloy of Ag/Au with significant Raman enhancement is prepared first on the BPE surface with a surface gradient using a pre-bipolar electrochemical deposition. The electrochemical reduction of 4-nitrothiophenol (NTP) was used to demonstrate the feasibility of



this approach, because both the oxidized and reduced forms are Raman active. By using BRSE, the NTP reduction process on Ag/Au alloy surface could be detailed characterized with changing alloy composition and cathodic overpotential simultaneously in a 2D profile system. This real-time, in situ Raman characterization under bipolar electrochemistry enable the investigation of the dependence of electrochemical process on multiple parameters such as substrate composition, and applied potential, capable of rapid discovery of efficient electrocatalysts.

## 2.2 Experimental Section

### 2.2.1 Materials and Reagents

All solutions were prepared with deionized, ultra-pure water (VWR Type II). Stainless Steel foil (0.1mm, Alfa Aesar), Gold foil (0.1mm thick, 99.99% trace metals, Sigma-Aldrich), Silver nitrate (99.9+%, metals basis, Alfa Aesar), Potassium cyanide (97%, Sigma-Aldrich), Sodium hydroxide (98.4%, Fisher Scientific), Gold chloride ( $\text{HAuCl}_4 \cdot 3\text{H}_2\text{O}$ ) (VWR), 4-nitrothiophenol (80%, Alfa Aesar), Sodium perchlorate monohydrate ( $\geq 99.0\%$ , Fluka analytical), Potassium Chloride (crystals, BDH Chemicals), Potassium nitrate (99.7%, Fisher Scientific), Ethyl Alcohol (200 Proof, ACS/USP grade, Pharmco-Aaper), Potassium Ferricyanide(III) powder (99%, Sigma-Aldrich), Capillary tubes (I.D. 1.1-1.2 mm, Wall  $0.2 \pm 0.02$  mm, Kimble Chase), Silver wire (0.25mm diameter, 99.99%, Sigma-Aldrich), Potassium dicyanoargentate ( $\text{KAg}(\text{CN})_2$ , Sigma-Aldrich), Potassium dicyanoaurate(I) ( $\text{KAu}(\text{CN})_2$ , 98%, Sigma-Aldrich).

### 2.2.2 Preparation of Bipolar Electrochemical Cell Frames

Electrochemical cell frames were prepared using 3D-printer (MakerBot Replicator 2). As Figure 2.2 showed, three dimensions of (A) cell frame are 60 mm long  $\times$  72 mm wide (driving electrode width)  $\times$  10 mm deep, (B) cell frame are 60 mm long  $\times$  25 mm wide (driving electrode width)  $\times$  10 mm deep.

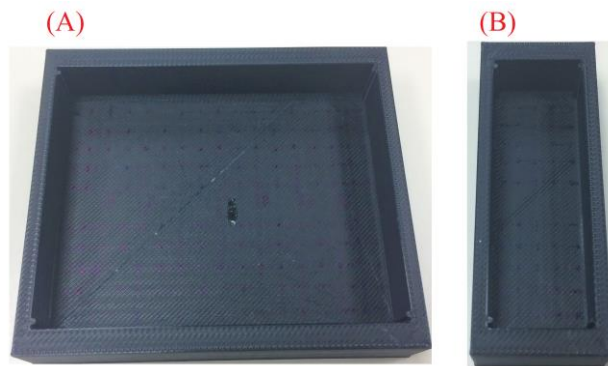


**Figure 2.2** Bipolar electrochemical cell frames. (A) cell frame used for electrodeposition; (B) cell frame used for Raman characterizing.

### 2.2.3 Self-made tiny Ag/AgCl Reference Electrodes for Solution Potential Measurement

To measure the solution potential more precisely, two tiny Ag/AgCl reference electrodes were prepared as measuring tips. The processes of making Ag/AgCl reference electrodes are as below:

Hydrogen flame was used to melt capillary tube into micrometer size hole, and it was cut according to the length required. Then it was filled with 1 M KCl solution. The oxidized silver wire was placed into it and sealed the top with tape. Prior to the preparation of the oxidized silver wire, first, the silver wire was slightly polished with sand paper (micro cut, 1200 grit, purchased from BUEHLER), then washed with deionized (D.I.) water and dried with stream of nitrogen, followed by dipping the silver wire into HNO<sub>3</sub> solution (assay 68%-70%, purchased from Pharmco-Aaper) for 2 mins, then it was cleaned with D.I. water and dried with stream of nitrogen. Using cyclic voltammetry in 1 M KCl solution (standard commercial Ag/AgCl electrode was used as reference electrode), the oxidation peak was observed, and then the oxidization peak potential was hold for 2-3 mins to oxidize the silver wire surface using Bulk Electrolysis method.

Self-made Ag/AgCl reference electrodes only used for measuring solution potential. All the experiments that involved three electrode systems were used standard commercial Ag/AgCl reference electrode.

## 2.2.4 Setup of Solution Potential Measurement

In order to study the solution potential distribution in the electrochemical cell, the bipolar solution potential differences located at the edges and middle across the BPE length was measured in cell B from Figure 2.2 using oscilloscope (Hantek DSO8060), 0.1 M NaClO<sub>4</sub> solution was used as electrolyte and applied 6V across the Au driving electrodes. The bipolar across length is 26 mm. Also, to study the stability of solution potential, the potential across 30 mm length in the middle of the bipolar cell was measured for close 2 hours under 6V across the bipolar cell.

## 2.2.5 Electrodeposition of Ag/Au on Stainless Steel Substrate Using Bipolar System

The bipolar cell frame used for the experiment is the frame (A) that is shown in Figure 2.2. Stainless steel was used as bipolar and driving electrodes that were pretreated by polishing with sandpaper and sonicated in alcohol solution (volume ratio of ethyl alcohol: water equals 1) for 5 mins, and finally washed with D.I. water and dried with the flow of nitrogen gas. The shape and the dimensions of BPE are shown in Figure 2.3(A). About half of the size covered with parafilm. Finally, it was placed in the middle of the bipolar cell.

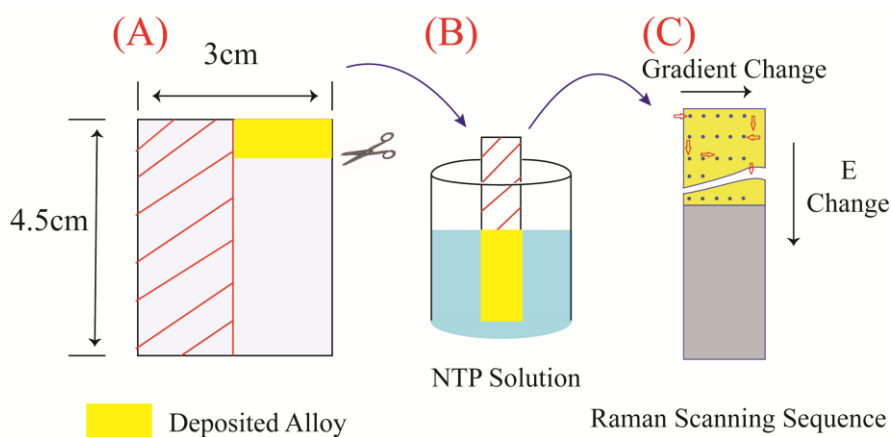


**Figure 2.3** (A) Electrodeposition Bipolar shape and dimension sizes, the red part covered with parafilm, (B) the cut new BPE with alloy side dipped in NTP solution to form self-assembled monolayer, (C) Raman scanning sequence of BPE cartoon.

Precursor solution for the deposition of Ag/Au alloy using 30 mM of  $HAuCl_4$  and 30 mM  $AgNO_3$  in 300 mM KCN solution and pH was adjusted to 12 using NaOH solution.

For electrodeposition, 6.5 V was applied to the driving electrodes for 3 mins.

#### 2.2.6 SEM-EDX Measurement

Scanning Electron Microscopy (SEM) images were collected using Joel JSM-7000f Field Emission Microscope and analyzed using EOS 7000F software package. EDX data were acquired using an Oxford X-Max energy dispersive X-ray spectrometer and were analyzed using the INCA software package.

#### 2.2.7 Setup of Bipolar Cell for Raman Spectroscopy

After electrodeposition of Ag/Au, the top electrodeposited part that has the Ag/Au gradient ratio was cut to form the new BPE for the Raman characterization. Prior to characterization by BRSE, the BPE was cut into a dimension of 26 mm long  $\times$  7 mm wide, and the side with the electrodeposited part dipped into 1 mM NTP solution, which was dissolved in ethyl alcohol, for 2 hours in the dark environment to form the self-assembled monolayer (The stainless-steel side covered with parafilm). Then the alloy part with NTP monolayer was washed with ethyl alcohol and DI water, respectively, and then dried with stream of nitrogen.

The BPE was placed such a way that the part covered by NTP was directed toward anodic driving electrode. The cell was filled with 0.1 M  $NaClO_4$  solution. Gold foils were used for driving electrodes. 6 V was applied and waited for about 12 mins. Then Raman scanning was started from the side edge part horizontally as 'S' sequence towards the middle part of the BPE, as shown in Figure 2.3(C). And the data collected under nitrogen environment. The distance between two adjacent scanning dots is 1 mm. Raman scanning was used 785nm (18 mW power was used for Raman measurement) output from a wavelength stabilized high power laser diode system (model

SDL – 8530, SDL Inc.). Raman measurement and analysis were performed using a Renishaw inVia Raman microscope system, and Raman signals were accumulated for 10 second.

## 2.3 Results and Discussion

### 2.3.1 Electrodeposition of Ag/Au Alloy on Stainless Steel BPE Substrate

In bipolar electrochemistry, a linear potential gradient will be generated in the solution across the cell under the influence of external electric field. The interfacial potential, notes as the potential difference between the solution and the BPE, is the driving force that leads to reduction or oxidation, respectively. Due to the solution potential difference, it will possess a certain value at each local position across the BPE, showing a varying overpotential for faradaic reaction. In the application of electrodeposition, the designed material would be deposited along the BPE cathode at different rate with continuous change in cathodic overpotential. In our experimental design, to have bimetallic Ag/Au alloy on the substrate, a co-depositing solution consisted of both Ag and Au anions should be prepared. The alloy gradient, with varying percentage ratio of Ag/Au along the cathode of BPE, can only be established by the presence of reduction potential separation in two different deposition reagents. For example, a co-depositing solution of  $KAg(CN)_2$  and  $KAu(CN)_2$  is not appropriate with similar reduction potentials. As illustrated in Figure 2.4, the reduction peak of Ag complex and Au complex ions are not distinguishable, which demonstrates the co-depositing solution of  $KAg(CN)_2$  and  $KAu(CN)_2$  is not a good selection to achieve Ag/Au alloy gradient. In addition to the reagent selection, the pH of deposition solution should be carefully controlled due to possible hydrogen evolution in aqueous solution would give rise to inconsistency on the alloy morphology and discontinuity of gradient distribution.

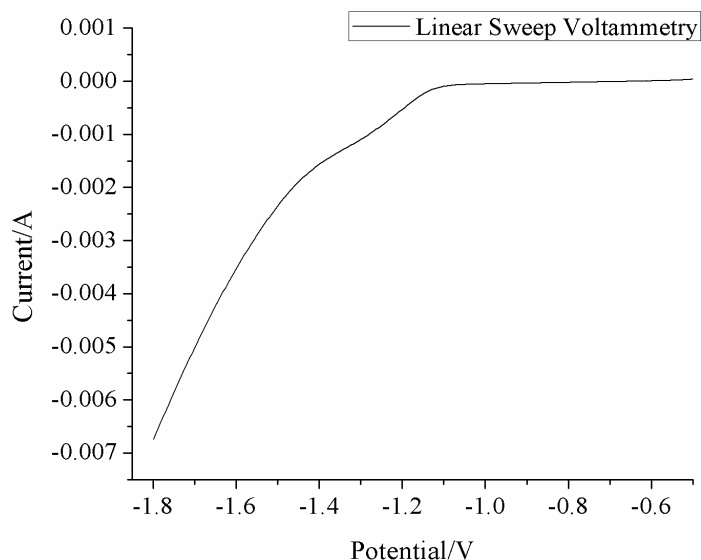


**Figure 2.4** Linear Sweep Voltammogram scanned in 10 mM  $\text{KAu}(\text{CN})_2$  and 10mM  $\text{KAg}(\text{CN})_2$  with 200mM KCN supporting electrolyte solution, pH=12. Ag/AgCl electrode as reference electrode, Pt grid as counter electrode, stainless-steel as working electrode, scan rate: 100mV/s.

$\text{HAuCl}_4$  and  $\text{AgNO}_3$  were finally selected as deposition reagent in KCN solution, with pH adjusted by 0.1 M NaOH to a value of 12 to avoid the generation of HCN during electrodeposition process. In the cyanide solution,  $\text{Ag}^+$  ions from  $\text{AgNO}_3$  would chelate with  $\text{CN}^-$  and form  $[\text{Ag}(\text{CN})_2]^-$  complex, while  $[\text{Au}(\text{Cl})_4]^-$ , from  $\text{HAuCl}_4$ , will undergo a ligand exchange reaction to form a new complex  $[\text{Au}(\text{CN})_4]^-$  as the result of their high formation constant by the substitution of  $\text{CN}^-$  to  $\text{Cl}^-$ . First, cyclic voltammetry was carried out by scanning the co-deposition solution with newly formed  $[\text{Au}(\text{CN})_4]^-$  and  $[\text{Ag}(\text{CN})_2]^-$  complex from -0.5 V to -1.6 V, at a scan rate of 50 mV/s. Pt grid was used as the counter electrode and standard Ag/AgCl electrode was used as reference electrode. As is shown in Figure 2.5(A), the reduction potential of  $[\text{Ag}(\text{CN})_2]^-$  locates at ca. -1.2 V, and the reduction potential of  $[\text{Au}(\text{CN})_4]^-$  locates at about -1.45 V. This reduction potential separation could be mainly assigned as the difference in formation

constant of  $[Au(CN)_4]^-$  complex at  $\sim 10^{56}$ , and  $[Ag(CN)_2]^-$  complex at  $5.6 \times 10^{18}$  respectively. Also, the aforementioned similarity in reduction potential between  $[Au(CN)_2]^-$  and  $[Ag(CN)_2]^-$  complexes, can now maybe explained by their much more closed formation constants of  $2 \times 10^{38}$  and  $5.6 \times 10^{18}$ .<sup>32</sup> The considerable reduction potential separation between  $[Au(CN)_4]^-$  and  $[Ag(CN)_2]^-$ , would allow Au/Ag alloy to be deposited on the surface of stainless steel substrate in the bipolar system, with an increasing percentage ratio of Au towards end along the BPE cathode.

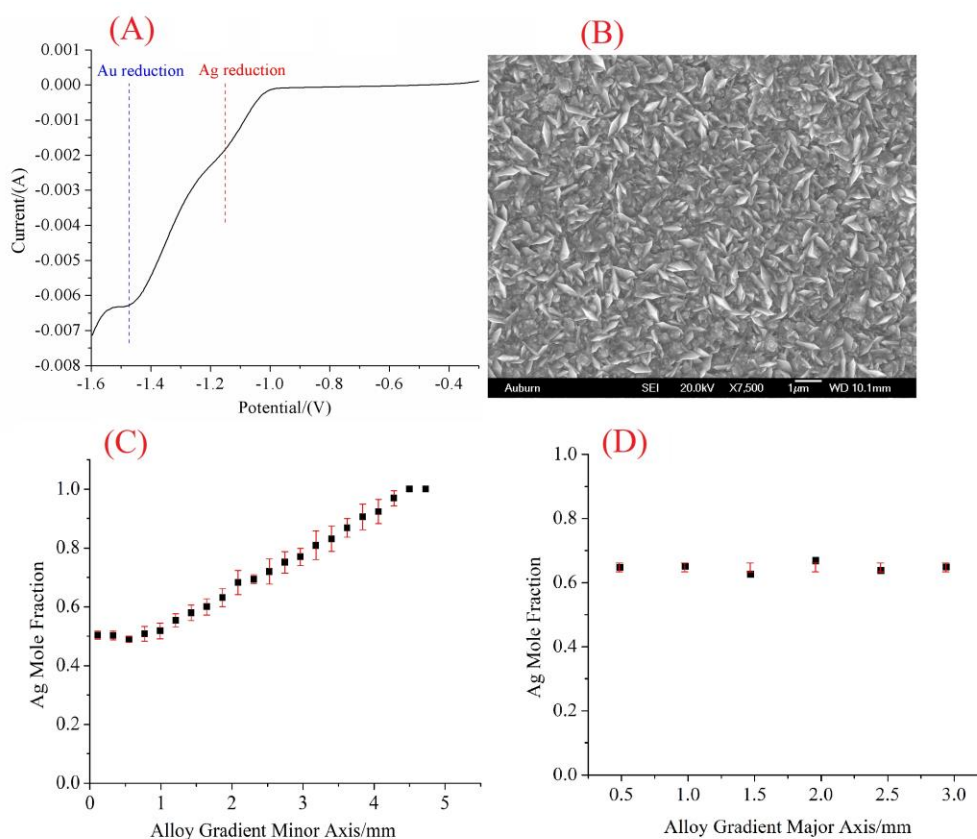


**Figure 2.5** Cyclic voltammogram of co-deposition solution (A), scan rate 50 mV/s. SEM image of the Ag/Au alloy (B), bar size: 1  $\mu$ m. The alloy gradient composition obtained from EDX measurements along the major and minor axes of the BPE cathode (C, D). Error bars indicate the standard deviation of three independent measurements.

Electrodeposition was carried out on the stainless steel BPE substrate in the bipolar cell frame (A) from Figure 2.2 using this co-deposition solution under 6.5V for 3min. One side of the substrate served as the BPE cathode for deposition and the other side on the bottom served as the BPE anode for corresponding oxidation reaction. Due to half of the cathode was covered by parafilm, Ag/Au bimetallic alloy would only be deposited on the other half cathodic side of the stainless-steel substrate. As discussed, the cyanide solution was titrated to a basic condition with pH value equals to 12. Two benefits could be obtained from this pH adjustment. On one hand, cyanide solution, as the common deposition solution environment which provides a stabilized metal-cyanide complex for uniform film coverage, in the bipolar electrodeposition, the oxidation of water on the driving anode would produce  $H^+$  locally and possibly form HCN with  $CN^-$ , by setting the solution pH to a much more basic condition, the formation of toxic HCN could be avoided. On the other hand, even though at pH =12, hydrogen evolution is still present during the process of Ag and Au deposition as shown in a step-down trend in the CV curve, the extent of bubble generation would be minimized and provide a relative uniform morphology and continuous bimetallic alloy ratio across the BPE substrate cathode as demonstrated in the following SEM and EDX characterization.

After the pre-electrodeposition, the deposited part as cathode was cut off from the stainless-steel substrate for characterization. In future discussion, this cathode strip was turned 90 degree and would serve as another whole BPE body for subsequent BRSE study. Here we defined the major axis as the length along the new BPE, which would be parallel to the electric field in the new bipolar cell. The minor axis across the width, which is along the Ag/Au bimetallic alloy gradient, would be vertical to the electric field. Figure 2.5(B) shows the SEM image of the half cathode strip which is not covered by parafilm during electrodeposition. Ag/Au alloy is



successfully deposited on the surface of stainless steel with consistent poly-crystalline structure and fully covered the substrate. These polycrystals are “needle-like” shapes with about 1  $\mu\text{m}$  in length and 0.3  $\mu\text{m}$  in width with uniform distribution. The alloy composition gradient is characterized synchronously by using Ag mole ratio acquired from EDX measurement, across two directions of the deposited BPE. In the plot illustrated in Figure 2.5(C), Ag mole ratio of the alloy changes gradually from around 50% to 100% crossing 4 mm length along the minor axis. The standard deviation, less than 2.5% in each point as shown in the error bar, is calculated from measurement of three sampling points at the same distance in minor axis but different position in major axis. While in Figure 2.5(D), it exhibits an identical Ag mole ratio along the major axis, with standard deviation less than 1.4% in each point. The consistent change of Ag/Au alloy gradient along the major axis and its uniformity along the horizontal distance strongly suggested that the half cathode strip could be employed as the new BPE substrate for NTP monolayer immobilization on varying bimetallic alloy composition.

### 2.3.2 Solution Potential Profile in Bipolar Cell System

The reduction of NTP molecules on electrode surface is very sensitive to the overpotential applied, especially for monolayer with small amount of coverage. For the purpose of addressing the kinetics of reduction of NTP monolayer under same overpotential on the substrate with varying bimetallic alloy composition in our BRSE system, the interfacial potential at each local point across the BPE minor axis, vertical to the electric field applied by driving electrodes, must be carefully controlled to ensure the same value. Since the bipolar electrode in the cell is an equal potential body with an equilibrium potential adjusted by the surrounding solution potential, the interfacial potential variations along the BPE minor axis, could be just represented by the solution potential at each point next to the BPE. Instead of the absolute value, the solution potential was

measured as the difference across the BPE length. Voltage of 6V, which was proven to be appropriate for later NTP reduction study in BRSE, was applied in the BPE cell B (Figure 2.2) in 0.1M NaClO<sub>4</sub> solution. Three measurements were made individually along the BPE major axis line at left edge, middle and right edge of the cell with locating two self-made Ag/AgCl reference electrodes at the BPE distance. As was shown in Figure 2.6(A), they have the magnitudes at ca. 1.2V with about 17mV standard deviation. The almost same values confirm the same overpotential along the BPE minor axis with bimetallic alloy composition gradient during the Raman scattering operation.

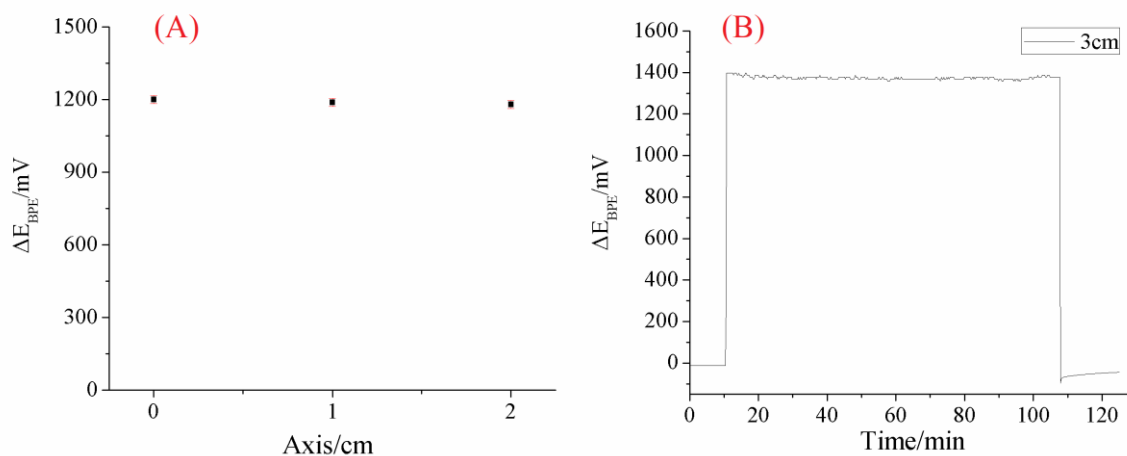


**Figure 2.6** (A) Solution potential difference  $\Delta E_{bpe}$  between the end of cathode and the end of anode of BPE length at the left edge, middle and right edge in the Raman Bipolar cell (6 V applied voltage on Au driving electrode, and the length of BPE is 26mm). (B) Potential difference  $\Delta E_{bpe}$  as a function of time in the middle major axis line (6 V applied voltage on Au driving electrode, and the length of BPE is 30mm).

In addition, the overpotential stability during following bipolar Raman characterization was examined by potential-time dependent measurement using the oscilloscope. Taking the major axis line in the middle as an example in Figure 2.6(B), the solution potential difference between the

anode and cathode is considerable stable for close two hours, about 1.4 V with an 20mV standard deviation, indicating its stability and applicability of collecting consecutive Raman spectrum during bipolar electrochemistry for cathodic NTP reduction.

### 2.3.3 Characterization of the Reduction of NTP Monolayer on Bimetallic Ag/Au Alloy Using BRSE

NTP molecule has a high affinity to metal surfaces and its electrochemical reduction mechanisms process differs depending on the materials of substrate and reaction conditions. As illustrated in Figure 2.7(A), on Au substrate, the NTP favors the direct reduction to 4-aminothiophenol (4-ATP), while using Ag substrate, the NTP reduction goes through an intermediate process of 4,4'-dimercaptoazobenzene (DMAB) to 4-ATP.<sup>33</sup> Since 514nm laser from Raman spectrometer has a strong photo driven effect of NTP reduced to DMAB<sup>34-35</sup>, 785nm laser was used to characterize the reduction process of NTP on bimetallic alloy (Ag/Au).

The NTP monolayer on substrate used for Raman characterization was prepared by dipping the new BPE, which was covered by Ag/Au alloy with gradient as mentioned, in NTP solution for 2 hours. Then the BPE was placed in the bipolar cell with its NTP side towards the driving anode. According to our potential profile measurement, all NTP molecules along the minor axis with same major coordinate on the bipolar substrate would have the same cathodic overpotential for electrochemical reduction. Due to Ag/Au alloy gradient is across the minor axis, NTP reduction could be studied as a function of alloy composition under same cathodic overpotential. Also, the consistent Ag mole ratio of alloy across the major axis endows the study of NTP reduction as a function of cathodic overpotential under same alloy composition. Consequently, the 2D profile of reduction process on NTP molecules with varying cathodic overpotential and alloy composition

based on Ag mole ratio could be recorded by using in situ Raman characterization under bipolar electrochemistry in equilibrium state.

Figure 2.7(B) illustrates the CVs of NTP monolayer on the surface of three different substrates in 0.1 M NaClO<sub>4</sub> solution. Au, Ag, and Ag/Au on the surface of stainless steel were electrodeposited by applying around (-1.5) V with Bulk Electrolysis (BE from AfterMath software on PINE Potentiostat) for 60 seconds to the stainless-steel sheets dipping in *HAuCl*<sub>4</sub> (30 mM), *AgNO*<sub>3</sub> (30 mM), and the *HAuCl*<sub>4</sub>:*AgNO*<sub>3</sub> (30 mM, 1:1) solutions containing 300 mM KCN supporting electrolyte with pH=12, respectively. Then followed by immersing in NTP solution for 2 hours. As the CVs (Figure 2.7(B)) demonstrate that the reduction of NTP occurs at less negative potential at the gold substrate surface in compared with silver and Ag/Au alloy showed that the gold substrate has better catalytic ability for the reduction of NTP molecules.

As mentioned, immobilized NTP monolayer on Ag/Au alloy surface would undergo two main reduction processes under enough negative potential, and the time it takes for its reduction to the equilibrium state depends on the reduction potential, laser power and wavelength. In our case, the latter two parameters are fixed during the whole experiment and waited for 12min after applied the potential to begin the Raman spectra measurement. That is in accordance with others reports that the Raman peaks would reach a steady state after a period of time.<sup>10, 22</sup> This equilibrium state reached after a certain time could thus lay the foundation for our system with lasting multiple Raman spectra acquisitions spatially under bipolar electrochemistry with stable cathodic overpotential distribution. The Raman spectrum of NTP at equilibrium states on Ag/Au alloy substrate is shown in Figure 2.7(C). The vibrational bands at 1080, 1335, and 1572 cm<sup>-1</sup>, are corresponding to C-S stretching, O-N-O stretching, and the phenyl ring modes, respectively. Raman bands at 1140, 1390, and 1434 cm<sup>-1</sup>, which mainly from the DMAB, correspond to C-N

symmetric stretching,  $N=N$  stretching, and  $C-H$  in plane bending modes, respectively. In addition, during the process of NTP molecules reduction to ATP, the  $1572\text{ cm}^{-1}$  band would decrease and finally disappear, and a new band at  $1594\text{ cm}^{-1}$  would generate.

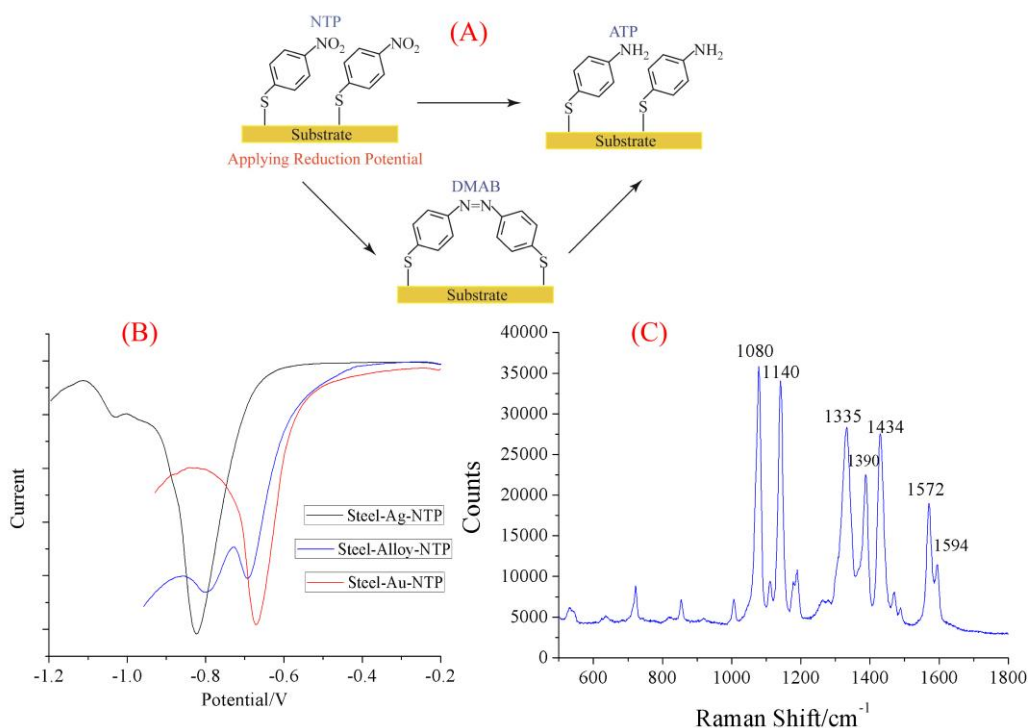


**Figure 2.7** (A) Schematic NTP reduction mechanisms of (1) direct reduction to 4-aminothiophenol (ATP) and (2) through an intermediate 4,4'-dimercaptoazobenzene (DMAB) to ATP. (B) CVs of NTP monolayer on three different substrates: Au, Ag and Ag/Au alloy on stainless-steel, respectively, in 0.1M NaClO<sub>4</sub> solution bubbled with nitrogen, scan rate: 5 mV/s. (C) Raman spectrum of NTP at equilibrium states on Ag/Au alloy.

In our BRSE study, the peak at  $1335\text{ cm}^{-1}$  from  $O-N-O$  stretching of NTP and peak at  $1434\text{ cm}^{-1}$  peak is one from  $C-H$  in plane bending of DMAB are selected to address NTP reduction and the formation of intermediate. In virtue of the same existence of  $C-S$  stretching in NTP and its reduction product, this peak at  $1080\text{ cm}^{-1}$  could be used as reference peak for Raman intensity

normalization.  $I_{1335}/I_{1080}$  and  $I_{1434}/I_{1080}$ , (short for the peak height intensity at 1335 and 1434  $\text{cm}^{-1}$  divided by the reference peak height intensity at 1080  $\text{cm}^{-1}$ , respectively), as characterizing the NTP reduction rate parameters. Also, because of the gradual disappearance of peak at 1572  $\text{cm}^{-1}$  and appearance of new peak at 1594  $\text{cm}^{-1}$ ,  $R = (I_{1594} - I_{1572}) / (I_{1594} + I_{1572})$  is served as a third parameter to characterize the NTP reduction. This third parameter would be more accurate compared to  $I_{1594}/I_{1080}$  since It could show the whole shifting peak changing from band 1572  $\text{cm}^{-1}$  to 1594  $\text{cm}^{-1}$ , which represents the process of NTP reducing to ATP, and increase the normalized intensity for the low intensity value of  $I_{1594}$  compared to that of  $I_{1080}$  as well.

The BRSE study was operated under 6V of applied voltage, with half of the BPE covered by NTP with Ag/Au alloy gradient underneath. Sequential Raman signals were collected along the major and minor axis with varying alloy composition and cathodic overpotential in a zig-zag pattern after reaching equilibrium state. Three normalized Raman peaks profiles,  $I_{1335}/I_{1080}$ ,  $R$ , and  $I_{1434}/I_{1080}$  are plotted as a function of calibrated cathodic overpotential and Ag mole ratio in a 2D profiles in Figure 2.8(B), (C), (D), separately.

In order to find out the differences of catalytic ability of alloy composite for the NTP reduction, the reduction potential of NTP showed on Raman peaks 2D profiles combine to that showed with cyclic voltammogram would be a better way, in other words, the potential showed on Raman 2D profile is relative potential versus Ag/AgCl reference electrode. Since the reduction of NTP monolayer on substrate surface is irreversible (showed on Figure 2.9 (C) and (D)), and the exact actual reduction potential on specific position of BPE is hard to know, the way to achieve the calculated reduction potential showed in the 2D profiles as follows (showed on Figure 2.9): Firstly, choose the  $E_{p/2}$  of cyclic voltammogram of NTP reduction on steel-Au substrate equals the reduction potential on the position in which  $R=0$  of Raman 2D profile on the same substrate, since

the solution potential gradient can get from Figure 2.10, we can calculate every reduction potential of the spot on the BPE, therefore, the calculated reduction potential can achieve for the Raman 2D profile; Secondly, use the calculated reduction potential profile from first part to check the NTP reaction on steel-Ag substrate to double check whether this method is reasonable, turned out the reduction potential on the position in which  $R=0$  of Raman 2D profile on steel-Ag substrate is almost same with the  $E_{p/2}$  of cyclic voltammogram of NTP reduction on same substrate. Therefore, this way to calculate the reduction potential on the Raman 2D profile is reasonable.

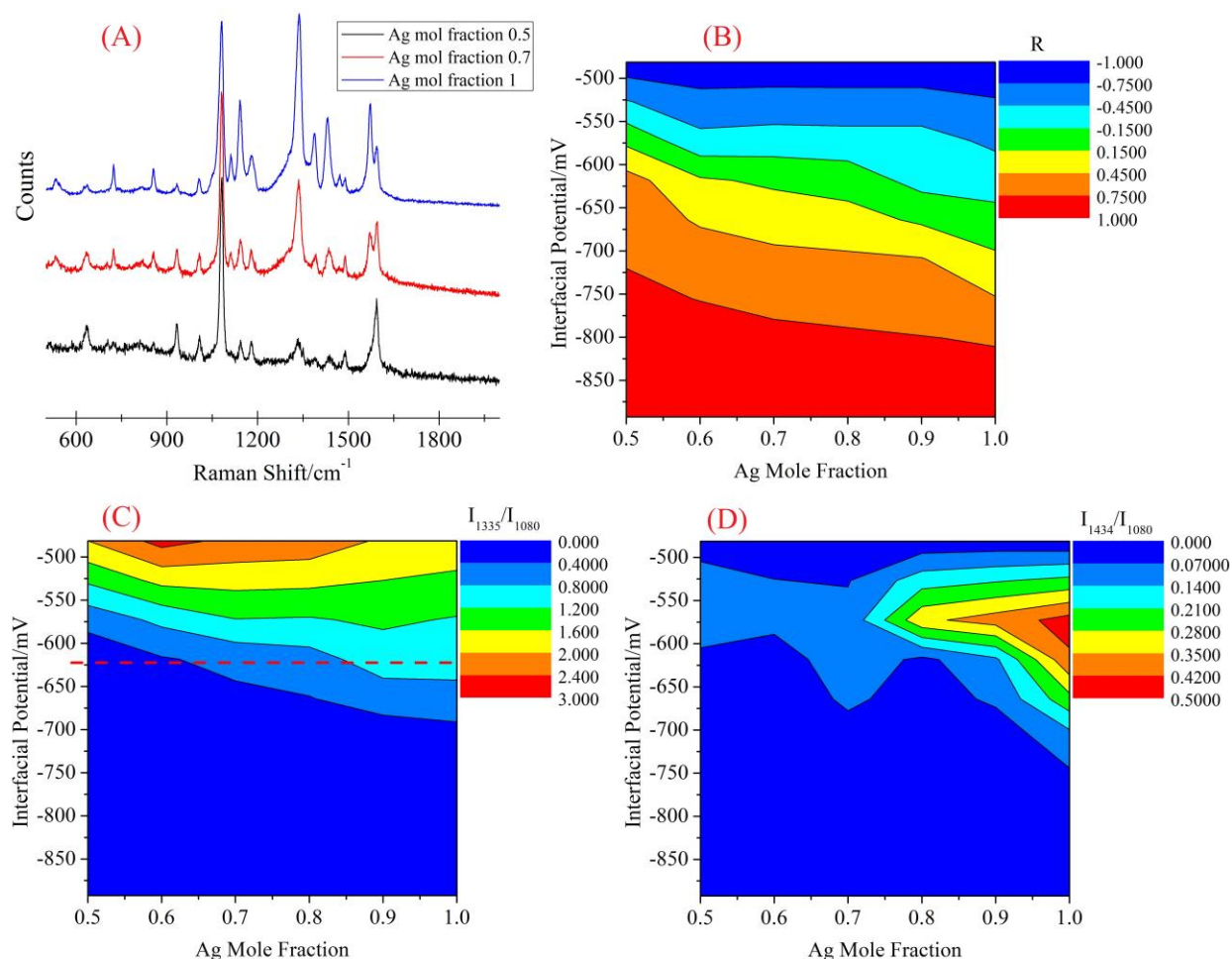


**Figure 2.8** Raman spectra (A) acquired at -625 mV at the indicated alloy compositions. Normalized Raman peak intensity profiles for R (B),  $I_{1335}/I_{1080}$  (C), and  $I_{1434}/I_{1080}$  (D).

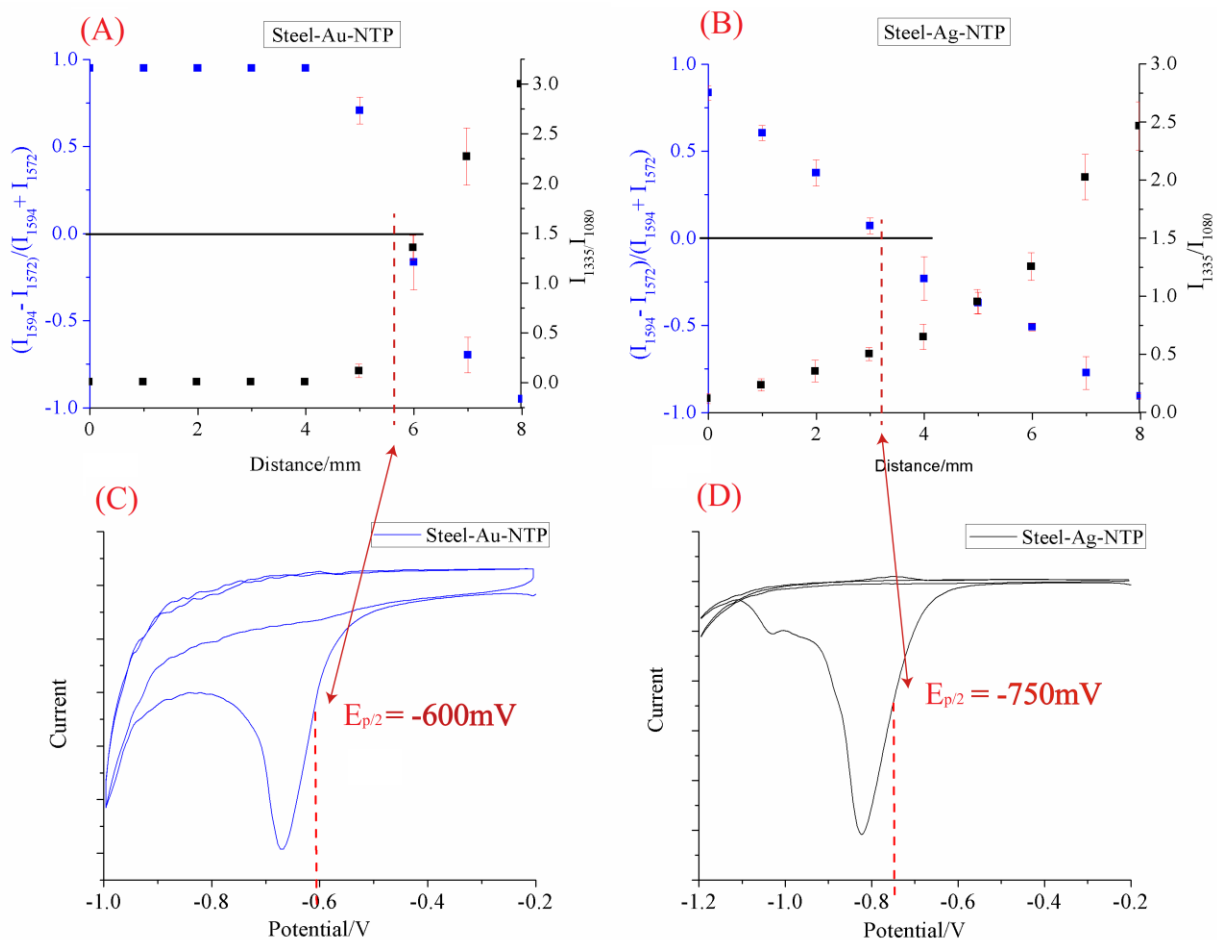


**Figure 2.8** (A) and (B) are normalized Raman peak intensities of  $I_{1335}/I_{1080}$ ,  $(I_{1594}-I_{1572})/(I_{1594}+I_{1572})$  as a function of distance from the BPE cathodic edge measured on Au and Ag substrate under 6V applied voltage on the driving electrodes, respectively; (C) and (D) are voltammograms of NTP reduction on different substrates as Ag/AgCl reference electrode in 0.1 M  $\text{NaClO}_4$  solution under nitrogen atmosphere with a scan rate of 5 mV/s, Pt grid as counter electrode.

Representative SERS spectra of 4-NTP self-assembled monolayers on an Ag/Au alloy gradient under steady state conditions at -625 mV are shown in Figure 2.8(A) for the three specific alloy compositions noted in the legend. When the Ag mole fraction is 1.0, the monolayer is mostly oxidized, with a significant surface concentration of 4-NTP (blue curve). Raman bands at 1140, 1390, and  $1434\text{ cm}^{-1}$  arise from the C-N symmetric stretch, N=N stretch, and the C-H in-plane



bending modes, respectively, of 4, 4' dimercaptoazobenzene (DMAB, partially reduced dimer species). In addition, due to the ca.  $22\text{ cm}^{-1}$  shift in the ring modes between 4-NTP and 4-ATP, their interconversion can easily be monitored spectroscopically. The  $1572\text{ cm}^{-1}$  band from 4-NTP decreases in intensity as 4-NTP is reduced and the band at  $1594\text{ cm}^{-1}$  (corresponding 4-ATP) increases in intensity (Figure 2.8A). These data illustrate how SERS can be used to monitor the interconversion of 4-NTP, DMAB, and 4-ATP as a function of potential and alloy composition using bipolar electrochemistry. As noted above, the ring modes of 4-ATP and 4-NTP are easy to resolve ( $1572\text{ cm}^{-1}$  and  $1594\text{ cm}^{-1}$ , respectively), the progress of their interconversion could be monitored by simultaneously measuring changes in these two bands in SERS spectra (see Figure 2.8B). More specifically, the ratio R is a convenient metric that reports on both 4-NTP and 4-ATP surface concentrations. That is, under conditions where the monolayer is comprised of fully oxidized 4-NTP,  $I_{1594}=0$ , and  $R=-1$ . On the other hand, under conditions where the monolayer is fully reduced,  $I_{1572}=0$  and  $R=+1$ . When the surface concentrations of the two forms are equal, the sign of R changes. In all cases, data from at least three separate experiments were averaged.

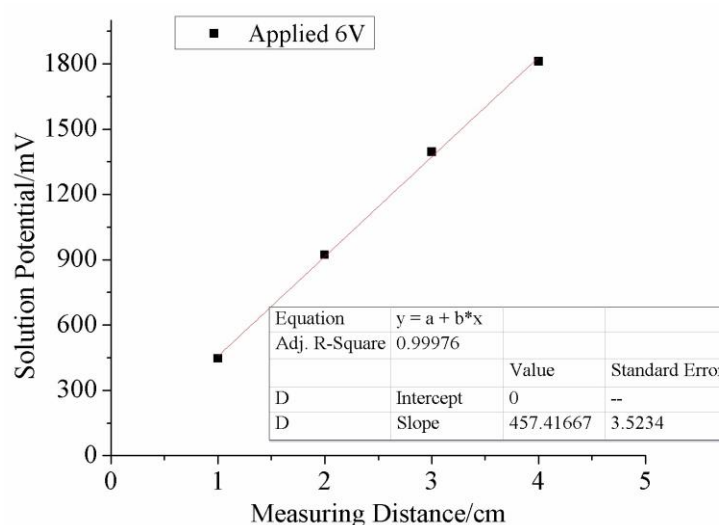


**Figure 2.9** Solution potential as a function of measuring distance in 0.1M  $\text{NaClO}_4$  using the Raman cell frame under 6V applied voltage.

Figure 2.8C shows how the ratio  $I_{1335}/I_{1080}$  (which reports on the surface concentration of 4-NTP) depends on the electrode potential and alloy composition as measured along the two dimensions of the BPE. The red dashed line indicates the potential at which the SERS spectra discussed above were acquired. At potentials more positive than about -575 mV, the monolayer is fully oxidized independent of alloy composition.  $I_{1335}$  is at or near its maximum value (green, yellow, and red regions of the plot). For potentials more negative than about -700 mV, the monolayer is fully reduced, also independent of alloy composition.  $I_{1335}$  is close to 0 and unchanging (blue region of the plot). Finally, for potentials near -625 mV, the surface concentration of 4-NTP is strongly dependent on alloy composition. When the alloy Ag mole fraction is 0.5, the monolayer is fully reduced (blue). On pure Ag, the monolayer is not fully reduced until much more negative potentials near -700 mV are reached. The key takeaway is that the surface concentration of 4-NTP depends on the alloy composition in addition to the interfacial potential.

Figure 2.8B shows how the experimentally measured value of  $R$  (defined above) varies as a function of potential and composition. As expected, under conditions where the monolayer is comprised of fully oxidized 4-NTP,  $I_{1594}=0$ , and  $R$  has a value of -1 (blue in the plot). On the other hand, under conditions where the monolayer is fully reduced,  $I_{1572}=0$  and  $R=+1$  (red in the plot). The potential where  $R$  changes sign corresponds to the condition where the surface concentrations of 4-NTP and 4-ATP are equal – that is, the  $E_{1/2}$  value (green-yellow border).  $E_{1/2}$  is dependent on the composition of the alloy, changing by about 100 mV over the range of compositions investigated. This trend is similar to that described previously for 4-NTP. The shifts in  $E_{1/2}$  observed spectroscopically are consistent with our cyclic voltammetry measurements and those published in the literature.<sup>36-37</sup>

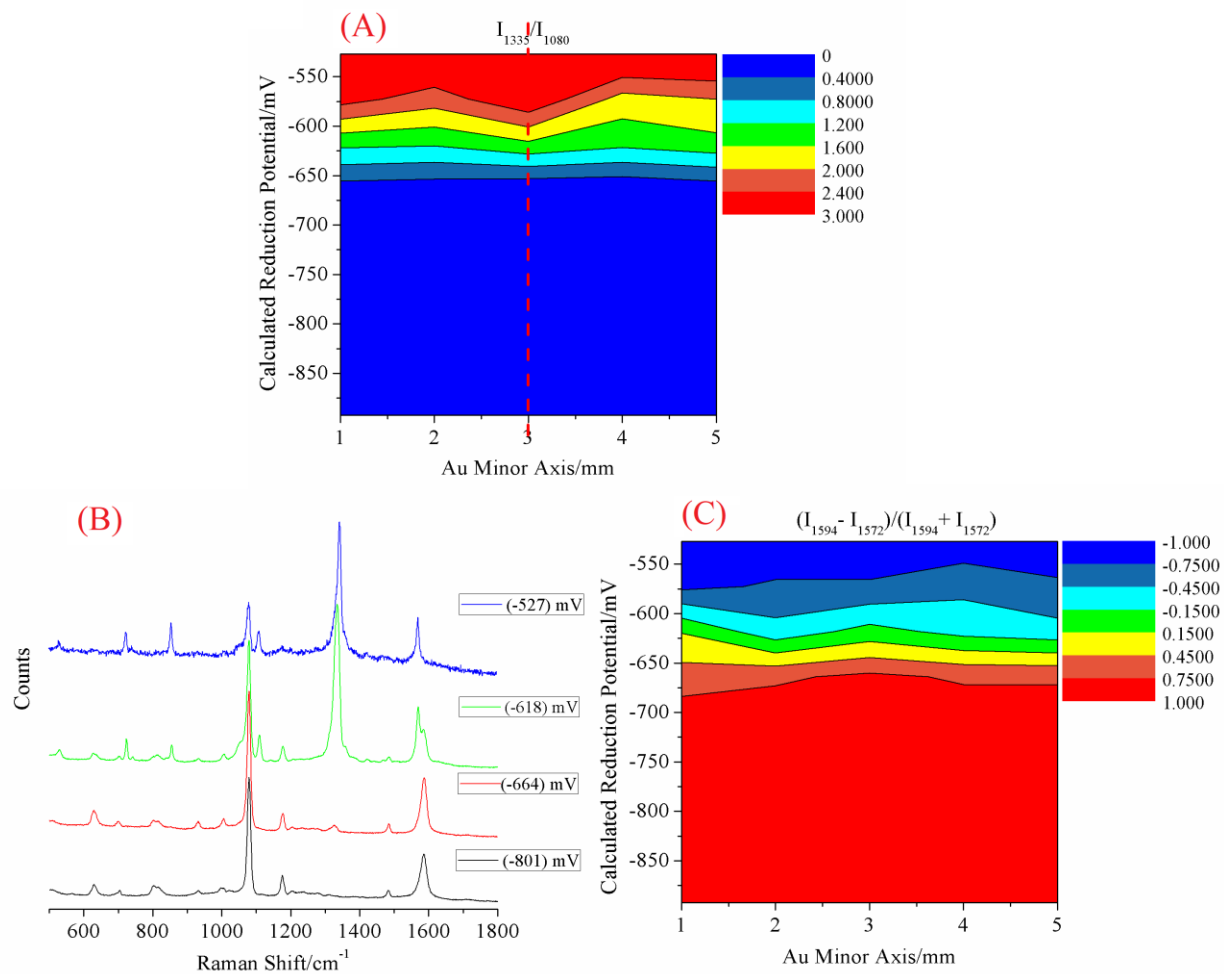


**Figure 2.10** Normalized Raman peak intensity profiles on pure Au:  $I_{1335}/I_{1080}$  (A); R (C). Raman spectra (B) acquired along the red-dashed line in (A).

To rule out the possibility that optical misalignment between the bipolar cell and the axes of the Raman spectrometer could account for the behavior described above, we conducted analogous measurements for 4-NTP monolayers adsorbed on pure Au BPEs, Figure 2.11. In this control, there is no composition gradient along the minor axis of the BPE (90° to the potential gradient) as the electrode is pure Au. Both plots of  $I_{1335}/I_{1080}$  (Figure 2.11A), R (Figure 2.11C) as well as the raw SERS spectra (Figure 2.11B) show a uniform distribution of 4-NTP/4-ATP along the minor axis of the BPE with the expected changes as a function of potential. SERS data collected along

the vertical red dashed line show a smooth progression from 4-NTP to 4-ATP along the principle axis of the BPE (electric field direction), as expected.

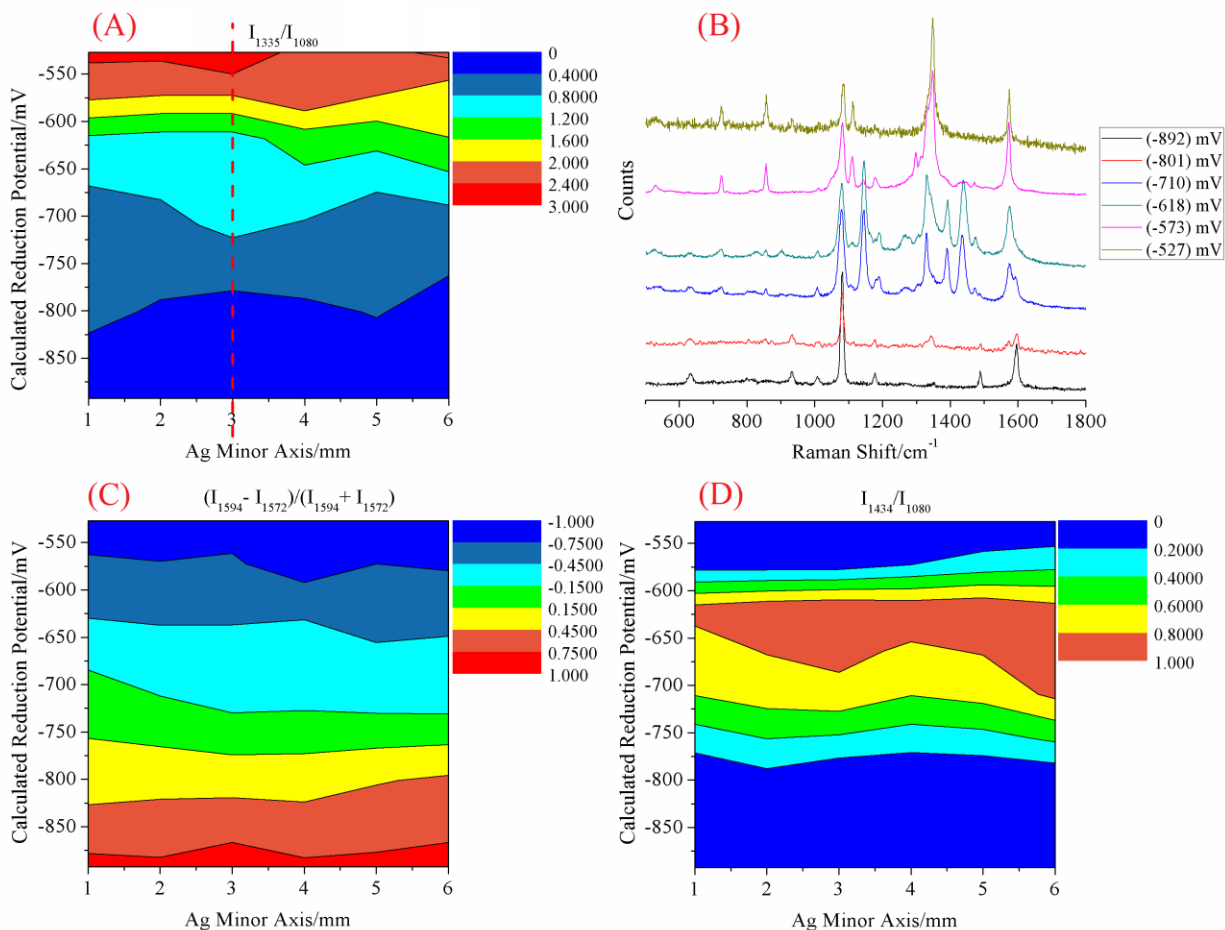


**Figure 2.11** Normalized Raman peak intensity profiles on pure Ag:  $I_{1335}/I_{1080}$  (A);  $(I_{1594} - I_{1572})/(I_{1594} + I_{1572})$  (C); and  $I_{1434}/I_{1080}$  (D). Raman spectra (B) acquired along the red-dashed line in (A).

Previous researchers have discussed the fact that, in addition to the direct electrochemical reduction of 4-NTP to 4-ATP, it is also possible under certain conditions of potential, pH, and laser irradiation, to form a partially reduced azo-dimer (DMAB).<sup>33</sup> We wished to investigate whether this process might be responsible for the dependence of the apparent  $E_{1/2}$  on alloy composition. Therefore, we used SERS to determine the experimental conditions under which DMAB could be

observed on the alloy surface. As noted earlier, the C-H in-plane bend at  $1434\text{ cm}^{-1}$ , normalized to the C-S stretch is a convenient measure of the surface concentration of DMAB. A plot of  $I_{1434}/I_{1080}$  as a function of potential and alloy composition is shown in Figure 2.11D. The surface concentration of DMAB is very dependent on potential and alloy composition. This observation strongly suggests that the conversion of 4-NTP to 4-ATP occurs by a different pathway at higher Ag mole fractions. For alloy compositions below about 0.70 Ag, little to no DMAB is observed under steady state conditions. On pure Ag surfaces, however, there is a ca. 20 mV window where significant surface concentrations of DMAB are detected by SERS. Similar results also could be achieved when using pure Ag substrate, illustrated in Figure 2.12.

To summarize the bipolar Raman spectroelectrochemistry findings, the mechanism by which 4-NTP is converted to 4-ATP depends on the alloy composition. For alloy compositions above about 70% Ag, 4-NTP is first partially reduced to DMAB, which is then further reduced to 4-ATP at more negative potentials. As the Ag content of the alloy decreases with increasing Au mole fraction, the amount of DMAB present on the surface appears to decrease. Below roughly 70% Ag, 4-NTP is directly converted to 4-ATP, and no DMAB is observed spectroscopically at any potential.

Campion was one of the first researchers to document the importance of adsorbate-substrate charge transfer transitions in SERS.<sup>38</sup> Beyond accounting for part of the SERS enhancement factor, other researchers have noted that depending on the initial and final states coupled by these CT transitions, it is possible to induce photoredox reactions during a SERS measurement. Indeed, even as early as 1992, Matsuda and coworkers suggested that charge transfer transitions between the Ag electrode and adsorbed 4-NTP played a role in their SERS pioneering measurements.<sup>39</sup>

We believe our results are consistent with the previously published computational investigation by Tian, et al.<sup>10</sup> Crucially, these workers demonstrated that metal-to-molecule CT transitions in the visible region of the electromagnetic spectrum could drive the photo-electrochemical reduction of 4-NTP SAMs on Au and Ag surfaces. Conversely, molecule-to-metal CT processes were shown to be operative in photo-electrochemical oxidation of 4-ATP. According to these researchers, photoreduction involves coupling metal electrons near the Fermi level to anti-bonding states in the 4-NTP. The calculated metal-to-4-NTP CT transition energies for Ag and Au were 1.76 and 2.35 eV, respectively. While the Au CT process is not accessible, the 1.76 eV value for Ag is reasonably close to the laser frequency used for our SERS measurements (785 nm, or 1.6 eV). The 4-ATP-to-metal CT transitions that could be important in the photo-oxidation of 4-ATP were found to be 2.2 and 2.48 eV on Ag and Au, respectively. Thus, using 785 nm (1.6 eV) excitation, as in the experiments described herein, we believe it is possible to excite two relevant Ag-to-molecule CT transitions leading to the photo-assisted reduction of 4-NTP to 4-nitrosothiophenol and 4-hydroxylaminothiophenol. These two molecules can couple to form DMAB, in analogy to the Haber process. On Au rich alloys, on the other hand, these photoinduced redox channels are much higher in energy (>2 eV) and thus are not accessible using 785 nm radiation, so that only direct electrochemical transformations are possible.

It only remains to account for the increase in the amount of DMAB formed as the mole fraction of Ag in the alloy increases. We believe this can be explained on the basis that the plasmonic efficiency of Ag is higher than that of Au and that the absorption cross-section for the alloy increases as the Ag content of the film increases. We have previously reported on this effect, for films are similar to those studied here.<sup>31</sup> This is additional confirming evidence that the formation of DMAB is a photo-assisted process.

## 2.4 Conclusions

In this work, we present a novel method, bipolar Raman spectro-electrochemistry (BRSE), to investigate the reduction process of NTP monolayer on Ag/Au alloy substrate. With the help of bimetallic alloy gradient established by pre-bipolar electrodeposition, a monolayer of studied molecule, such as NTP, was immobilized on the cathode of BPE substrate. Then Raman characterization profile on 2D system as a function of potential and bimetallic alloy composition could be achieved simultaneously in longitude and latitude across the BPE. The reaction process can thus be addressed under continuous potential control and varying bimetallic alloy composition bi-directionally using BRSE. The results shown as the Ag mole ratio of alloy increases (from 50% to 100% range), the alloy substrate would become less favorable for the reduction of NTP to ATP.

In this method, the bipolar electrochemistry provides a uniform and continuous potential control and the Raman characterization provides a in situ record of quantitative information about catalyst activity. Not only Ag/Au alloy for NTP reduction, large libraries of potential catalyst candidates, like Au/Ag/Pt/Pd/Cd, etc., with varying alloy composition and other parameters, can be rapidly evaluated and screened out for efficient electrocatalysis.

## References

1. Zhai, Y.; Zhu, Z.; Zhou, S.; Zhu, C.; Dong, S., Recent Advances in Spectroelectrochemistry. *Nanoscale* **2018**, *10*, 3089-3111.
2. Choi, H.-K.; Park, W.-H.; Park, C.-G.; Shin, H.-H.; Lee, K. S.; Kim, Z. H., Metal-Catalyzed Chemical Reaction of Single Molecules Directly Probed by Vibrational Spectroscopy. *J. Am. Chem. Soc.* **2016**, *138* (13), 4673-4684.
3. Li, J.; Liu, J.; Yang, Y.; Qin, D., Bifunctional Ag@ Pd-Ag nanocubes for highly sensitive monitoring of catalytic reactions by surface-enhanced Raman spectroscopy. *J. Am. Chem. Soc.* **2015**, *137* (22), 7039-7042.
4. Matsuda, N.; Sawaguchi, T.; Osawa, M.; Uchida, I., Surface-assisted photoinduced reduction of p-nitrothiophenol self-assembled monolayer adsorbed on a smooth silver electrode. *Chem. Lett.* **1995**, *24* (2), 145-146.
5. Lu, T.; Cotton, T. M.; Birke, R. L.; Lombardi, J. R., Raman and surface-enhanced Raman spectroscopy of the three redox forms of 4, 4'-bipyridine. *Langmuir* **1989**, *5* (2), 406-414.
6. Ying, Y.-L.; Hu, Y.-X.; Gao, R.; Yu, R.-J.; Gu, Z.; Lee, L. P.; Long, Y.-T., Asymmetric Nanopore Electrode-Based Amplification for Electron Transfer Imaging in Live Cells. *J. Am. Chem. Soc.* **2018**, *140* (16), 5385-5392.
7. Xu, F.; Wang, H.; He, X.-D.; Deng, N.; Li, F.; Li, B.; Xie, J.-H.; Han, S.-K.; He, J.-B., One-step deposition of Ni x Cu 1- x alloys with both composition gradient and morphology evolution by bipolar electrochemistry. *J. Electroanal. Chem.* **2018**.
8. Koefoed, L.; Pedersen, E. B.; Thyssen, L.; Vinther, J.; Kristiansen, T.; Pedersen, S. U.; Daasbjerg, K., Functionalizing Arrays of Transferred Monolayer Graphene on Insulating Surfaces by Bipolar Electrochemistry. *Langmuir* **2016**, *32* (25), 6289-6296.



9. Zhang, L.; Gupta, B.; Goudeau, B.; Mano, N.; Kuhn, A., Wireless electromechanical readout of chemical information. *Journal of the American Chemical Society* **2018**, *140* (45), 15501-15506.
10. Ren, X.; Tan, E.; Lang, X.; You, T.; Jiang, L.; Zhang, H.; Yin, P.; Guo, L., Observing reduction of 4-nitrobenzenthionol on gold nanoparticles in situ using surface-enhanced Raman spectroscopy. *Physical Chemistry Chemical Physics* **2013**, *15* (34), 14196-14201.
11. Fosdick, S. E.; Knust, K. N.; Scida, K.; Crooks, R. M., Bipolar electrochemistry. *Angewandte Chemie International Edition* **2013**, *52* (40), 10438-10456.
12. Ibañez, D.; Heras, A.; Colina, A., Bipolar Spectroelectrochemistry. *Anal. Chem.* **2017**, *89* (7), 3879-3883.
13. Andolina, C. M.; Dewar, A. C.; Smith, A. M.; Marbella, L. E.; Hartmann, M. J.; Millstone, J. E., Photoluminescent gold–copper nanoparticle alloys with composition-tunable near-infrared emission. *J. Am. Chem. Soc.* **2013**, *135* (14), 5266-5269.
14. Dai, L.; Song, L.; Huang, Y.; Zhang, L.; Lu, X.; Zhang, J.; Chen, T., Bimetallic Au/Ag Core–Shell Superstructures with Tunable Surface Plasmon Resonance in the Near-Infrared Region and High Performance Surface-Enhanced Raman Scattering. *Langmuir* **2017**, *33* (22), 5378-5384.
15. Tsao, Y.-C.; Rej, S.; Chiu, C.-Y.; Huang, M. H., Aqueous phase synthesis of Au–Ag core–shell nanocrystals with tunable shapes and their optical and catalytic properties. *J. Am. Chem. Soc.* **2013**, *136* (1), 396-404.
16. Khlebtsov, B.; Panfilova, E.; Khanadeev, V.; Bibikova, O.; Terentyuk, G.; Ivanov, A.; Rummyantseva, V.; Shilov, I.; Ryabova, A.; Loshchenov, V., Nanocomposites containing silica-coated gold–silver nanocages and Yb–2, 4-Dimethoxyhematoporphyrin: Multifunctional

capability of IR-luminescence detection, photosensitization, and photothermolysis. *ACS nano* **2011**, *5* (9), 7077-7089.

17. Juzgado, A.; Soldà, A.; Ostric, A.; Criado, A.; Valenti, G.; Rapino, S.; Conti, G.; Fracasso, G.; Paolucci, F.; Prato, M., Highly sensitive electrochemiluminescence detection of a prostate cancer biomarker. *J. Mater. Chem.B* **2017**, *5* (32), 6681-6687.

18. Yuan, T.; Le Thi Ngoc, L.; van Nieuwkastele, J.; Odijk, M.; van den Berg, A.; Permentier, H.; Bischoff, R.; Carlen, E. T., In situ surface-enhanced raman spectroelectrochemical analysis system with a hemin modified nanostructured gold surface. *Anal. Chem.* **2015**, *87* (5), 2588-2592.

19. Kiyonaga, T.; Jin, Q.; Kobayashi, H.; Tada, H., Size-Dependence of Catalytic Activity of Gold Nanoparticles Loaded on Titanium (IV) Dioxide for Hydrogen Peroxide Decomposition. *ChemPhysChem* **2009**, *10* (17), 2935-2938.

20. Boghosian, S.; Bebelis, S.; Vayenas, C.; Papatheodorou, G., In situ high temperature SERS study of Ag catalysts and electrodes during ethylene epoxidation. *J. Catal.* **1989**, *117* (2), 561-565.

21. Hartman, T.; Wondergem, C. S.; Kumar, N.; van den Berg, A.; Weckhuysen, B. M., Surface-and tip-enhanced Raman spectroscopy in catalysis. *J. Phys. Chem. Lett.* **2016**, *7* (8), 1570-1584.

22. Li, P.; Ma, B.; Yang, L.; Liu, J., Hybrid single nanoreactor for in situ SERS monitoring of plasmon-driven and small Au nanoparticles catalyzed reactions. *Chem. Commun.* **2015**, *51* (57), 11394-11397.

23. Cui, Q.; Yashchenok, A.; Li, L.; Moehwald, H.; Bargheer, M., Mechanistic study on reduction reaction of nitro compounds catalyzed by gold nanoparticles using in situ SERS monitoring. *Colloids Surf., A* **2015**, *470*, 108-113.

24. Krajczewski, J.; Kołataj, K.; Pietrasik, S.; Kudelski, A., Silica-covered star-shaped Au-Ag nanoparticles as new electromagnetic nanoresonators for Raman characterisation of surfaces. *Spectrochim. Acta, Part A. Mol. Biomol. Spectrosc.* **2018**, *193*, 1-7.
25. Yin, Z.; Wang, Y.; Song, C.; Zheng, L.; Ma, N.; Liu, X.; Li, S.; Lin, L.; Li, M.; Xu, Y., Hybrid Au-Ag Nanostructures for Enhanced Plasmon-Driven Selective Hydrogenation through Visible Light Irradiation and Surface-Enhanced Raman Scattering. *J. Am. Chem. Soc.* **2018**, *140* (3), 864–867.
26. Han, Q.; Zhang, C.; Gao, W.; Han, Z.; Liu, T.; Li, C.; Wang, Z.; He, E.; Zheng, H., Ag-Au alloy nanoparticles: Synthesis and in situ monitoring SERS of plasmonic catalysis. *Sens. Actuators, B* **2016**, *231*, 609-614.
27. Cao, M.; Zhou, L.; Xu, X.; Cheng, S.; Yao, J.-L.; Fan, L.-J., Galvanic replacement approach for bifunctional polyacrylonitrile/Ag–M (M= Au or Pd) nanofibers as SERS-active substrates for monitoring catalytic reactions. *J. Mater. Chem. A* **2013**, *1* (31), 8942-8949.
28. Luo, L.; Duan, Z.; Li, H.; Kim, J.; Henkelman, G.; Crooks, R. M., Tunability of the adsorbate binding on bimetallic alloy nanoparticles for the optimization of catalytic hydrogenation. *J. Am. Chem. Soc.* **2017**, *139* (15), 5538-5546.
29. Tisserant, G.; Gillion, J.; Lannelongue, J.; Fattah, Z.; Garrigue, P.; Roche, J.; Zigah, D.; Kuhn, A.; Bouffier, L., Single-Step Screening of the Potential Dependence of Metal Layer Morphologies along Bipolar Electrodes. *ChemElectroChem* **2016**, *3* (3), 387-391.
30. Ramakrishnan, S.; Shannon, C., Display of solid-state materials using bipolar electrochemistry. *Langmuir* **2010**, *26* (7), 4602-4606.

31. Ramaswamy, R.; Shannon, C., Screening the Optical Properties of Ag– Au Alloy Gradients Formed by Bipolar Electrodeposition Using Surface Enhanced Raman Spectroscopy. *Langmuir* **2011**, *27* (3), 878-881.
32. Nicol, M.; Paul, R.; Fleming, C. In *The chemistry of the extraction of gold*, Mintek: 1987.
33. Corma, A.; Concepción, P.; Serna, P., A different reaction pathway for the reduction of aromatic nitro compounds on gold catalysts. *Angewandte Chemie International Edition* **2007**, *46* (38), 7266-7269.
34. Han, S. W.; Lee, I.; Kim, K., Patterning of organic monolayers on silver via surface-induced photoreaction. *Langmuir* **2002**, *18* (1), 182-187.
35. Shin, K. S.; Lee, H. S.; Joo, S. W.; Kim, K., Surface-induced photoreduction of 4-nitrobenzenethiol on Cu revealed by surface-enhanced Raman scattering Spectroscopy. *J. Phys. Chem. C* **2007**, *111* (42), 15223-15227.
36. Futamata, M., Surface-plasmon-polariton-enhanced Raman scattering from self-assembled monolayers of p-nitrothiophenol and p-aminothiophenol on silver. *The Journal of Physical Chemistry* **1995**, *99* (31), 11901-11908.
37. Nielsen, J. U.; Esplandiu, M. J.; Kolb, D. M., 4-Nitrothiophenol SAM on Au (111) investigated by in situ STM, electrochemistry, and XPS. *Langmuir* **2001**, *17* (11), 3454-3459.
38. Campion, A.; Ivanecy III, J.; Child, C.; Foster, M., On the mechanism of chemical enhancement in surface-enhanced Raman scattering. *Journal of the American Chemical Society* **1995**, *117* (47), 11807-11808.
39. Matsuda, N.; Yoshii, K.; Ataka, K.-i.; Osawa, M.; Matsue, T.; Uchida, I., Surface-enhanced infrared and Raman studies of electrochemical reduction of self-assembled monolayers formed from p-nitrothiophenol at silver. *Chemistry letters* **1992**, *21* (7), 1385-1388.

## Chapter 3

### Control of the Potential Profile of Bipolar Electrodes Using Cell Frames

#### 3.1 Introduction

Bipolar electrochemistry is an unconventional technique where a conductor is immersed electrochemically in an electrolyte wirelessly with two driving electrodes connected an external power supply, when the external power large enough to cause faradic reaction, the two distinct poles of bipolar electrode would exhibit opposite polarization with respect to the solution due to electric field crossing the whole cell, specifically, reduction occurs at the cathodic pole while oxidation happens simultaneously at the anodic.<sup>1</sup> Based on the different configurations, BPE system can be carried out into two system, 'open' BPE system, where BPE anode and BPE cathode sharing same cell, and 'closed' BPE system, where BPE anode and BPE cathode separated into different cell. And bipolar electrochemistry used in a variety of fields, such as electrodeposition,<sup>2</sup> electrocatalysis,<sup>3</sup> sensing,<sup>4</sup> concentration enrichments,<sup>5</sup> electro-grafting,<sup>6</sup> etc.

An important issue in BPE system is the applied voltage to the driving electrodes to achieve desired redox reaction occurs on the anode and cathode of BPE. Specifically, external bias of power source applied on the driving electrodes would induce an electric field formation in the solution, with an potential gradient across the cell from anodic driving electrode to the cathodic in the solution, when the interfacial potential between the solution and BPE is large enough would cause redox reaction happens.<sup>7</sup> However, one thing should be noted that there is a potential dropping at the driving electrode, and under some circumstances, the potential loss within the electrochemical double layers can be substantial.<sup>8</sup> And the dropped potential mainly occupied by double layer capacitance formation, charge transfer resistance and diffusion impedance happened at the metal electrode/solution surface.<sup>9</sup> The properties of interface formed by charged

electrode/electrolyte system governs the charge transfer processes through the interface itself, which would influence the electrochemical responses.<sup>10</sup> Thus some well-known models established based on Helmholtz's early theoretical work to address and refine the electrochemical double layers, such as Gouy–Chapman model and Gouy–Chapman–Stern model.<sup>11-12</sup> As for solution potential, which is applied voltage subtracts dropped potential, would be employed for inducing the electric field formation or potential gradient formation in the solution across the electrochemical cell. Noted that the exist of electric field or potential gradient in the solution indicates Faradic current flowing through the driving electrode, on the contrary, when the applied voltage is not big enough to cause faradic current happens on the driving electrodes, no potential gradient would be formed at steady states. And our purpose is offering a basic guideline for researchers to make the optimal BPE cell frames. To achieve that, it is important to understand the potential profile of different cell frames.

Herein, the potential profile of three types of cell frames were studied, as illustrated in Figure 3.1, three types of cell frame is open cell frame, closed cell frame and channel cell frame, respectively, and the electric field trend line (red line) that is virtual to show the probable trend of electron or anions moving direction in the solution. And the electric field strength that is a quantitative expression of the intensity of an electric field at a particular location can be tuned by the design of cell frame, as demonstrated in Figure 3.1, the electric field line in closed cell frame is uniform and have a same electric field strength anywhere in the cell under a fixed applied voltage, while the density of electric field line would slight decrease by using open cell frame and opposite results would obtain in channel cell frame. Therefore, the potential profile was studied based on these three types of cell frames, and simple models were proposed to describe the potential behavior of channel cell frames.

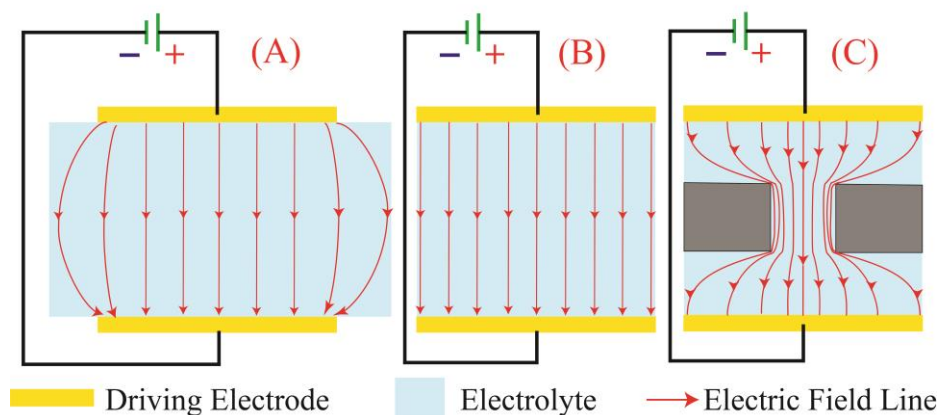


**Figure 3.12** Electric field strength illustrated in three cell frames, (A) open cell frame, (B) closed cell frame and (C) channel cell frame.

All the study has focused exclusively on what are known as ‘open’ BPE system cell frames in this section. As far as we understand the potential profile of ‘open’ BPE system cell frames, it would be much easier for us to comprehend the potential distribution of ‘closed’ BPE system cell frames that could simply be treated as two ‘open’ BPE system cell frames in series.

## 3.2 Experimental section

### 3.2.1 Materials and Reagents

All solutions were prepared with deionized, ultra-pure water (VWR Type II). Stainless Steel foil (0.5mm, Alfa Aesar), Gold foil (0.1mm thick, 99.99% trace metals, Sigma-Aldrich), Sodium perchlorate monohydrate ( $\geq 99.0\%$ , Fluka analytical), Potassium Chloride (crystals, BDH Chemicals), Ethyl Alcohol (200 Proof, ACS/USP grade, Pharmco-Aaper), Capillary tubes (I.D. 1.1-1.2 mm, Wall  $0.2 \pm 0.02$  mm, Kimble Chase), Silver wire (0.25mm diameter, 99.99%, Sigma-Aldrich), Tris(2,2'-bipyridyl) dichlororuthenium(II) hexahydrate ( $\text{Ru}(\text{bpy})_3\text{Cl}_2 \cdot 6\text{H}_2\text{O}$ ) (99.95%, Sigma-Aldrich), Sodium phosphate dibasic anhydrous (Sigma-Aldrich), Sodium Phosphate Monobasic (98.8%, Fisher Scientific), tri-*n*-propylamine (TPrA) ( $\geq 98\%$ , Sigma-Aldrich),

hydrogen peroxide (30% (v/v) in H<sub>2</sub>O, Sigma-Aldrich), sulfuric acid (HPLC grade) were from commercial sources and used as received, Potassium Ferricyanide(III) powder (99%, Sigma-Aldrich), Potassium nitrate (99.7%, Fisher Scientific).

ECL solution used 5mM Ru(bpy)<sub>3</sub><sup>2+</sup> as chemiluminescent, 25mM TPrA as co-reagent, prepared in 0.1M PBS buffer, pH=7. And 0.1M NaClO<sub>4</sub> Solution used for the potential measurement in the cell frames.

### 3.2.2 Apparatus

Panasonic Lumix DMC-LX3 Camera (Panasonic Corporation, Osaka Japan), Electrochemical Potentiostat (Pine Instrument), Power supply (9122A 0-60V/0-2.5A Single Output Programmable DC, B&K Precision Corporation), Solution potentials were monitored by a two-channel handheld oscilloscope (Hantek model DSO8060).

### 3.2.3 Preparation of Bipolar Electrochemical Cell Frames

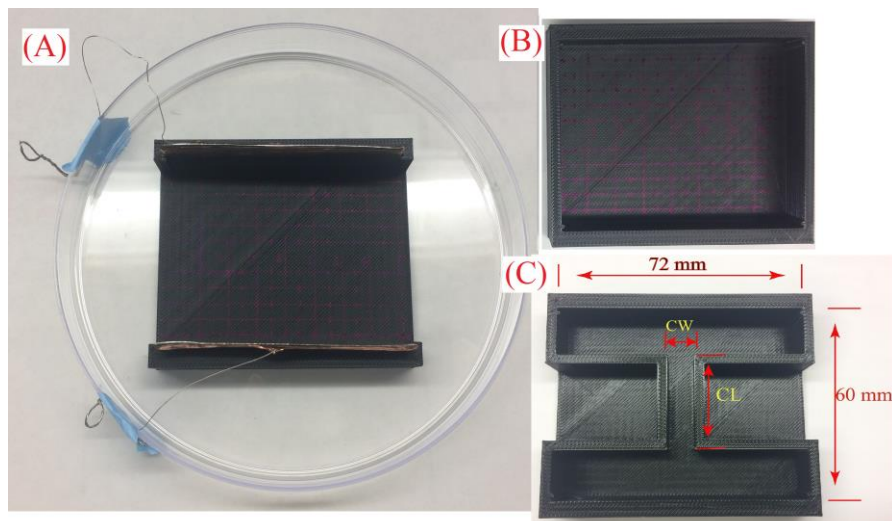


**Figure 3.13** (A), (B) and (C) are open cell frame, closed cell frame and channel cell frame, respectively.



Use 3D-printer (MakerBot Replicator 2) to print different bipolar electrochemical cell frames. Designs were modeled by Sketch Up © (Trimble Navigation Limited) and printed from polylactic acid filament (1.75mm diameter).

According to the structure of cell frames used for BPE system, cell frames divided into three categories: open cell frames, closed cell frames and channel cell frame. As shown in Figure 3.2, without notification, the cell frames, which used for the experimental research for the BPE system in this section, have a width of 72mm and length of 60mm.

#### 3.2.4 Prepared Self-made tiny Ag/AgCl Reference Electrodes for Solution Potential Measurement

To measure the solution potential more precisely, we made two tiny Ag/AgCl reference electrodes as measuring tips. And the processes about self-making Ag/AgCl reference electrodes see chapter 2(2.3).

#### 3.2.5 Gold BPE cleanness

Gold foil, which serves as BPE, cleaned in fresh piranha solution ( $\text{H}_2\text{SO}_4/\text{H}_2\text{O}_2$ , 3:1 (v/v)) at room temperature for about 5 min, rinsed with alcohol mixed D.I. water, and dried under nitrogen gas. *Caution: piranha solution is dangerous to human health and should be used with extreme caution and handled only in small quantities.* Then, the cleaned Gold BPE was placed into the electrochemical cell frames near the center using epoxy, driving electrodes were used stainless steel.

#### 3.2.6 ECL measurement

ECL light recorded using Panasonic Lumix DMC-LX3 Camera (Panasonic Corporation, Osaka Japan), and the light intensity analyzed using ImageJ2x software.

### 3.3 Results and Discussion

#### 3.3.1 Self-made Ag/AgCl reference electrodes

The criteria of a reference electrode including: (i) electrode potential should be stable, (ii) electrode should be reversible which obeys Nernst Equation, (iii) electrode should response fast to the change of environment conditions;<sup>13</sup> and the final important one is electrode should be nonpolarizable, which could mostly minimize the potential loss between the measuring tip and solution, and increase the accuracy of performance. Therefore, two Ag/AgCl reference electrodes were made to measuring the solution potential in the cell frames.

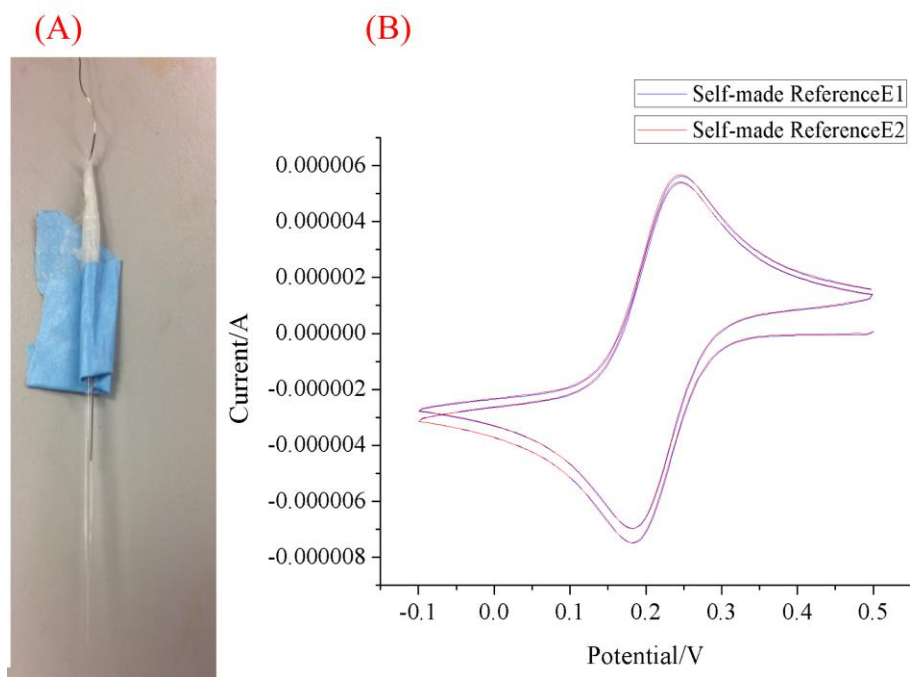


**Figure 3.3** (A) is a picture of Self-made reference electrode. (B) Cyclic Voltammograms of two self-made Ag/AgCl reference electrodes, Pt electrode as counter electrode, Au electrode as working electrode, scan in 2 mM Potassium Ferricyanide (III) solution from 0.5 volt to (-0.1) volt with 0.5 M  $\text{KNO}_3$  as supporting electrolyte, scan rate: 50 mv/s (Red and blue CV scanned using two self-made electrodes).

To verify the self-made reference electrodes working properly, cyclic voltammograms obtained by using two different self-made reference electrodes as reference electrode scanned in ferricyanide (III) solution from 0.5V to (-0.1)V with 0.5 M KNO<sub>3</sub> as supporting electrolyte, as shown in Figure 3.3, the cyclic Voltammograms, red and blue overlapped together, and are undistinguishable, indicates that the two self-made reference electrodes working properly, are good enough for solution potential measurement.

### 3.3.2 Closed cell frames versus open cell frames

To achieve solution potential measurement more convenient, accurate, and easier to compare, the cell frame was evenly separated sixteen columns with 4.5mm distance next to each line and twelve rows with 5mm distance of each row, as illustrated in Figure 3.4(A), solution potential across 10 mm, the two self-made reference electrode tips would be placed in the two green dots position, solution potential across 40 mm, the two self-made reference electrode tips would be placed in the two blue dots position, etc. Using this way, the solution potential profile of closed cell frame (Figure 3.2(B)) and open cell frame (Figure 3.2(A)) achieved at different measuring distance and applied voltage, as demonstrated in Figure 3.4(B), the potential profile contains five layers, the potential on each layer obtained under a fixed applied voltage, from low to high, 3V, 4V, 5V, 6V, and 7V, respectively; each layer contains five horizontal lines and seventeen vertical lines, as for the horizontal lines, for example, 3V4 meaning potential measured across 4cm distance under 3V applied voltage, etc., in terms of vertical lines, which meaning the potential measured at different position of the cell frame, it corresponding the seventeen vertical lines showed in Figure 3.4(A). And Figure 3.4(B) clearly indicates that the potential from closed cell frame more uniform, all the potential located same line that parallels with the driving electrode are same, and also slight higher than that from the open cell frame obtained under same measuring condition; while the

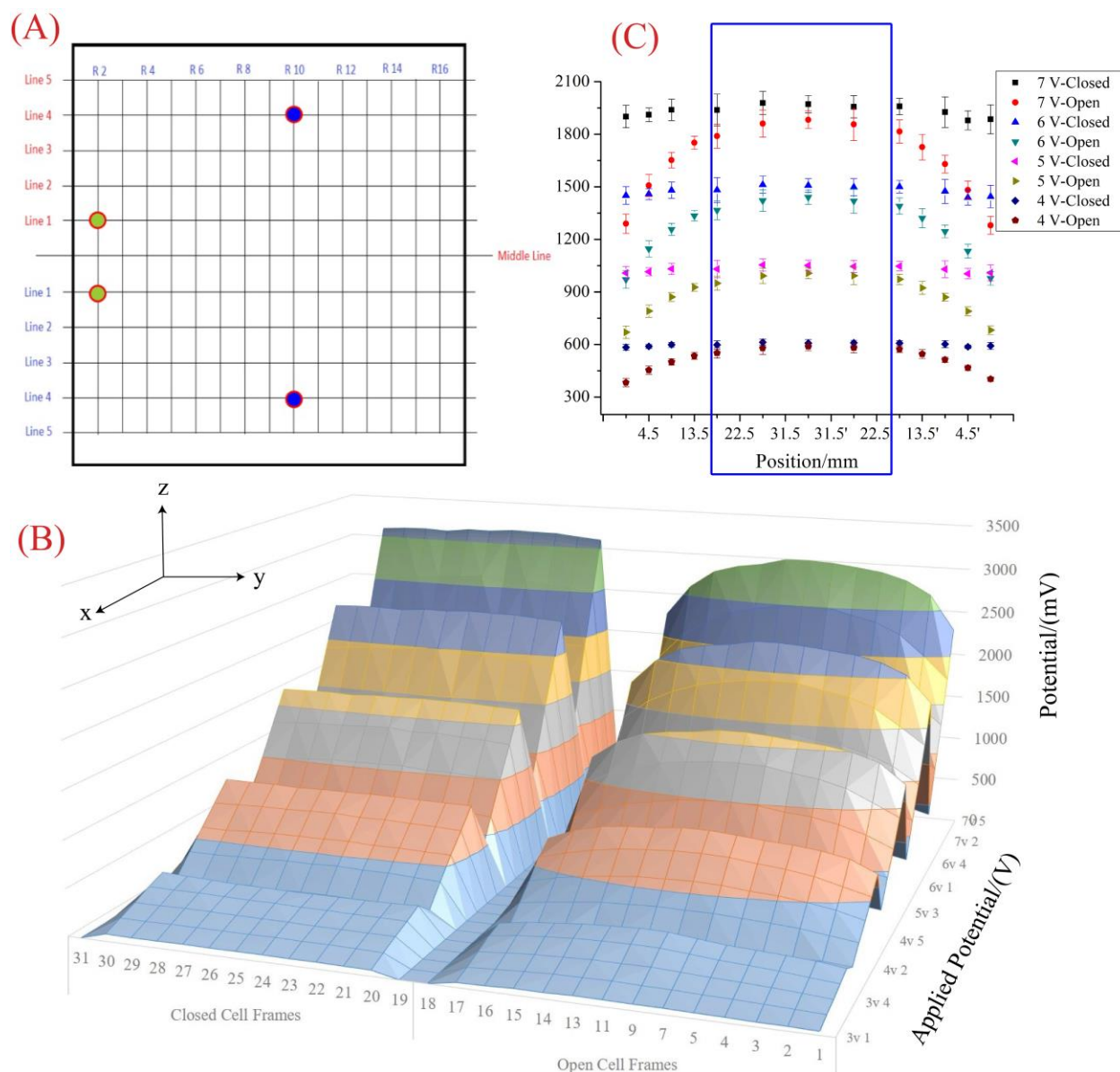


**Figure 3.4** (A) Solution potential measurement scheme; (B) solution potential profile of closed cell frames vs open cell frames; (C) solution potential profile of closed cell frames vs open cell frames at different applied voltage under 30 mm measuring distance.

potential from the open cell frame higher in the middle, and slight decreasing as the measuring position moves from middle to edges. It is reasonable, as demonstrated in Figure 3.1, the electric field strength of solution in closed cell frame is uniform, while the electric field strength decreasing and the electric lines become less dense from middle to edges of the open cell frame. From Figure

3.4(C), which shows the potential profile from closed cell frame and open cell frame measured at 30mm distance with different applied voltage, we also can see the potential from the closed cell frame is a little higher than that of open cell frame, and the potential difference between middle and edge is increasing as increasing the applied voltage using the open cell frame, which caused by increased electric field strength as increasing applied voltage. Therefore, a closed cell frame would be preferred compared to open cell frame, if open cell frame was needed to use, to ensure a relative uniform and stable potential, the BPE width should be not wider than 1/3<sup>rd</sup> width of the driving electrode.

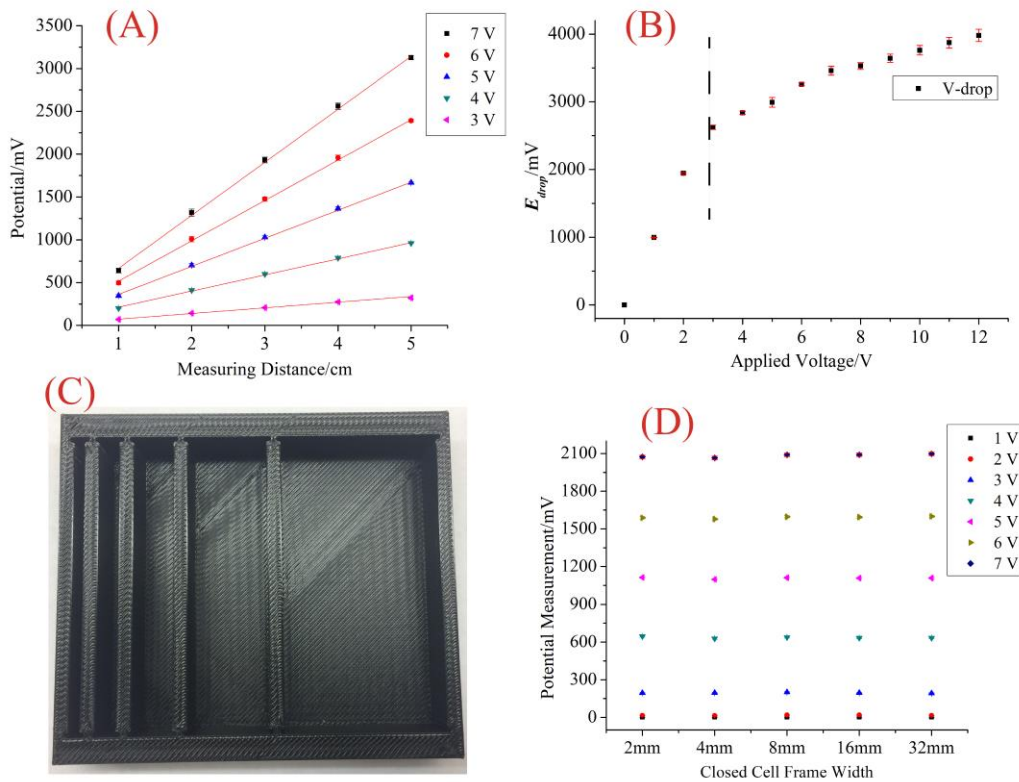


**Figure 3.5** (A) Solution potential as a function of measuring distance under different applied voltage using closed cell frames; (B) dropped potential at different applied voltage in the closed cell frame;(D) potential profile in different closed cell frame width under different applied voltage measured at 30mm distance using (C) cell frame design.

To better understand solution potential profile in the closed cell frame, solution potential as a function of measuring distance under different applied voltage was plotted in Figure 3.5(A), as indicates, the solution potential shows a linear relationship with measuring distance, and the slope of the line increases as increasing the applied voltage, which contributes to the uniformed electric field strength. In terms of voltage/potential drop, which is the applied voltage subtracts the solution potential across the cell, as illustrated in Figure 3.5(B), applied voltage smaller than 3V, non-faradic current plays a important role, the applied voltage mainly contributes to the formation of double layer at the surface of driving electrodes, nearly no voltage across the solution (or most of applied voltage acts as potential drop) since any reaction happens need to reach their redox potential; when the applied voltage larger than 3V, the slope of potential drop is decreasing, indicates most of increased voltage employs the increase of solution potential across the cell frame. To study the effect of cell frame width for the potential profile, solution potential profile achieved using cell frames with different width (Figure 3.5(C)) under different applied voltage at same measuring distance, as demonstrated in Figure 3.5(D), the solution potentials are almost same under 2mm, 4mm, 8mm, 16mm and 32mm cell frame width at a fixed applied voltage, indicates cell frame width does not affect the potential profile using the closed cell frame, probably due to the voltage drop at electrode surface for overcome double layer capacitance, charge transfer resistance, and diffusion impedance is same.

### 3.3.3 Effect of Measuring tip depth and Concentration of electrolyte

The effect of reference electrodes tips depth in solution and concentration of electrolyte when perform potential measurement also studied. The potential as a function of applied voltage collected when the measuring reference electrode tips immersed in solution ca. 3mm (shallow), 6mm (middle), and 10mm (deep), as demonstrated in Figure 3.6(A), the potential measured in

three different depth overlapped together, indicates the measuring reference electrode tip depth in solution has no effect for interfering the accuracy of collected solution potential. Meanwhile, the potential profile in 1mM, 10mM, 100mM, 1M, 2M, and 4M concentrated  $\text{NaClO}_4$  electrolyte solution under different applied voltage were measured, as shown in Figure 3.6(B), the solution potentials, which collected under same measuring distance and same applied voltage, increasing as electrolyte concentration varies from low to high. This behavior was ascribed to lower the concentration of electrolyte maybe decrease the unit double layer capacitance and increase the charge transfer at the driving electrode surface, not caused by the solution resistance across the cell since the cell frame width (or solution resistance across the cell) has no interference for the solution potential profile, as discussed above.

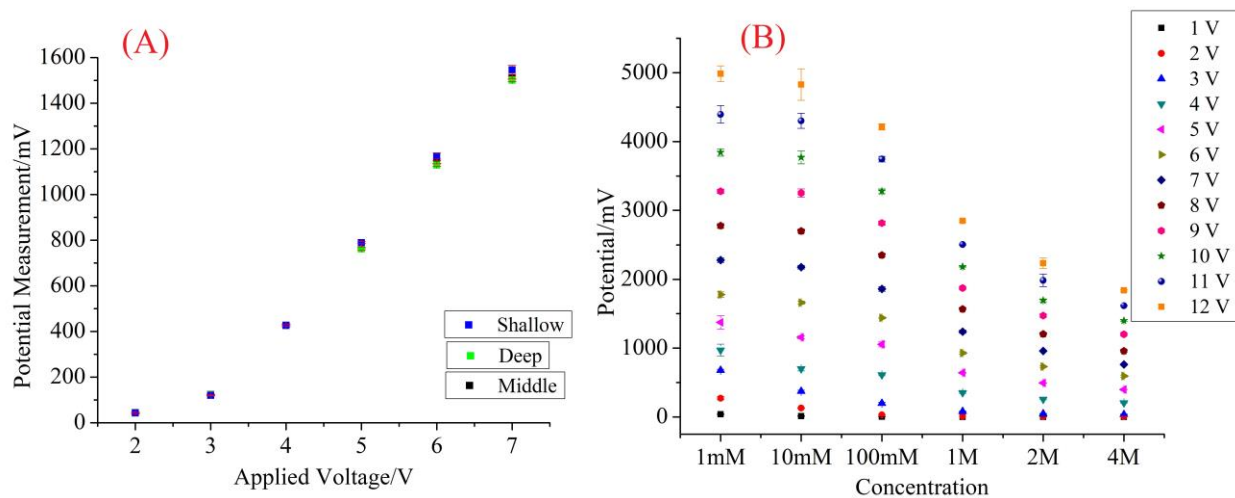


**Figure 3.6** (A) Potential profile of different measuring tip depth under different applied voltage at a fixed measuring distance; (B) potential profile of different concentrated electrolyte under different applied voltage at same measuring distance.

### 3.3.4 Study of Potential Profile using Channel Cell Frames

As for the channel cell frames used for BPE system, the effect of channel position for the potential were discussed in this section, three types of cell frames were used, where the channel

located in the middle, 1/4<sup>th</sup> of cell width to the cell side edge, and next to the side edge, as showed in Figure 3.7(A)- (C), all channels in three types of cell frames are same length, and potential profile was collected using these three types of cell frames under different applied voltage, as illustrated in Figure 3.7(D), the potential across the channel is slight increasing as the channel varies from edge to middle of the cell frame, and this behavior becomes more obvious as applied voltage increasing, especial after 4V. This phenomenon was ascribed to the solution resistance at a fixed applied voltage since the solution resistance between driving anode and cathode decreasing as the channel varies from edge to middle in cell frames. Therefore, the channel should be placed in the middle of the cell frames when a channel cell frame chosen to use in BPE cell.

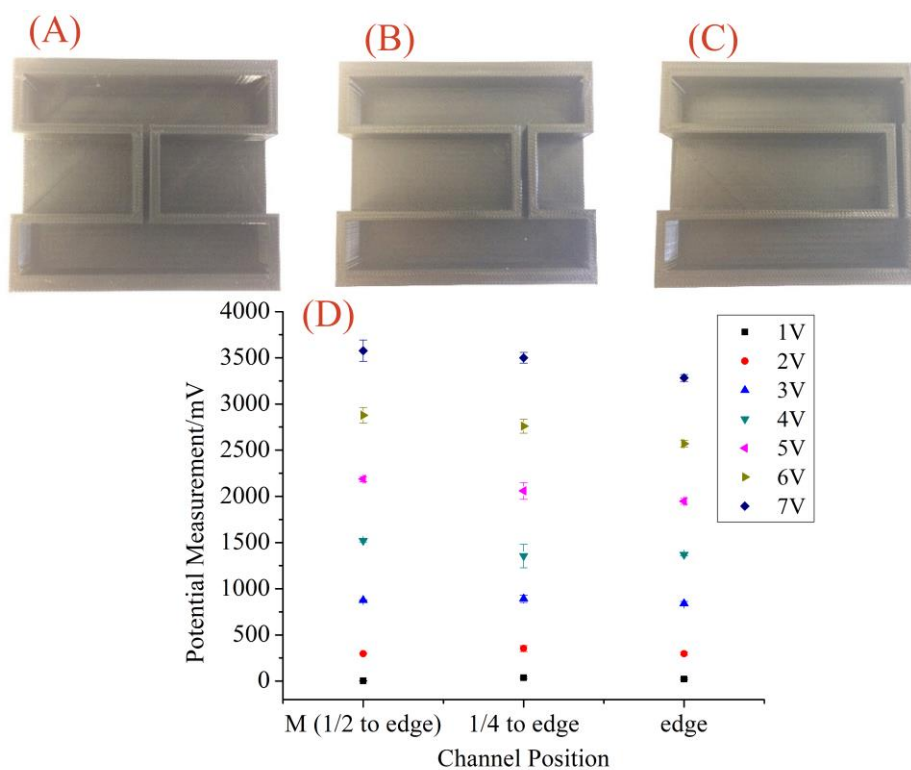


**Figure 3.7 (D)** Channel potential as function of channel position under different applied voltage by using (A), (B) and (C) cell frames, channel with 30mm length  $\times$  2mm width.



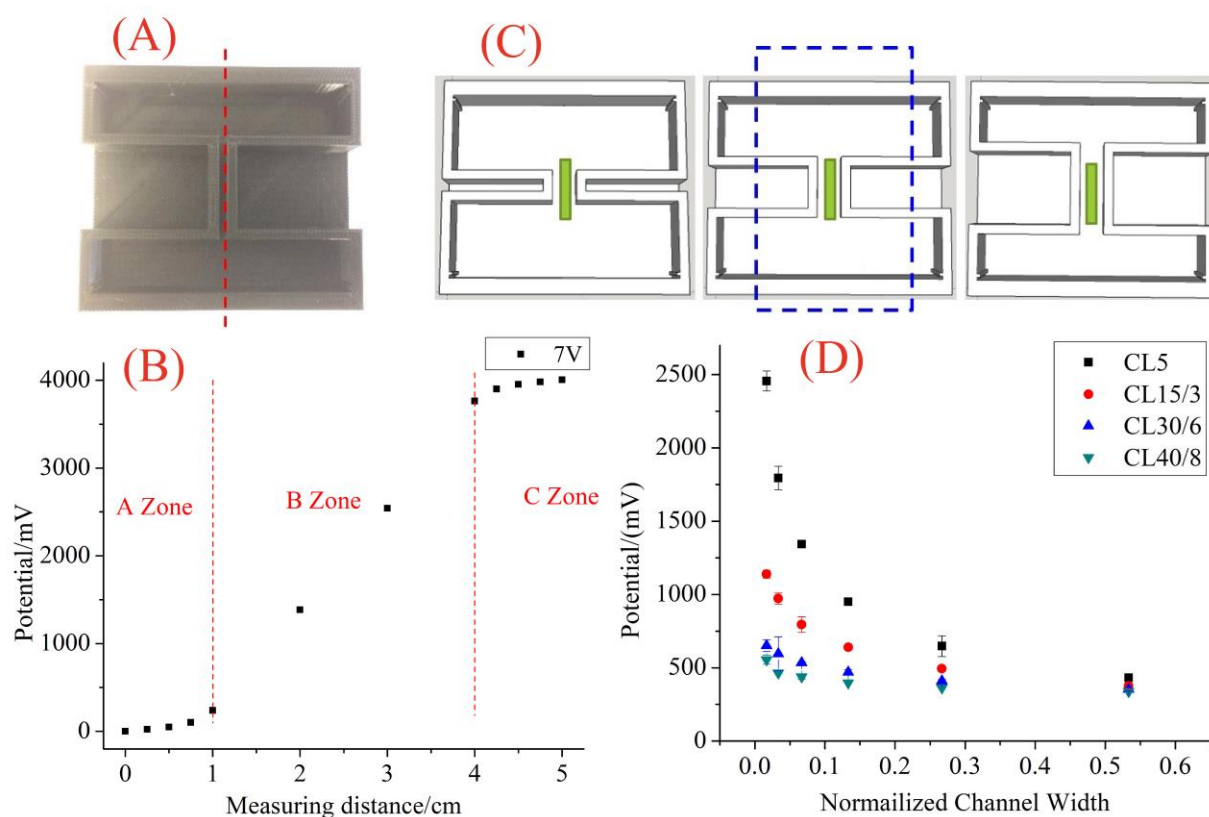


**Figure 3.8** (B) Potential profile along the red line using (A) cell frame under 7V applied voltage, channel with 30mm length  $\times$  2mm width; (C) Scheme of BPE (green color) placed in three different channel cell frames, BPE length is larger, equal, and smaller than that of the channel, respectively; (D) BPE (5mm) potential as a function of channel width with different channel length (5mm, 15mm, 30mm and 40mm, respectively) under 7V applied voltage (CL x/y meaning potential across x mm channel divided by y).

Due to the purpose of cell frames design is used for BPE system, does the length of BPE should be longer, equal, or shorter than that of channel (as shown in Figure 3.8 (C))? Therefore, a potential gradient was measured in the middle of cell frame across the channel at 7V applied voltage, as illustrated in Figure 3.8 (A)-(B), the solution potential along the red line from Figure 3.8(A) contains three parts, two parts from two reservoirs (presented in A zone and C zone), one

from the channel (B zone with 30mm channel length). And we can see the potential gradient or slope in the channel is much larger than that of the reservoir, indicates BPE should not longer than the channel to use maximum voltage efficiency on the BPE. Now it leaves BPE should equal or smaller than the length of channel. Thus, a 5mm BPE was chosen, potential profiles with 5mm, 15mm, 30mm, and 40mm channel length were collected at 7V applied voltage, and plotted as a function of normalized channel width (defines channel width divided by cell width), as shown in Figure 3.8(D), CL5 defines potential across 5mm channel length, CL15/3 defines potential across 15mm channel length divided by 3, etc., hence, the potentials shown in Figure 3.8(D) measured across same length, and the potential is higher in plot CL 5 than that from other plots, indicates the BPE placed in the channel with same length has higher voltage and the channel should be designed same length of BPE.

To further understand the potential profile along with different channel width and length, the potential profile as a function of normalized channel width (channel width divided by cell width) using different length of channel at 7V were collected and plotted in Figure 3.9(A), as it shows the potential increases as increasing the channel length under same channel width, and the potential increase becomes more obvious at same channel length when the normalized channel width not larger than 0.2, which indicates the normalized channel width should not larger than 0.2 to better increase potential across the BPE in the channel cell frame design. Meanwhile, the potential profile as a function of normalized channel length (channel length divided by cell length) using different length of channel at 7V were also collected and plotted in Figure 3.9(B), indicates normalized channel length should not smaller than 0.4 to maintain the potential across BPE at least 60% solution potential across the cell, and also not larger than 0.8 to avoid the interference from the reactions happening at the driving electrode. Therefore, to make a better channel cell frame

design/fabrication and increase the potential across the BPE, the normalized cell width should not larger than 0.2 and normalized cell length should keep in the range of 0.4 to 0.8. And the optimized conditions were presented in the red area in Figure 3.9(C).

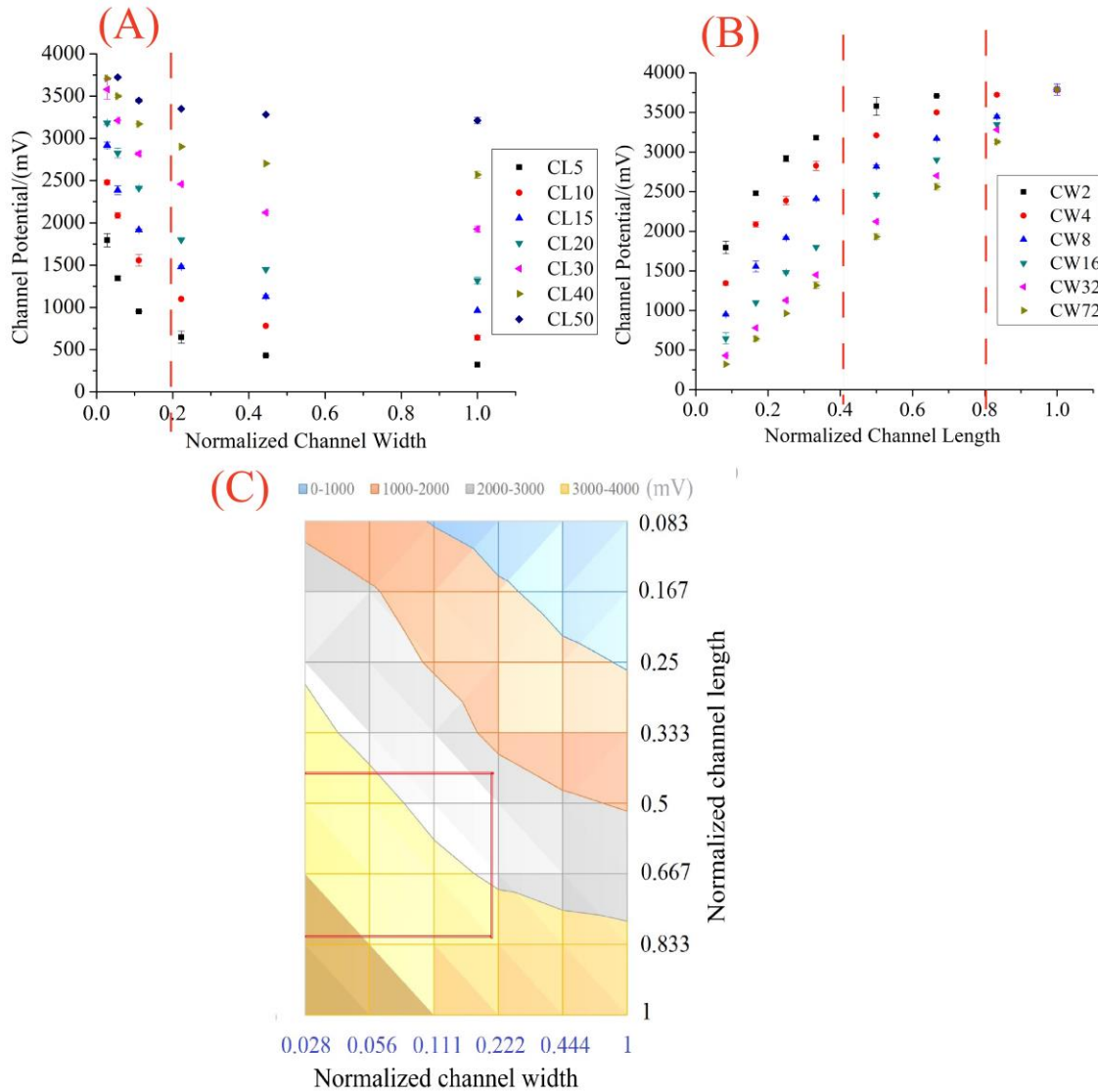


**Figure 3.9** (A) Potential profile across the channel as function of normalized channel width under different channel length with 7V applied voltage; (B) Potential profile across the channel as function of normalized channel length under different channel width with 7V applied voltage; (C) Measured potential profile across the channel (top view) as function of normalized channel width and length with 7V applied voltage.

One import case should be noticed that in the channel cell frame design, the potential profile in the channel is not that uniform. The potential across the channel length is slight larger when measurement close to the edge of channel, and potential is smallest in the middle of channel, as illustrated in Figure 3.10(A), where the potential at edge and middle of the channel measured in different width of channel under different applied voltage, and the potential difference between the edge and middle increases as increasing channel width. For example, the potential at different channel position measured under 7V applied voltage using channel with 32mm width and 30mm length of cell frame, as illustrated in Figure 3.10(B), the edge potential ca. 350mV larger than that of middle. This behavior was due to the high electric field strength at the edge compared the middle of the channel, as demonstrated in Figure 3.1(C), electric field lines much denser at channel edge while loose in the middle of the channel.

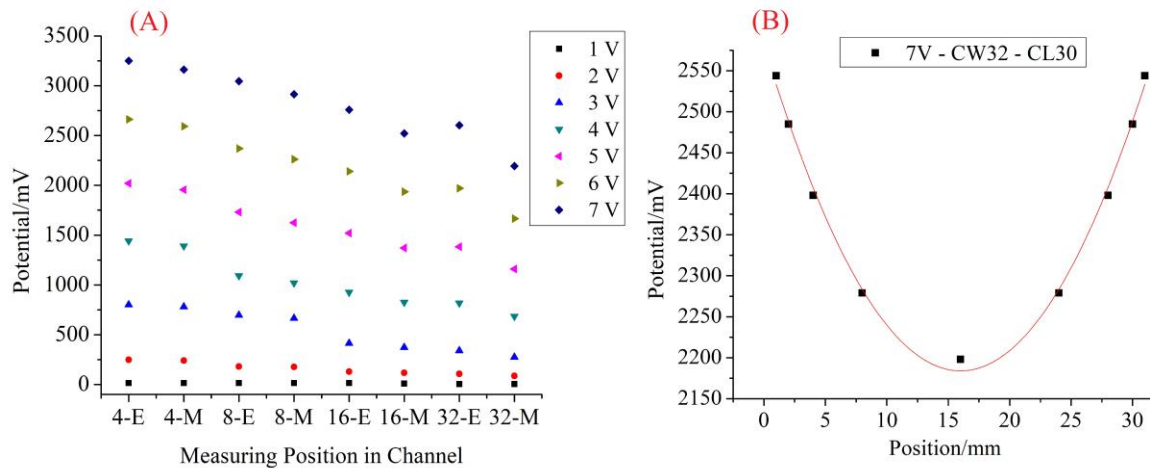


**Figure 3.10** (A) Potential profile (across 30mm channel length, measured close to channel edges and located the middle of channel) as a function of channel width under different applied voltage; (B) Potential profile measured at different position across the channel of 32mm channel width under 7V applied potential.

### 3.3.5 Model the Potential of Channel Cell Frames

To predict and better understand the potential profile of BPE across the channel, the solution was considered as ideal conductor since the concentration of electrolyte used is 0.1M that not low for ions movement in solution to have a better conductivity, and also for better calculation, a simple model was built to describe the potential across the BPE that is placed in the channel, and the calculation shows below:

$$V_{app} = V_{cathodic\ drop} + V_{anodic\ drop} + V_{channel} + V_{reservoir1} + V_{reservoir2}$$

where  $V_{reservoir1} = V_{reservoir2} = V_r$ , assume  $V_{cathodic\ drop} + V_{anodic\ drop} = V_d$  and is constant since the potential drop at electrode surface not depends on solution resistance caused by different cell frame structure when not changing the concentration of electrolyte and composition, which already discussed above,

$$V_{app} = V_d + 2V_r + V_c$$

Where  $V_{app}$  is applied voltage,  $V_c = V_{channel}$  is the potential across the channel in cell frame, since  $V$  (voltage) is proportional of solution resistivity,

$$V_c = (V_{app} - V_d) * R_c / (2R_r + R_c) = b * R_c / (2R_r + R_c) \quad (3.0)$$

Where  $p = (V_{app} - V_d)$ ,  $R_r$  is the resistance of solution in reservoir located at the end of channel next to driving electrode, and  $R_c$  is the solution resistance in the channel, if consider solution as ideal conductor,

$$R_c = \rho * \frac{l}{A_c} = \rho * \frac{l}{w_c * h}, R_r = \rho * \frac{0.5(L-l)}{A_r},$$

Where  $\rho$  is resistivity,  $W$  is cell width,  $L$  is cell length,  $l$  is channel length,  $w_c$  is channel width,  $A_c$  is the area of cross section of channel,  $h$  is the solution depth,

(1) Assume the  $R_r$  of the solution in reservoir is a rectangle resistor, then

$$V_c = p^* R_c / (2R_r + R_c) = p^* \left( \rho^* \frac{l}{w_c * h} \right) / \left( \rho^* \frac{L-l}{W * h} + \rho^* \frac{l}{w_c * h} \right) = \frac{pWl}{w_c L + (W - w_c)l}$$

$$= \frac{p^* \left( \frac{l}{L} \right)}{\left( \frac{w_c}{W} \right) + \left( 1 - \left( \frac{w_c}{W} \right) \right) * \left( \frac{l}{L} \right)} = \frac{p^* x_l}{x_w + (1 - x_w) * x_l}$$

Where  $l/L = x_l$ ,  $\frac{w_c}{W} = x_w$ , if  $V_c = y$ , then potential across the channel is:

$$y = \frac{p^* x_l}{x_w + x_l - x_w * x_l} \quad (0 < x_l < 1, 0 < x_w < 1) \quad (3.1)$$

Where  $y$  is channel potential,  $x_w$  is normalized channel width, and  $x_l$  is normalized channel length.

(2) Assume the  $R_r$  of the solution in reservoir is a trapezoid resistor, then

$$V_c = p^* R_c / (2R_r + R_c) = p^* \left( \rho^* \frac{l}{w_c * h} \right) / \left( 2 * \rho^* \frac{0.5 * (L-l)}{\frac{1}{2} (W + w_c) * h} + \rho^* \frac{l}{w_c * h} \right)$$

$$= p^* \frac{\frac{l}{w_c}}{\frac{l}{w_c} + 2 * \frac{(L-l)}{(W + w_c)}} = p^* \frac{\frac{l}{L}}{\frac{l}{L} + 2 * \frac{w_c * (1 - \frac{l}{L})}{(W + w_c)}} = p^* \frac{\frac{l}{L}}{\frac{l}{L} + 2 * \frac{(1 - \frac{l}{L})}{\left( \frac{W}{w_c} + 1 \right)}}$$

$$= p^* \frac{x_l}{x_l + 2 * \frac{(1 - x_l)}{\left( \frac{1}{x_w} + 1 \right)}} = p^* \frac{(x_l + x_w x_l)}{x_l + 2x_w - x_w x_l}$$

if  $V_c = y$ , then potential across the channel is:

$$y = p^* \frac{(x_l + x_w x_l)}{x_l + 2x_w - x_w x_l} \quad (0 < x_l < 1, 0 < x_w < 1) \quad (3.2)$$

To verify the accuracy of the two simple models that described in equation (3.1) and equation (3.2), two sets of experimental data collected at 7V applied voltage using channel frames showed

in Figure 3.11(A)-(B), and two sets of calculated data based on two models from equation (3.1) and equation (3.2) were plotted in Figure 3.11(C), as it shows, the two sets of experimental data were very close, indicates the electric field strength distributes in reservoir of the cell frame is more like in triangle or trapezoid area shape, as expected, the trapezoid calculated data from equation (3.2) more close to experimental data than rectangular calculated data since the model treated reservoir resistor as trapezoid shape. However, the trapezoid calculated data from equation (3.2) still slightly larger than experimental data, especially around 0.2 of normalized channel length, indicates  $R_r$  that used for calculation is smaller than real value based on equation (3.0), since  $R_r$  is proportional to  $(1/A_r)$ , the value of  $A_r$  used for calculation, which from trapezoid model, is larger than real one and need to be decreased. Therefore, a third model was proposed as below:

(3) An ellipse model that has a center of O, point M and N both on the ellipse was offered, as illustrated in Figure 3.11(D). Due to the problem to cause large potential differences between calculated data and experimental one from all the models is the determination of  $R_r$ , and  $R_r$  is proportional to  $(1/A_r)$ , thus  $A_r$  plays an important role for achieving the proper model. In this ellipse model, two methods were used to determine  $A_r$  and need to be verified. Since  $A_r$  is the area of cross section of solution in reservoir, which has a constant solution depth, we only need to find the length of the cross section. As illustrated in Figure 3.11(D), the length of the cross section could be line segment RH, where the line parallels with the driving electrodes and goes through the midpoint G of line segment MF, or line segment ST, which also parallels to the driving electrodes with point T is the midpoint of arc MN. Therefore, to determine the length of RH or ST, both need to acquire function of ellipse. Refers to the assumed ellipse goes  $M(0, L/2)$  and  $N(\frac{w_c - W}{2}, \frac{1}{2})$ , and the determined function of ellipse, no matter foci on x axis or y axis, presents as below:

$$\frac{4(L^2-l^2)x^2}{L^2(W-w_c)^2} + \frac{4y^2}{L^2} = 1 \quad \left( |x| < \left| \frac{W-w_c}{2\sqrt{1-x_1^2}} \right|, 0 < x_1 < 1 \right) \quad (3.3)$$

a) Channel potential profile model based on RH. To find out length of RH, from  $H(x, \frac{L+1}{4})$  and

place  $y$  value of  $\frac{L+1}{4}$  into equation (3.3), we can acquire  $x = \frac{w_c-W}{4} \sqrt{\frac{3L+1}{L+1}}$ , then obtain the length of

RH is  $(W - \frac{W-w_c}{2} \sqrt{\frac{3L+1}{L+1}})$ , put it into  $R_r = \rho^* \frac{0.5(L-1)}{A_r} = \rho^* \frac{0.5(L-1)}{RH \times h}$  and substitute it into equation (3.0),

rearrangement, and obtains the final equation for the model,

$$y = p^* \frac{2x_1 \sqrt{1+x_1-x_1(1-x_w)} \sqrt{3+x_1}}{2x_w(1-x_1) \sqrt{1+x_1} + 2x_1 \sqrt{1+x_1-x_1(1-x_w)} \sqrt{3+x_1}} \quad (0 < x_1 < 1, 0 < x_w < 1) \quad (3.4)$$

b) Channel potential profile model based on ST. The length  $s$  of arc given by  $s = \int ds$ , where  $ds =$

$dx(1+y'^2)$ , where  $y' = \frac{dy}{dx}$ . Thus, the length of arc between  $x = x_1$  and  $x = x_2$  shows as:

$$s = \int_{x_1}^{x_2} \sqrt{(1+y'^2)} dx \quad (3.5)$$

Therefore, differential of equation (3.3) and alternative we can obtain

$$y'^2 = \frac{4(L^2-l^2)^2 x^2}{L^2(W-w_c)^4 - 4(W-w_c)^2(L^2-l^2)x^2} = \frac{4a^2 x^2}{L^2 b^2 - 4abx^2} = \frac{4x^2}{L^2 c^2 - 4cx^2} \quad (3.6)$$

Where  $a = L^2-l^2$ ,  $b = (W-w_c)^2$ ,  $c = b/a$ , to find out the length of arc NM showed in Figure 3.11(D), combine equation (3.5) and equation (3.6),



$$\begin{aligned}
s(\text{Arc NM}) &= \int_{-\frac{\sqrt{b}}{2}}^0 \sqrt{1 + \frac{4x^2}{L^2c^2 - 4(cx^2)}} dx \\
&= \frac{\sqrt{1 - \frac{b}{L^2c}} \sqrt{1 - \frac{1}{c} + \frac{L^2}{-b + L^2c}} \text{EllipticE}\left[L\sqrt{\frac{1}{L^2c}} \sqrt{c} \text{ArcCsc}\left[\frac{L\sqrt{c}}{\sqrt{b}}\right], \frac{-1+c}{c}\right]}{2\sqrt{\frac{1}{L^2c}} \sqrt{\frac{b-bc + L^2c^2}{L^2c^2}}} \\
&= \frac{1}{2} L\sqrt{c} \times \text{EllipticE}\left[\text{ArcCsc}\left[\frac{L\sqrt{c}}{\sqrt{b}}\right], \frac{-1+c}{c}\right] \quad (3.7)
\end{aligned}$$

Assume T (x<sub>0</sub>, y<sub>0</sub>), which is the midpoint of arc NM, same way we can have the length of arc TM,

$$\begin{aligned}
s(\text{Arc TM}) &= \int_{x_0}^0 \sqrt{1 + \frac{4x^2}{L^2c^2 - 4(cx^2)}} dx = -\frac{1}{2} L\sqrt{c} \\
&\quad \times \text{EllipticE}\left[\text{ArcSin}\left[\frac{2x_0}{L\sqrt{c}}\right], \frac{-1+c}{c}\right] \quad (3.8)
\end{aligned}$$

Due to length of arc NM is two times of the length of arc TM, combine equation (3.7) and equation (3.8), we can have

$$\begin{aligned}
&\left| \text{EllipticE}\left[\text{ArcCsc}\left[\frac{L\sqrt{c}}{\sqrt{b}}\right], \frac{-1+c}{c}\right] \right| \\
&= 2^* \left| \text{EllipticE}\left[\text{ArcSin}\left[\frac{2x_0}{L\sqrt{c}}\right], \frac{-1+c}{c}\right] \right| \quad (x_0 < 0) \quad (3.9)
\end{aligned}$$

By using the Mathematica and Wolfram Alpha software could not solve out x<sub>0</sub>, even though we could not make further calculation to obtain the final modeling function, the way to calculate it is obvious, after x<sub>0</sub>, then achieve the length of ST showed in Figure 3.11(D), followed by substitution of it into equation (3.0) and alternate to have the final modeling function.

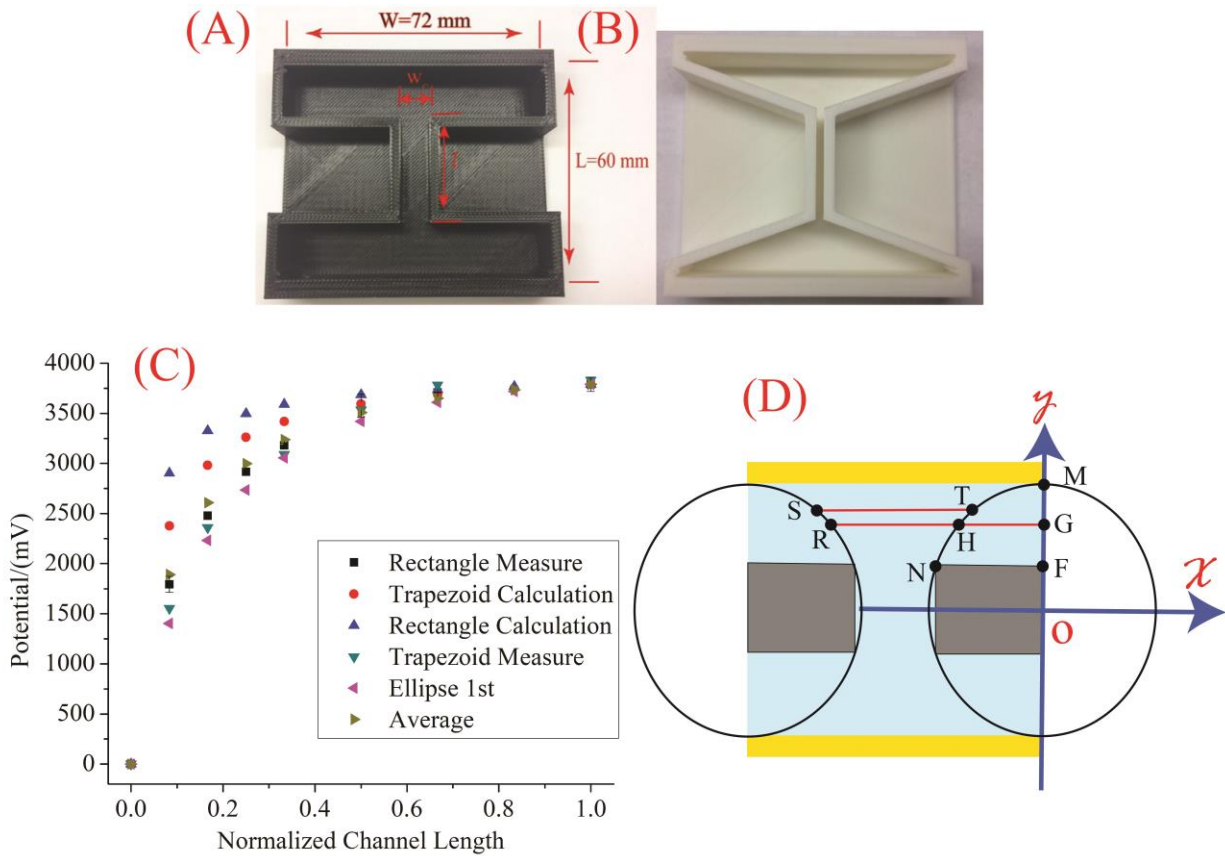


**Figure 3.11** (C) Channel potential profile as a function of normalized channel length using (A), (B) types of cell frames, and four calculation methods, channel width 2mm with 7V applied voltage; (D) Simple scheme used for describing potential modeling calculation of ellipse.

Therefore, to achieve a reasonable modeling function for predicting potential profile of channel cell frame, a final function was determined to use by averaging modeling potential function equation (3.2) and equation (3.4) for most close to the experimental measured data, as Figure 3.11(C) demonstrates, average data (dark yellow dots) is very close to real experimental data acquire from rectangular reservoir channel cell compared with calculated ellipse 1<sup>st</sup> data (magenta dots). And the final determined, easy to calculated and reasonable modeling potential function shows below in equation (3.10),

$$y = p^* \frac{1}{2} \left[ \frac{2x_1 \sqrt{1+x_1} - x_1(1-x_w) \sqrt{3+x_1}}{2x_w(1-x_1) \sqrt{1+x_1} + 2x_1 \sqrt{1+x_1} - x_1(1-x_w) \sqrt{3+x_1}} + \frac{(x_1+x_w x_1)}{x_1+2x_w-x_w x_1} \right] \quad (0 < x_1 < 1, 0 < x_w < 1) \quad (3.10).$$

### 3.3.6 ECL Comparison using Closed Cell Frame and Channel Cell Frame

To verify using channel cell frame could lower down applied potential to cause same redox reaction happens on BPE under same condition, ECL experiments was employed in BPE system using channel cell frame, which has a 2mm channel width and 30mm length, and closed cell frame. And BPE used a gold foil. As illustrated in Figure 3.12(A), the initial potential (defined as smallest applied potential on driving electrodes to cause redox reaction happens on BPE) to emit ECL on BPE is ca. 3.8V using the channel cell frame, while ca. 6V using closed cell frame, indicates using channel cell frame does lower applied potential for increasing current density or electric field strength.

And from Figure 3.12(B)-(C), which plotted the gray value (or ECL intensity) crossing the anodic driving electrode acquired from closed cell frame and channel cell under 4V applied potential, respectively, we can clearly observe a flat gray value line (Figure 3.12(B)) from using closed cell frame, which indicates a uniform solution potential distribution in closed cell frame, a gray value curve similar the model shape from ellipse 2<sup>nd</sup>, which further assured the right model we built to describe the potential crossing the channel.

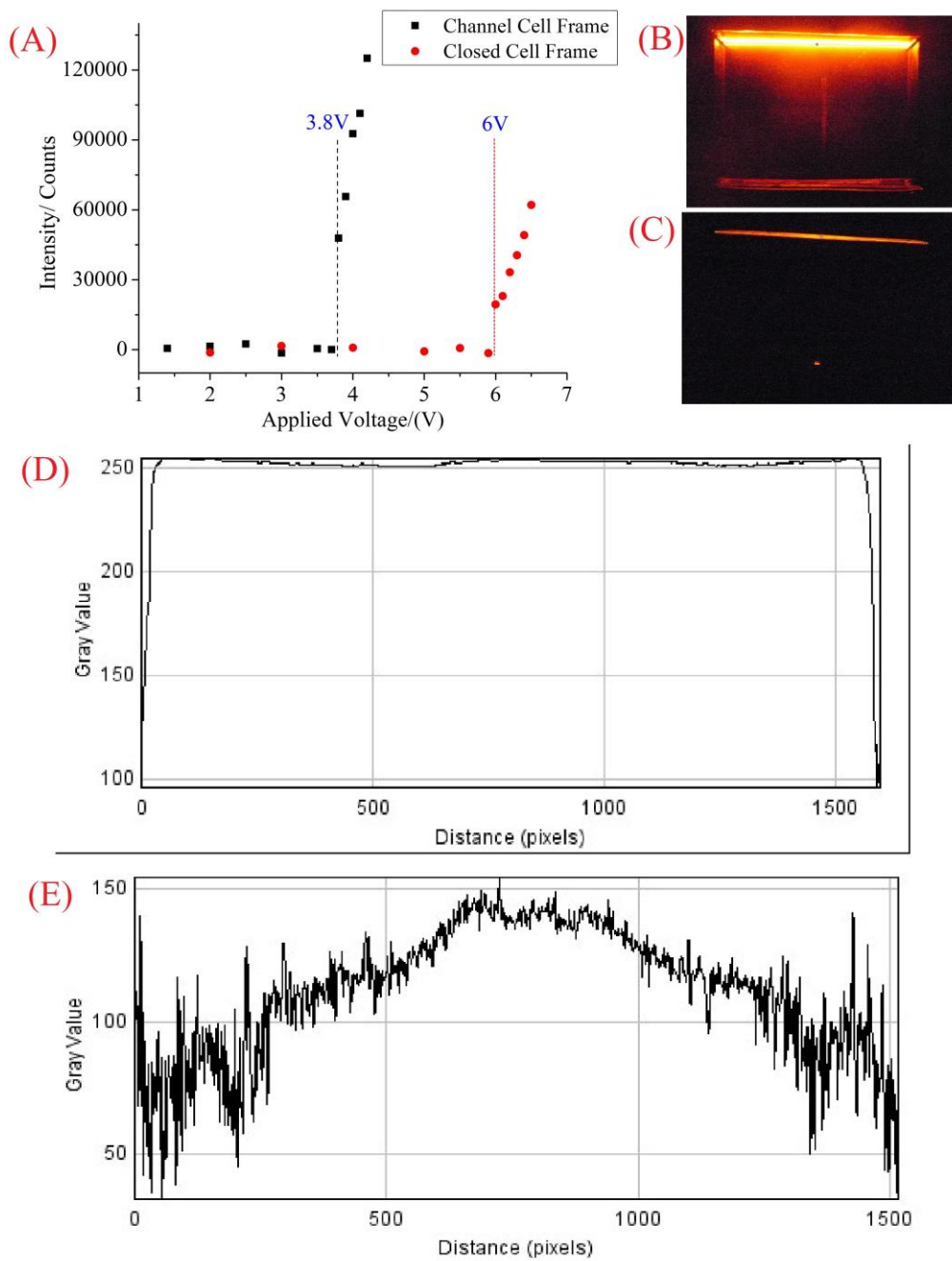


**Figure 3.12** (A) ECL intensity at different applied voltage by using closed cell frame (B) and channel cell frame (C), 2mm channel width and 30 mm length, Au foil BPE with a length of 30mm; (B) and (C) is closed cell frame and channel cell frame under 4V applied voltage, respective, and (D) and (E) is the corresponding surface plot of gray value (or ECL intensity) crossing the anodic driving electrode.

### 3.3.7 Multiple BPEs Cell Frames Design

Since we already discussed the potential profile of one channel cell frame and have known how to make an optimal fabrication of it, multiple channels (BPEs) cell frame would be studied in this small section. And for multiple BPEs in one cell frame, two alignment would be demonstrated, one is BPEs in a line arrangement, the other is BPEs in parallel arrangement.

In terms of BPEs in a line arrangement, two kinds of cell frames were offered to discuss, as showed in Figure 3.13(A)-(B), herein, three BPEs with each one 6mm length were used as an example, in Figure 3.13(A), three BPEs were placed in three small channel with same length of BPE, two small reservoirs with length of 6mm (distance between black and red dot) to separate the channels, thus, three BPEs totally covering 30mm length; as for comparison, the channel cell frame showed in Figure 3.13(B) also has a 30mm channel length. And BPE crossing potential as a function of applied potential presented in Figure 3.13(C),  $(C-30)/5$  defines as potential of channel (B) divided by 5; Small C-6 defines as potential across small channel from cell frame (A) (red and blue dot); Small R-6 defines as potential across small rectangular reservoir from cell frame (A) (red and black dot); therefore, three potential profile (black, red, and blue curve) measured across same distance of 6mm. As demonstrated in Figure 3.13(C), small C-6 curve has a higher potential than that of small R-6 since the electric field strength decreased in small R-6 caused by the big reservoir structure; small C-6 and  $(C-30)/5$  curve has similar potential when applied voltage no bigger than 4V, indicates no big potential differences when BPEs placed in cell frame (A) or cell frame (B), while after 5V, the potential from small C-6 is bigger becomes more obviously, indicates using cell frames with multiple small channels would be better than one channel for BPE system.

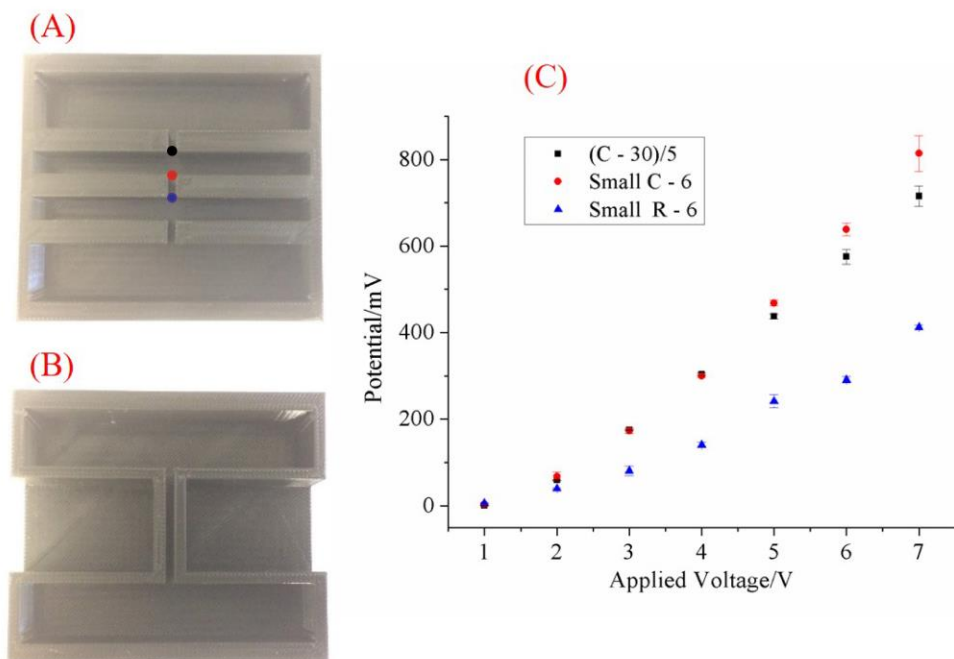


**Figure 3.13** (C) Potential profile as a function of applied voltage using cell frame (A) (three channels 2mm width  $\times$  6mm length, two rectangular reservoirs both with a 6mm length) and (B) (channel 2mm width  $\times$  30mm length); (C-30)/5 defines potential of channel (B) divided by 5; Small C-6 defines potential across center channel from cell frame (A) (red and blue dots); Small R-6 defines potential across small rectangular reservoir from (A) (black and red dots).

As for BPEs in parallel arrangement, two kinds of alignment for the channels in cell frames studied, one is the channel evenly separated distributed in the cell, with each channel toward same effectively driving electrode area, as illustrated in Figure 3.14(A), while the other is channels were closely placed in the central cell frame, as shown in Figure 3.14(B). The channel potential at different channel position under different applied voltage were measured based on the two structured channel cell frames, as demonstrated in Figure 3.14(C), the potential at different channel position exhibits similar value when using cell frame with evenly separated channels, while potential using cell frames from Figure 3.14(A) is slightly becoming bigger than that measured using cell frame (B) after 4V applied voltage, meanwhile, the potential measured in middle channel

also becomes slight lower than that from two sides channel after 4V when using cell frame (B) from Figure 3.14, and this behavior becomes more and more obvious as applied voltage varied from 4V to higher one, indicates channels should evenly separate in cell frames in order to ensure BPEs have same potential.

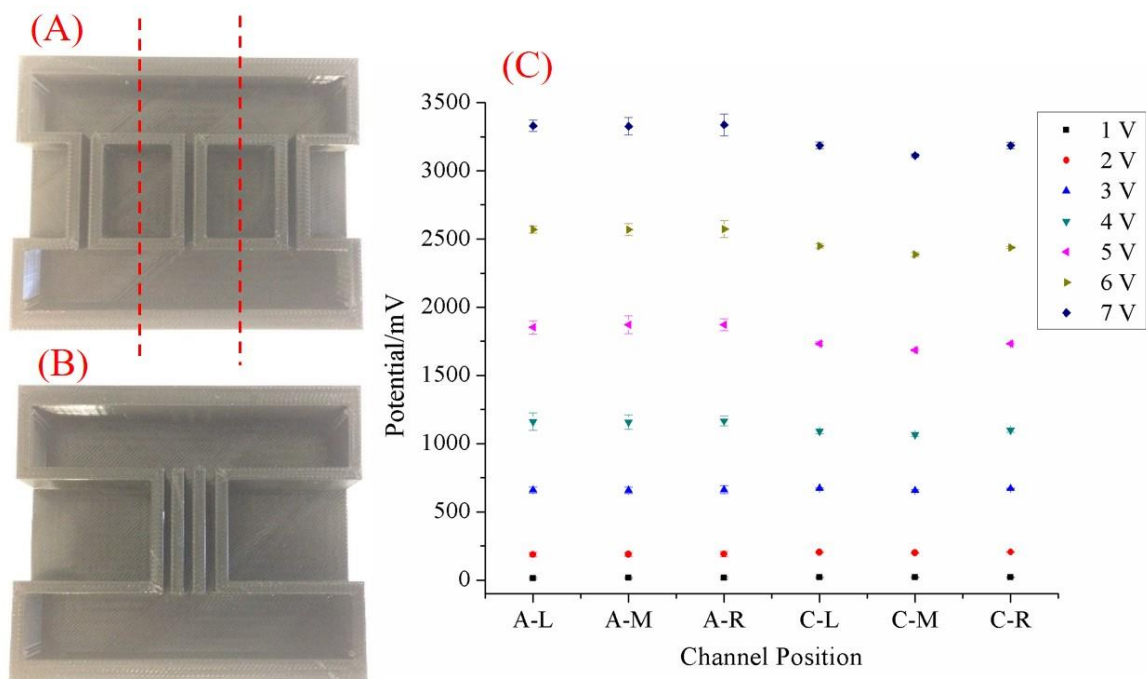


**Figure 3.14** (C) Potential measured at different channel position under different applied voltage by using cell frame (A) (channel evenly separated) and (B), all the channels 2mm width  $\times$  30mm length, A-L(M/R) defines left (middle/right) channel from cell frame (A), C-L(M/R) defines left (middle/right) channel from cell frame (B).

### 3.4 Conclusions

In this work, the potential profiles from open cell frame, closed cell frame, and channel cell frame were studied. We found that closed cell frames give an uniform potential distribution compared with open cell frames; the solution potential across the cell length does not depends on cell frame width; and closed cell frames would be a preferred choice to use in BPE system

compared with open cell frames. If open cell frames are chosen, to ensure a relative uniform and stable potential, the BPE width should be not wider than  $1/3^{\text{rd}}$  width of the driving electrode. As for channel cell frames, the potential of BPE can be enhanced or increased compared with that from using closed cell frames; to maintain the potential across BPE at least 60% solution potential across the cell, and avoid the interference from the reactions happening at the driving electrode, a optimal channel cell frame design/fabrication, the normalized cell width should not larger than 0.2 and normalized cell length should be in the range of 0.4 to 0.8; the potential across the channel is also described using several models (rectangle, trapezoid, ellipse 1<sup>st</sup> and ellipse 2<sup>nd</sup>) based on the variables of channel length and width, we find that the model of ellipse 2<sup>nd</sup> is most accurate, however, a final modeling function to predict and describe the channel potential is determined by averaging function of trapezoid and ellipse 1<sup>st</sup> for simplicity of calculation as well as acceptable accuracy.

In conclusion, this work may give a guideline to some researchers what kind of cell frame they should choose, what is the optimal cell frame fabrication for their BPE system.



## References

1. Koefoed, L.; Pedersen, S. U.; Daasbjerg, K., Bipolar electrochemistry—A wireless approach for electrode reactions. *Current Opinion in Electrochemistry* **2017**, *2* (1), 13-17.
2. Ramaswamy, R.; Shannon, C., Screening the Optical Properties of Ag– Au Alloy Gradients Formed by Bipolar Electrodeposition Using Surface Enhanced Raman Spectroscopy. *Langmuir* **2011**, *27* (3), 878-881.
3. Shannon, C.; Wang, B.; Yu, S., Reduction of 4-Nitrothiophenol on Ag/Au Bimetallic Alloy Surfaces Studied Using Bipolar Raman Spectroelectrochemistry. *ChemElectroChem* **2020**.
4. Zhang, X.; Lazenby, R. A.; Wu, Y.; White, R. J., Electrochromic, Closed-Bipolar Electrodes Employing Aptamer-Based Recognition for Direct Colorimetric Sensing Visualization. *Analytical Chemistry* **2019**, *91* (17), 11467-11473.
5. Sheridan, E.; Hlushkou, D.; Knust, K. N.; Tallarek, U.; Crooks, R. M., Enrichment of cations via bipolar electrode focusing. *Analytical chemistry* **2012**, *84* (17), 7393-7399.
6. Kumsapaya, C.; Limtrakul, J.; Kuhn, A.; Zigah, D.; Warakulwit, C., Bipolar electrografting on the inner wall of carbon nanotubes. *ChemElectroChem* **2016**, *3* (3), 410-414.
7. Gamero-Quijano, A.; Molina-Osorio, A. F.; Peljo, P.; Scanlon, M. D., Closed bipolar electrochemistry in a four-electrode configuration. *Physical Chemistry Chemical Physics* **2019**, *21* (19), 9627-9640.
8. Mavré, F.; Chow, K.-F.; Sheridan, E.; Chang, B.-Y.; Crooks, J. A.; Crooks, R. M., A theoretical and experimental framework for understanding electrogenerated chemiluminescence (ECL) emission at bipolar electrodes. *Analytical Chemistry* **2009**, *81* (15), 6218-6225.
9. Gamburg, Y. D.; Zangari, G., *Theory and practice of metal electrodeposition*. Springer Science & Business Media: 2011.

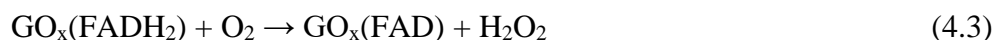
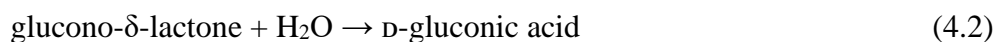
10. Markovic, N. M., Electrocatalysis: interfacing electrochemistry. *Nature materials* **2013**, *12* (2), 101-102.
11. Bard, A. J.; Faulkner, L. R., Fundamentals and applications. *Electrochemical Methods* **2001**, *2* (482), 580-632.
12. Favaro, M.; Jeong, B.; Ross, P. N.; Yano, J.; Hussain, Z.; Liu, Z.; Crumlin, E. J., Unravelling the electrochemical double layer by direct probing of the solid/liquid interface. *Nature communications* **2016**, *7* (1), 1-8.
13. Chan, S.; Chen, X.; Khor, K., Reliability and accuracy of measured overpotential in a three-electrode fuel cell system. *Journal of applied electrochemistry* **2001**, *31* (10), 1163-1170.

## Chapter 4

### Cathodic Electrochemiluminescence Glucose Biosensor Using Closed Bipolar Electrode System

#### 4.1 Introduction

Diabetes, one of the global diseases, plays a crucial part in effecting human health, and persistently high blood glucose levels may cause generalized vascular damage leading to cardiac arrest, failure function of kidney, and various complications.<sup>1</sup> It was estimated that there are 451 million (age 18–99 years) people suffering diabetes worldwide in 2017, and expected to increase to 693 million by 2045.<sup>2</sup> Therefore, screening and monitoring blood glucose, guide people on whether need seeking clinical help is very important.<sup>3</sup> Glucose oxidase (GO<sub>x</sub>), which is a hydrodynamic Metallo-flavoenzyme contains two flavin adenine dinucleotide (FAD) redox cofactors and two iron moieties, is commonly used for enzymatic glucose biosensor design because of its low cost and high sensitivity and selectivity.<sup>4-5</sup> It's been decades since Clark and Lyons<sup>6</sup> proposed the concept of glucose enzyme electrodes, which considered as first-generation glucose biosensor prototype, used oxygen to regenerate GO<sub>x</sub>(FAD) (oxidized form of GO<sub>x</sub>) and detect glucose based on monitoring consumption of oxygen or the production of hydrogen peroxide. And the reactions show as below (Eqs 4.1-4.3):



Due to Clark's design as so successful, many research and commercial biosensors have been produced by employing the original concept O<sub>2</sub> or H<sub>2</sub>O<sub>2</sub> measurement. However, the 10-fold excess of glucose over oxygen in blood that 'oxygen deficit' becomes the most serious problem

for the first generation biosensor.<sup>7</sup> Then, the so called ‘second generation’ first developed by Cass et al.<sup>8</sup> used ferrocene derivatives such as ferrocene carboxylic acid to replace oxygen as mediator, which aimed to deliver electrons between the enzyme active site and the electrode, to avoid dependence on ambient oxygen. An ideal mediator should be able to react rapidly with the reduced enzyme; exhibit reversible heterogeneous kinetics; possess reversible and stable redox forms; have a low redox potential; independent on pH and inert with O<sub>2</sub>.<sup>9</sup> And the commonly used mediators are Prussian blue,<sup>10</sup> quinones,<sup>11</sup> ferrocene and ferrocene derivatives,<sup>12</sup> viologen,<sup>13</sup> ruthenium,<sup>14</sup> etc. For the third-generation glucose biosensors are much more interesting since one of the important and fundamental concepts is mediator-free direct electron transfer between the active center of the redox enzyme and the electrode surface. However, the direct electron transfer between the redox-active cofactor (FAD) and the electrode surface is very difficult because FAD redox cofactors are deeply embedded inside the nonconducting layer of the rigid protein structure.<sup>15</sup> Therefore, many methods have proposed to overcome the challenge and achieve the direct electron transfer between the enzyme and electrodes without mediator, such as the using of conductive nanomaterials like carbon nanotubes,<sup>16</sup> TiO<sub>2</sub> nanosheets array/carbon cloth,<sup>17</sup> gold nanoparticles,<sup>18</sup> etc. Although third generation glucose biosensor has a low detection limit,<sup>18-19</sup> a lot a scientific research need to perform before lay it into practical applications.

Electrochemiluminescence (ECL), also known as electrogenerated chemiluminescence, is an electrochemical luminescence process, where the light emission initiated by the active species, which located at excited states, undergo high energy electron transfer reactions at the electrode.<sup>20-</sup><sup>21</sup> And it can be generated under anodic and cathodic conditions. *Ru(bpy)<sub>3</sub>Cl<sub>2</sub>*<sup>22</sup> and luminol<sup>23</sup> are commonly used as ECL luminophores, while in a co-reagent ECL system, tripropylamine (TPrA), persulfate ( $S_2O_8^{2-}$ ), oxalate ( $C_2O_4^{2-}$ ) commonly used as co-reagents that could form

strong reducing or oxidizing agents upon electrochemical oxidized or reduced.<sup>24</sup> Due to the low background signal, high detection sensitivity, ease of controllability, simple optical setup, without requiring extrinsic illumination, etc.,<sup>25-26</sup> ECL has been widely used for analytical applications, such as dopamine,<sup>27</sup> antigen,<sup>28</sup> glucose,<sup>29</sup> glutathione,<sup>30</sup> RNA,<sup>31</sup> and so on.<sup>32</sup>

Bipolar electrochemistry or bipolar electrode (BPE) system, is an unconventional technique where an conductive material (BPE) that is immersed into a solution (open BPE system) or two separated solutions (closed BPE system) without any wire connection with an external power source. Exploiting the wireless nature of BPEs in solutions, BPE technique used in various areas, wastewater treatment,<sup>33</sup> energy,<sup>34</sup> material catalysis,<sup>35</sup> cation enrichment,<sup>36</sup> analytical sensors,<sup>37</sup> for example. Since ECL was first introduced to BPEs for reporting electrochemical reactions in 2001,<sup>38</sup> the technique of BPE combined with ECL has attracted great attention in analytical applications.<sup>39-40</sup> For instance, a nanopipette, in which the tip are decorated by a Pt deposit used as an open BPE-ECL device, was developed by researchers<sup>41</sup> to achieve intracellular wireless electroanalysis of H<sub>2</sub>O<sub>2</sub> or glucose; Xu group reported a disposable paper-based BPE based on ECL for the detection of cancer biomarker (PSA) for the first time,<sup>42</sup> Zhang group enhanced the sensitivity of glucose sensor based on BPE-ECL through the decoration of cathodic pole of BPE with chitosan, multi-walled carbon nanotubes, graphene quantum dots and gold nanoparticles, achieved a glucose detection range of 0.1-5000uM.<sup>23</sup> However, as for many cathodic ECL systems require very negative potentials to generate light,<sup>43</sup> cathodic ECL may not that preferred compared with anodic ECL by the researchers in scientific researches. To our knowledge, any publications in terms of glucose biosensor using cathodic ECL in a closed BPE (C-ECL-C-BPE) system have not seen so far, and using a C-ECL-C-BPE system to design glucose biosensor worth to try.

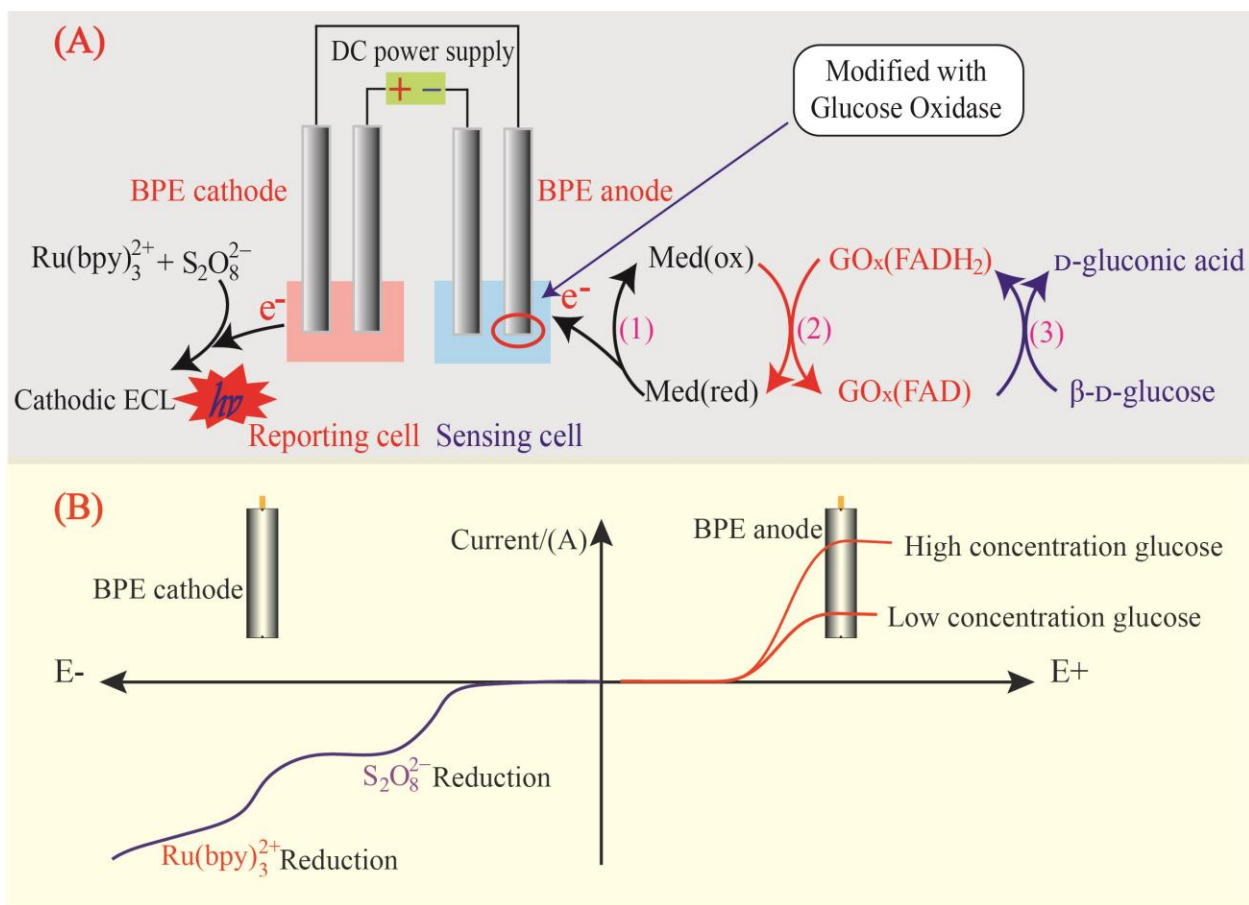
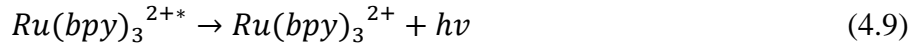
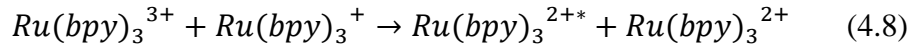
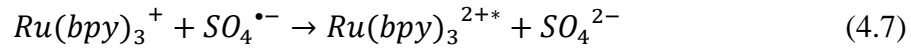
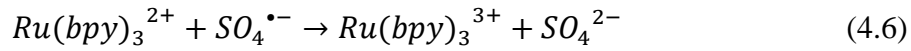
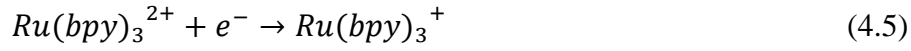


**Figure 4.1** Cathodic ECL Glucose biosensor Mechanism in Closed BPE system.

Herein, a cathodic ECL sensor in closed BPE system have been proposed for the measurement of glucose. And its basic schematic structure and operational mechanism illustrated in Figure 4.1. Compared with open BPE system, the closed BPE system is comprised of two cells, one is reporting cell that usually contains chemiluminescent and co-reagent, and the other one is sensing cell used for detecting interested analytes, which makes the reporting molecules not interfere the interested analyte during detecting performance; another main advantage of closed BPE system is the current passes through the whole system is same, which could increase the current efficiency on the BPE and lower the external applied voltage, and a lower applied voltage could further lower byproducts generation on the driving electrodes and may lead to increase the stability and sensitivity of measurement. In this report, ECL solution used  $Ru(bpy)_3^{2+}$  as luminophore,

$K_2S_2O_8$  as co-reagent, and the ECL emission on cathodic pole of BPE could be generated from the reaction between  $Ru(bpy)_3^+$  and sulfate radicals ( $SO_4^{\bullet-}$ ), the reaction between  $Ru(bpy)_3^+$  and  $Ru(bpy)_3^{3+}$  in the reporting cell, and the reactions show below (Eqs. 4.4-4.9):<sup>44-45</sup>



In the sensing cell, the commercial blood glucose test strips that already modified with  $GO_x$ (glucose oxidase) and mediator were used to detect glucose. To better illustrate the reaction processes during the measurement, two normal electrodes drawn in the sensing cell instead of commercial test strip, as showed in Figure 4.1(A). In the represent of glucose, oxidized form of  $GO_x$ , denoted as  $GO(FAD)$ , will oxidize it to gluconolactone, which will become gluconic acid in the present of aqueous condition. And at the same time,  $GO(FAD)$  is reduced to  $GO(FADH_2)$ , which will be oxidized back to  $GO(FAD)$  by the oxidized form of mediator that oxidized by the BPE anode under certain applied external voltage through a DC power supply on the sensor system. All these three reactions are describing on Figure 4.1(A). Once the glucose solution changed into higher concentration, it will accelerate these three reaction processes happening on the BPE anode, in other way, higher current would be generated. Since the glucose sensor established on the closed BPE system, the current passes through all four electrodes is same, the BPE cathode need higher current go through to compensate for the current change on the BPE anode, which means more  $Ru(bpy)_3^{2+}$  and  $S_2O_8^{2-}$  will be reduced and more  $Ru(bpy)_3^+$  and  $SO_4^{\bullet-}$  will be evolved, and

much higher intensity of ECL light will be emitted, as illustrated in Figure 4.1(B). Therefore, the cathodic ECL light intensity change as a function of glucose concentration would be established, and the cathodic ECL glucose biosensor in a closed BPE system would become reasonable and achievable in the practical way.

## 4.2 Experimental section

### 4.2.1 Chemicals and Reagents

All solutions were prepared with deionized, ultra-pure water (VWR Type II). Glucose Oxidase ( $GO_x$ ) from *Aspergillus niger* (Type X-S, lyophilized powder, 149500 units/g solid, purchased from Sigma-Aldrich), D-(+)-Glucose (99.5%, Sigma-Aldrich), Tris(2,2'-bipyridyl) dichlororuthenium(II) hexahydrate ( $Ru(bpy)_3Cl_2 \cdot 6H_2O$ ) (99.95%, Sigma-Aldrich), Acetonitrile (anhydrous, 99.8+%, Alfa Aesar), Sodium phosphate dibasic anhydrous (Sigma-Aldrich), Sodium Phosphate Monobasic (98.8%, Fisher Scientific), Sulfuric Acid (Fisher Chemical), MicroPolish Alumina (1.0 micron, 0.3 micron and 0.05 micron) and Chemomet Polishing Cloth (all purchased from BUEHLER), Capillary tubes (I.D. 1.1-1.2 mm, Wall  $0.2 \pm 0.02$  mm, Kimble Chase), Silver wire (0.25mm diameter, 99.99%, Sigma-Aldrich), Glassy carbon electrode (3mm diameter, Bioanalytical Systems, Inc.), human Serum samples (BioIVT), Potassium persulfate (Millipore Sigma), Potassium hexacyanoferrate(II) trihydrate (98.5%, Strem Chemicals), Nafion perfluorinated resin solution (5 wt% in lower aliphatic alcohols and water, contains 15-20% water, Sigma-Aldrich), hydroquinone (99%, Alfa Aesar), Glutaraldehyde solution (Grade II, 25% in  $H_2O$ , Sigma-Aldrich). Multi-walled carbon nanotubes (TCI, 10-20nm diameter, 5-15  $\mu m$  length), Multi-walled carbon nanotubes (Nanolab, 30nm diameter, 1-5  $\mu m$  length).



#### 4.2.2 Apparatus

Panasonic Lumix DMC-LX3 Camera (Panasonic Corporation, Osaka Japan), Electrochemical Potentiostat (Pine Instrument), Power supply (9122A 0-60V/0-2.5A Single Output Programmable DC, B&K Precision Corporation), PMT(photomultiplier tube) (HC-120-05 (HAMAMATSU, PhotoSensor Modules), Hantek multifunction DAQ device (USB-6002)(National Instruments), Contour NEXT EZ Diabetes Testing Kit (Contour NEXT EZ Blood Glucose Meter, Contour NEXT Blood Glucose Test Strips, Lancets, Lancing Device, Control Solution) (Amazon).

#### 4.2.3 Modification of glassy carbon electrodes (GCEs) with GO<sub>x</sub>

The glassy carbon electrodes (GCEs) were polished by using 1 micron, 0.3 micron and 0.05 micron Alumina starting with most coarse and finishing with the finest grade, followed by sonicating in EtOH and water for 5 mins, respectively, then scanned 20 cycles using cyclic voltammetry with 50 mV/s scan rate in 0.1 M sulfuric acid, and finally washed with D.I. water and dried with flowing nitrogen.

Prior to use, MWCNTs (multi-walled carbon nanotubes) were functionalized and purified by sonicating in a mixture of concentrated nitric acid and sulphuric acid (1:3, v/v) at 60 Celsius degree for 3 hours, neutralized with D.I. water and centrifuged the solution with 15000 rpm for 30min, remove the supernatant and dissolve MWCNTs in D.I. water, repeat 3 times and dried with Bella Dryer/cooler.

GCE/GO<sub>x</sub>/GA/Nafion modification: A mixed solution prepared by mixing 30  $\mu\text{L}$  GO<sub>x</sub> (1000U), 40  $\mu\text{L}$  glutaraldehyde (GA), and 50  $\mu\text{L}$  0.1M PBS buffer. 3  $\mu\text{L}$  mixed solution was put on the surface of GCE and dried under ambient condition, then 2  $\mu\text{L}$  Nafion solution was put on it

and dried under ambient condition. Finally, the modified GCE was dipped into PBS buffer under 4 Celsius degree overnight, then modified GCE ready to use.

GCE/GO<sub>x</sub>/GA/MWCNTs /Nafion modification: A mixed solution prepared by mixing 30 μL GO<sub>x</sub> (1000U), 40 μL glutaraldehyde (GA), 30 μL MWCNTs (0.5 mg/mL), and 20 μL 0.1M PBS buffer. 3 μL mixed solution was put on the surface of GCE and dried under ambient condition, then 2 μL Nafion solution was put on it and dried under ambient condition. Finally, the modified GCE was dipped into PBS buffer under 4 Celsius degree overnight before to use.

#### 4.2.4 Preparation of C-ECL-C-BPE glucose biosensor and data acquisition

For the C-ECL-C-BPE (cathodic ECL in closed BPE system) glucose biosensor, two GCEs (one electrode is anodic driving electrode, the other is cathodic BPE) used in the reporting cell through all the experiments, commercial Contour NEXT blood glucose test strip used in the sensing cell; all the ECL intensity using C-ECL-C-BPE sensor method acquired with a PMT (photomultiplier tube); after each measurement, the two GCEs rinsed with D.I. water and dried with nitrogen; all ECL solution used  $Ru(bpy)_3^{2+}$  as luminophore,  $K_2S_2O_8$  as co-reagent, prepared in 0.1M PBS buffer contains 35% (v/v) acetonitrile, pH=8, bubbled with nitrogen; all glucose solution prepared in 0.1M PBS buffer with pH=7.

Data acquisition: For ECL intensity calibration curve signal, each data point acquired the highest point from the ECL spectrum collected by PMT.

### 4.3 Results and discussion

#### 4.3.1 Effect of Acetonitrile for Cathodic ECL

Cathodic ECL is the emission of light initiated by electrochemical method produced on the cathode of electrode. As illustrated from Eqs.4-9, there are two ways to initiate the light. One is the reaction between  $Ru(bpy)_3^+$  and  $SO_4^{\bullet-}$ , and the other is the annihilation between  $Ru(bpy)_3^+$

and  $Ru(bpy)_3^{3+}$ . And the generation of  $Ru(bpy)_3^{3+}$  also contains two path ways, one is the reaction between  $Ru(bpy)_3^{2+}$  and  $SO_4^{\bullet-}$ , and the other is from the anode of driving electrode. In order to eliminate the possible interference that the ECL light may be observed on or near area of the anode of driving electrode through the diffusion of  $Ru(bpy)_3^+$ , generated on the BPE cathode, and  $Ru(bpy)_3^{3+}$ , oxidized from the driving anode, when binding the driving anode and BPE cathode together in the reporting cell, three GCEs were bound together, one is connecting positive side of a DC power supply, one is connecting negative side, and the third one is connecting nothing as a blank comparison, as indicated in Figure 4.2(A). And three GCEs immersed in ECL solution, the ECL emission can only be observed on the one connected negative DC power supply, as illustrated in Figure 4.2(B). To further rule out the ECL light may be observed on or near area of the anode of driving electrode, the light emission were collected from the three GCEs at 10 sec, 60 sec and 120 sec, as shown from Figure 4.2(C)-(E), still the ECL light can be observed only on the one connected to negative DC power supply at 3.3V applied voltage. All of these indicate ECL emission only happens on the cathodic electrode when using  $Ru(bpy)_3^{2+}$  as luminophore and persulfate as co-reagent, and  $Ru(bpy)_3^+$  generated from cathode and  $Ru(bpy)_3^{3+}$  oxidized from anode would not or not have enough time to diffuse to each other and emit the light before they were quenched by the surrounding environment under 2 mins.

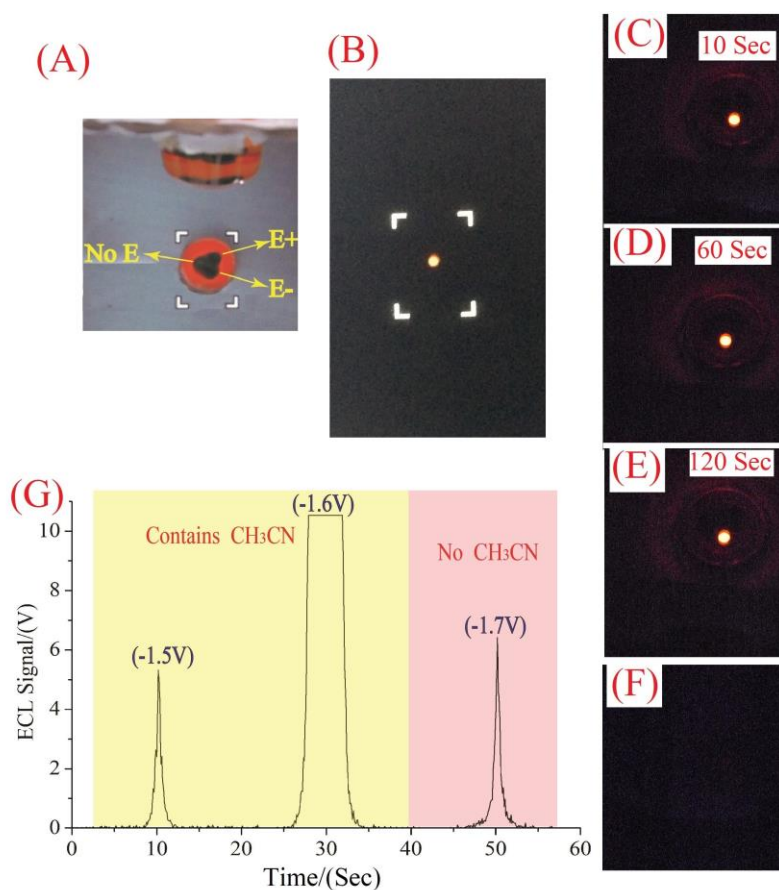


**Figure 4.2** (A)-(F) experimental setup: three GCEs binding together dipping in ECL solution ( $0.5\text{mM } Ru(bpy)_3^{2+}$ ,  $10\text{mM } K_2S_2O_8$ ), one connected positive DC power supply, one connected the negative and the last one connected nothing as comparison for the other two electrodes. (A) and (B) are the camera screenshot of experimental setup before and after measurement; (C)-(E) collected after experiment begins 10 sec, 60 sec and 120 sec under 3.3V applied DC voltage, respectively, in ECL solution contains 35% acetonitrile, while (F) collected under same condition but with ECL solution without acetonitrile; (G) collected using cyclic voltammetry scanned from  $(-0.5)\text{V}$  to  $(-1.5)\text{V}$ ,  $(-1.6)\text{V}$  and  $(-1.7)\text{V}$ , respectively, ECL solution used contains 35% acetonitrile for the first two measurements (yellow area) while the last one does not contain it (pink area), scan rate is  $50\text{mV/s}$ , GCE as working electrode, Ag wire as quasi-reference electrode, Pt grid as counter electrode.

To study the effect of acetonitrile for the emission of cathodic ECL, two kind of ECL solution prepared to use, one contains 35%(v/v) acetonitrile, the other does not, while both are prepared in 0.1M PBS with pH=8. Data of Figure 4.2(C)-(E) are collected in ECL solution contains acetonitrile shows much stronger and more stable ECL emission, while Figure 4.2(F) collected in ECL solution without acetonitrile under same experimental setup and applied voltage can barely to be observed. Same conclusion can be achieved from Figure 4.2(G), which collected using cyclic voltammetry, that the ECL emission can be initiated at much lower potential and much stronger light signal in ECL solution contains acetonitrile compared with that collected in ECL solution without it. All these results are consistent with previous research<sup>46</sup> that  $Ru(bpy)_3^+$  is very unstable in aqueous solutions and adding organic solvent such as acetonitrile could stabilize and increase the ECL emission.

#### 4.3.2 Oxygen Effect for Cathodic ECL

As for studying the effect of oxygen on the emission of cathodic ECL, ECL intensity signals, which are collected with ECL solution bubbled/ not bubbled nitrogen using chronoamperometry at different applied potential (-1.45V, -1.5V and -1.55V vs Ag wire quasi-reference electrode), compared. As Figure 4.3(A)-(C) shows, ECL intensity that performed in ECL solution without bubbling nitrogen is stronger than that from solution degassed nitrogen. The reasons for this are the cathodic ECL emission are not just from a series of reactions between  $Ru(bpy)_3^{2+}$  and persulfate, as mentioned above from Eqs.4-9; some types of reactive oxygen species such as  $H_2O_2$ ,  $\bullet OH$  and  $O_2^{\bullet -}$  could be produced when the dissolved oxygen was reduced under the reduction potential,  $H_2O_2$  can react with  $O_2^{\bullet -}$  to generate  $\bullet OH$ , which can oxidize  $Ru(bpy)_3^{2+}$  to form  $Ru(bpy)_3^{3+}$ , and  $Ru(bpy)_3^{3+}$  can react with  $OH^-$  to generate more  $Ru(bpy)_3^{2+*}$ , therefore, much more intense ECL light could be emitted.<sup>47-48</sup>

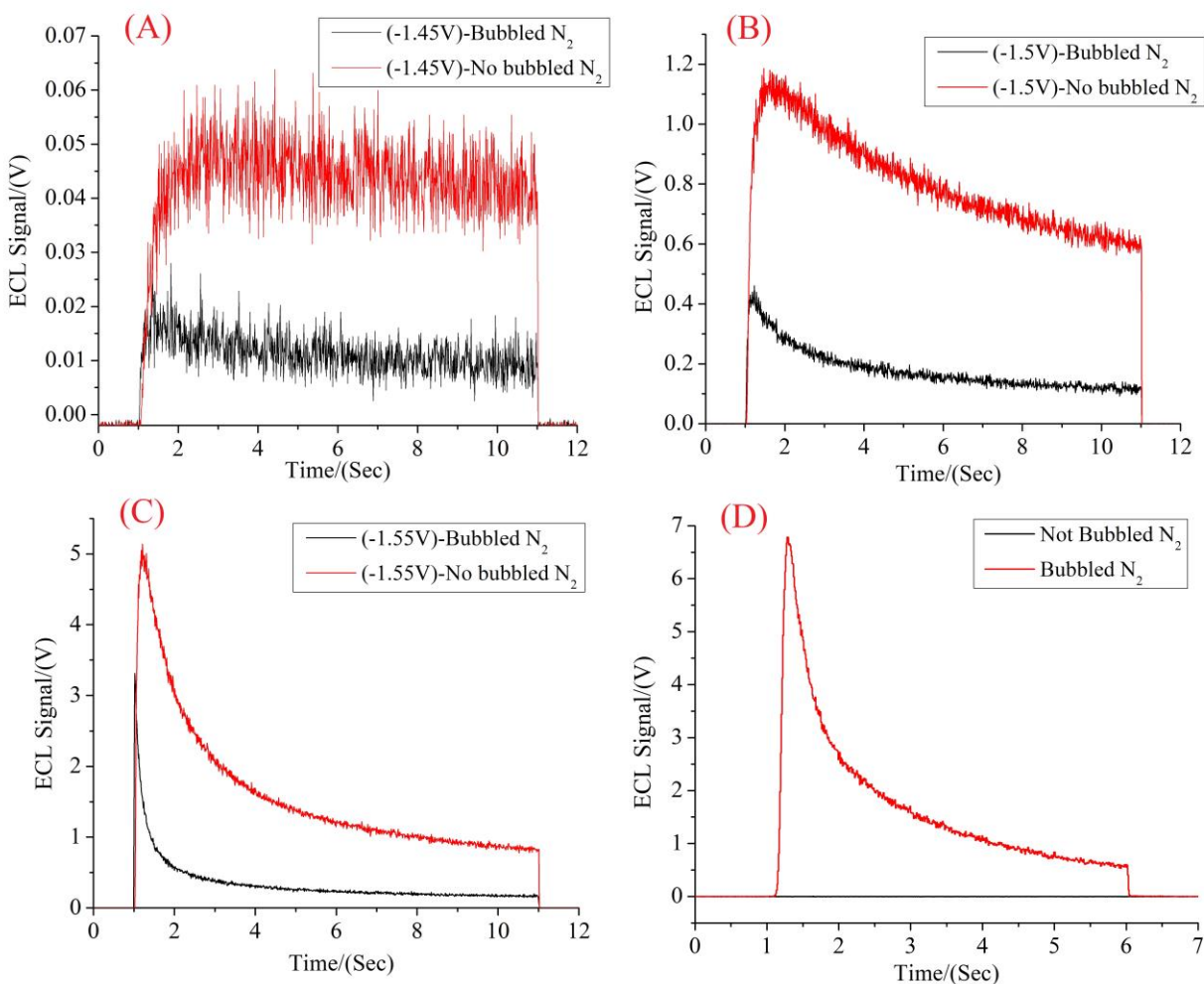


**Figure 4.3** (A)-(C) collected using chronoamperometry at different potential for 10 sec in ECL solution ( $0.25\text{mM } Ru(bpy)_3^{2+}$ ,  $0.5\text{mM } K_2S_2O_8$  in  $0.1\text{M}$  PBS buffer contains 35% acetonitrile,  $\text{pH}=8$ ) with/without bubbling  $N_2$ , GCE as working electrode, Ag wire as quasi-reference electrode, Pt grid as counter electrode. (D) collected C-ECL-C-BPE glucose biosensor used commercial glucose blood test strip measured  $12\text{ mM}$  glucose with ECL solution ( $62.5\mu\text{M } Ru(bpy)_3^{2+}$ ,  $0.125\text{mM } K_2S_2O_8$ ) with/without bubbling  $N_2$  in the reporting cell under  $3.6\text{V}$  applied DC voltage with 5 sec for each measurement.

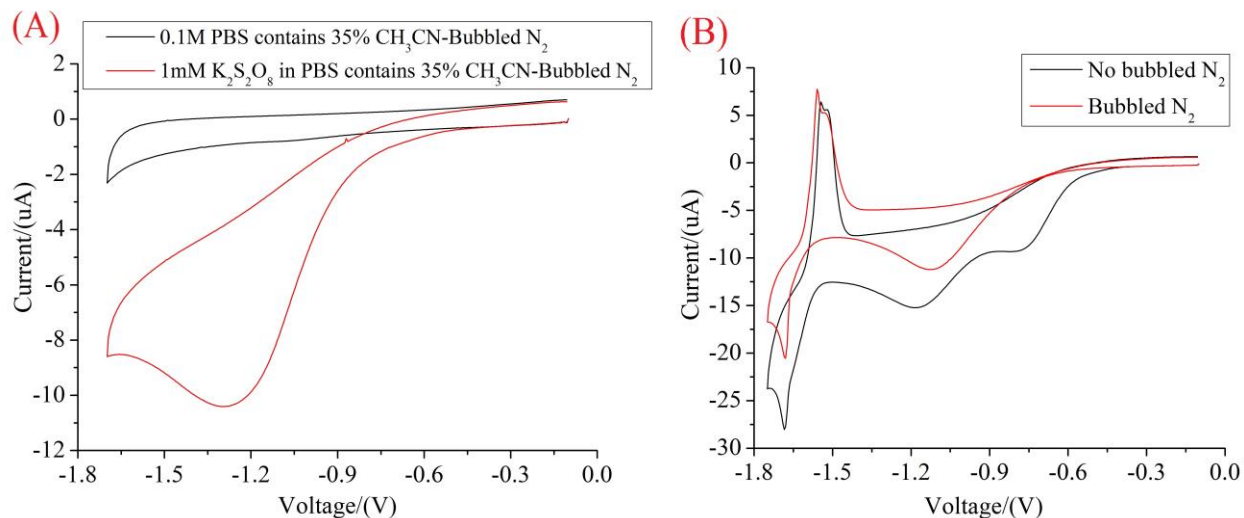


**Figure 4.14** Cyclic voltammograms of GCE, (A) scanned in 0.1M PBS buffer (contains 35% acetonitrile) bubbled  $N_2$  and 1mM  $K_2S_2O_8$  in 0.1M PBS buffer (contains 35% acetonitrile) bubbled  $N_2$ ; (B) scanned in ECL solution (0.5mM  $Ru(bpy)_3^{2+}$ , 1mM  $K_2S_2O_8$ ) with/without bubbling  $N_2$ . Scan rate is 30mV/s, Ag wire as quasi-reference electrode, Pt grid as counter electrode.

However, involving with oxygen into ECL solution used for cathodic ECL glucose biosensor in a closed BPE system is not a good choice, since the concentration of dissolved oxygen is not low (ca. 8-9 mg/L in water at room temperature and 1 atm)<sup>49</sup>, cathodic current from the reduction of oxygen can compensate for the anodic current from BPE and result in only small part of current or no current coming from the reduction of  $Ru(bpy)_3^{2+}$  and persulfate, the standard reduction potentials of  $Ru(bpy)_3^{2+}$  and persulfate are lower than that of oxygen, as indicated in Figure 4.4, the reduction peak potential for oxygen is ca. (-0.8)V while ca. (-1.2)V for persulfate and (-1.7)V for  $Ru(bpy)_3^{2+}$  versus Ag wire quasi-reference electrode, which used to generate the cathodic ECL emission on the cathode of BPE for the reporting of detection signal, in other way, it may result in a failure of detection of a sensor. For example, in the cathodic ECL glucose biosensor in a closed BPE system, the ECL signal is much stronger when the ECL solution bubbled nitrogen,

as shown in Figure 4.3(D) when the sensor performed in 12 mM glucose solution, while the ECL signal almost a flat line ( Figure 4.3(D) black line) detected by the PMT using ECL solution without bubbling nitrogen under the same applied DC voltage.

#### 4.3.3 Electrochemical study of modified GCEs

To study the electrochemical performance of modified GCEs in the glucose solution, two kinds of modified GCEs were scanned in glucose solution using cyclic voltammetry, one is GCEs/GO<sub>x</sub>/GA/Nafion electrode, the other is GCEs/GO<sub>x</sub>/GA/MWCNTs/Nafion. When increase the glucose concentration, it would increase the reaction rate of GO(FAD) reduced to GO(FADH<sub>2</sub>), which will be oxidized back to GO(FAD) by the oxidized form of mediator (hydroquinone) that oxidized on the surface of the modified GCEs, thus a higher current would be generated. As Figure 4.5 indicates, a clear observation of current increasing as modified GCEs scan from 0 to 50 mM concentrated glucose solution, as expected. However, the stability and reproducibility of modified GCEs are not good, as Figure 4.5(B)-(C) shows, no matter GCEs/GO<sub>x</sub>/GA/Nafion electrode or GCEs/GO<sub>x</sub>/GA/MWCNTs/Nafion electrode, a huge net current (the oxidation peak current of CV in certain concentrated glucose solution subtracts that with no glucose in it) differences generated from three sets of measurements with individual modified GCE. We believe the reasons for this may come from two ways, one is the thickness of casted nafion films are different, the other is the interference of GO<sub>x</sub> and GA when casting nafion film since the nafion solution contains water (15-20%) and alcohol (ca. 80%), which could re-dissolve GO<sub>x</sub> and GA during the modification of GCE process. All of this note that using modified GCE as BPE anode is not a good choice to design C-ECL-C-BPE glucose biosensor, unless the stability of Nafion film achieved.



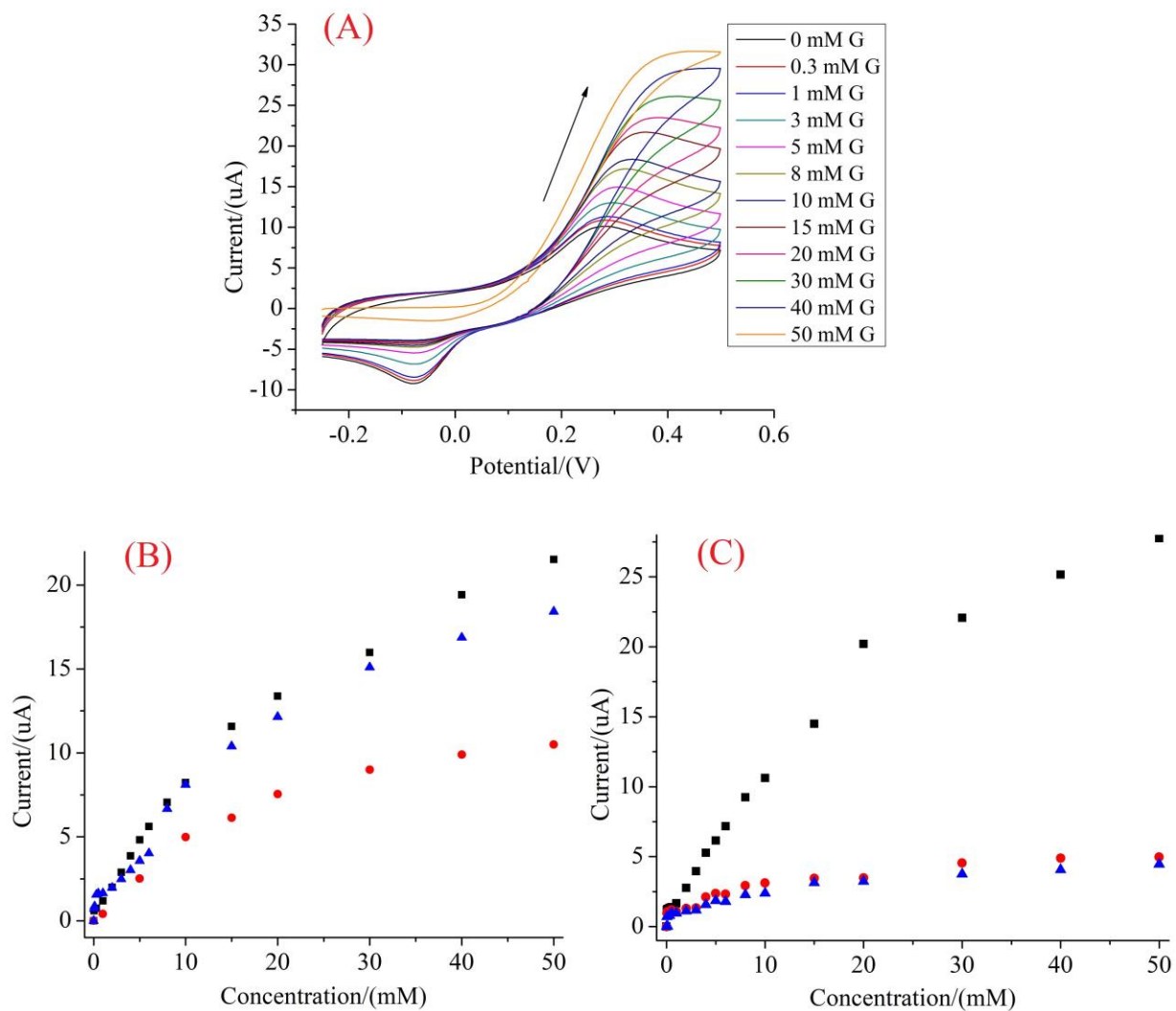


**Figure 4.5** (A) Cyclic voltammograms of modified GCEs/GO<sub>x</sub>/GA/Nafion electrode scanned in different concentrated glucose solution contains 1mM hydroquinone, Ag/AgCl as reference electrode, and Pt grid as counter electrode, scan rate 20 mV/s; (B) the calibration curves of cyclic voltammograms from GCEs/GO<sub>x</sub>/GA/Nafion electrode, each color curve represent from one individual modified GCEs/GO<sub>x</sub>/GA/Nafion electrode measurement;(C) same as (B) except the electrode modified with GCEs/GO<sub>x</sub>/GA/MWCNTs/Nafion.

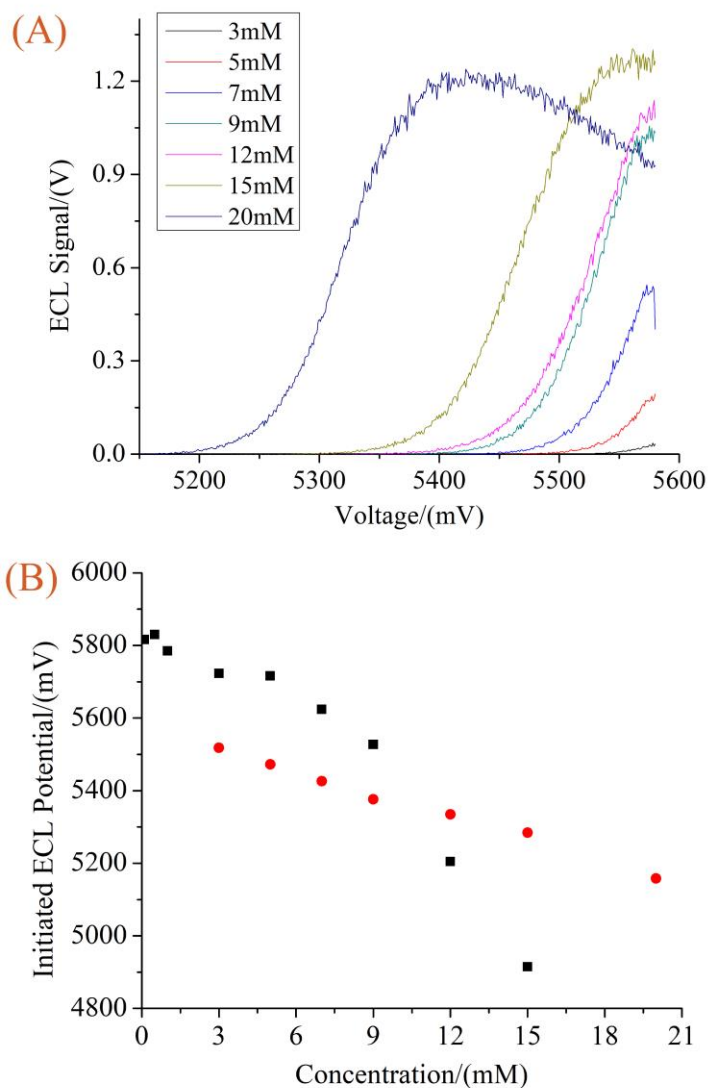


**Figure 4.6** (A) ECL intensity curves from C-ECL-C-BPE method using GCEs/ $\text{GO}_x$ /GA/Nafion electrode as BPE anode as the applied voltage employed from 4500mV to 5580mV; (B) Initiated ECL voltage from two sets of ECL intensity curves employed C-ECL-C-BPE method using GCEs/ $\text{GO}_x$ /GA/Nafion electrode as BPE anode.

To verify the feasibility of C-ECL-C-BPE glucose biosensor method, the modified GCEs/ $\text{GO}_x$ /GA/Nafion electrode used as BPE anode, which were bound with another bare GCE that serves as driving cathode in the sensing cell. The applied voltage scanned from low to high (4500mV to 5680mV) with 10mV/s to find out the voltage that could generate ECL signal at

different concentrated glucose solution. As Figure 4.6(A) demonstrated, the voltage to initiate ECL light decreasing as increasing glucose concentration from 3mM to 20mM. Similar trends could be observed in Figure 4.6(B), where the initiated ECL voltage (defined as the smallest voltage to initiate ECL light) decreasing as increasing glucose concentration. Two color curves represent two individual sets of performance using modified GCEs/GO<sub>x</sub>/GA/Nafion electrode. Even though a big difference of the initiated ECL voltage curves, which caused by instability and irreproducibility of modified BPE anode (GCEs/GO<sub>x</sub>/GA/Nafion electrode) mentioned above, it verified the feasibility and the achievable of the C-ECL-C-BPE glucose biosensor method.

#### 4.3.4 Electrochemical study of commercial blood glucose test strips

Due to the instability and irreproducibility of modified GCEs, commercial blood glucose test strips were used for further study. The test strips are already modified with GO<sub>x</sub> and mediator. As illustrated in Figure 4.7, four connections are showing on the test strips, L1 connected to the center of sensing spot that cover with GO<sub>x</sub> and mediator has a very high probability serves as BPE anode; L3 has a high chance serves as reference electrode that designed to use with commercial glucose meter showed in Figure 4.7(A). Either L2 or L4 serves driving cathode in the sensing cell of closed BPE system. In this small section, L2 was chosen serves as driving cathode to study the C-ECL-C-BPE glucose biosensor.

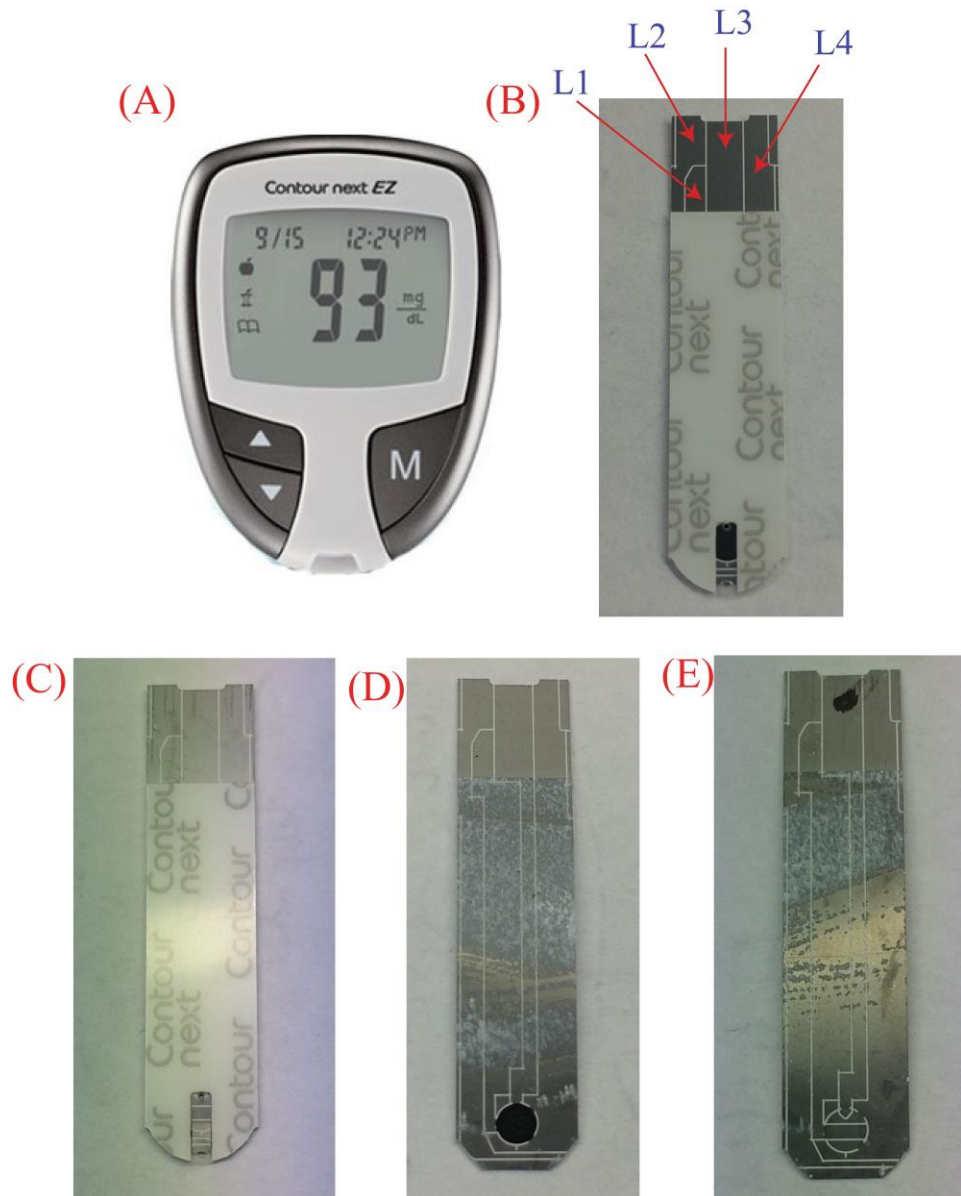


**Figure 4.7** (A) Commercial contour next EZ blood glucose meter; (B) and (C) are un-used glucose test strip and used one, respectively; (D) is inside structure of un-used test strips, and (E) is the used one. Note that the white line on the test strip is insulating.

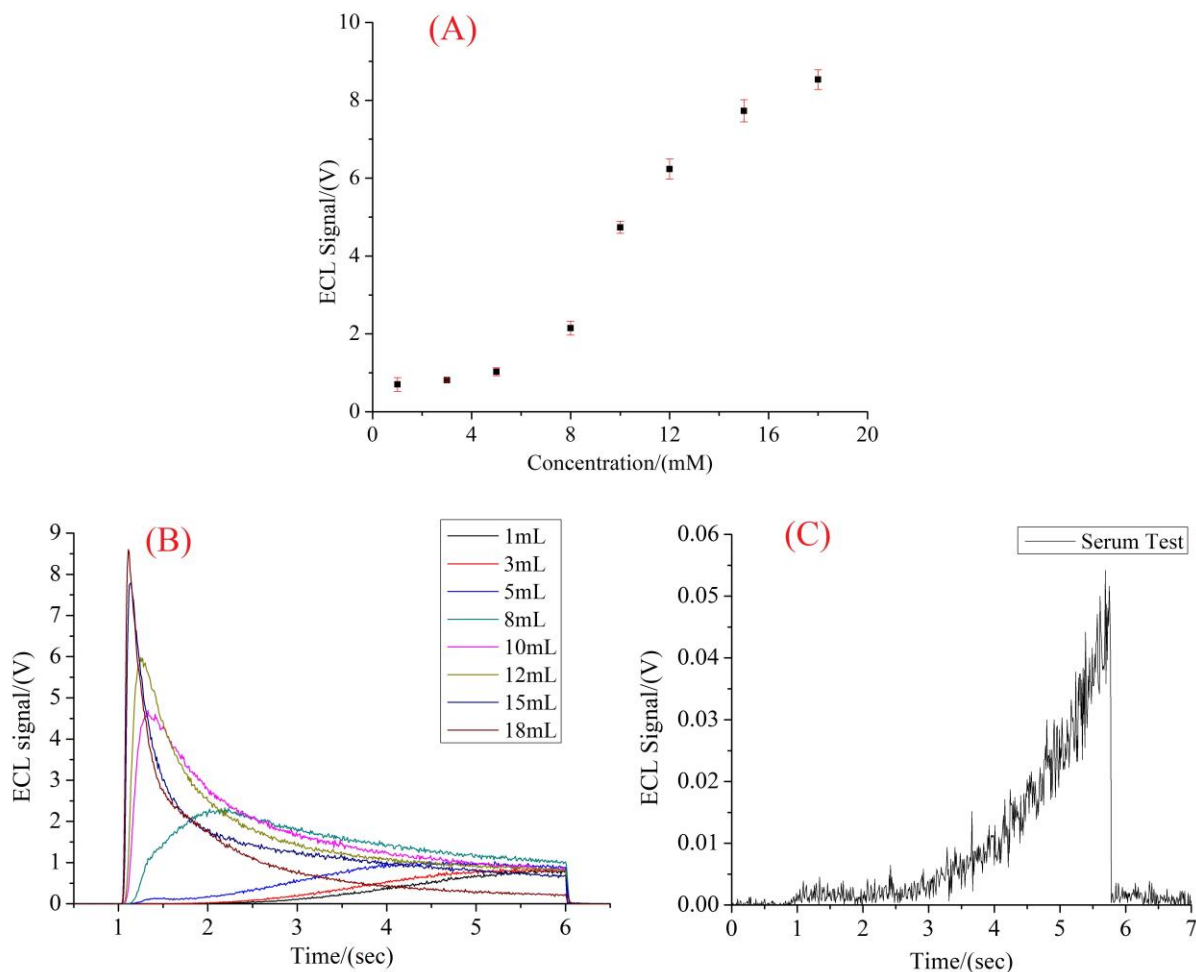


**Figure 4.8** (A) ECL signal calibration curve as a function of glucose concentration, L1 is BPE anode, and L2 as driving cathode, ECL solution ( $62.5\mu\text{M Ru}(bpy)_3^{2+}$ ,  $0.125\text{mM K}_2\text{S}_2\text{O}_8$ ), applied voltage  $4800\text{mV}$ ; (B) is ECL intensity spectra corresponding to (A); (C) is ECL intensity spectrum scanned in serum sample.

A reasonable ECL signal calibration curve as a function of glucose concentration (prepared in  $0.1\text{M}$  PBS buffer with  $\text{pH}=7$ ) employing C-ECL-C-BPE method achieved, as illustrated in Figure 4.8(A), the ECL solution contains  $62.5\mu\text{M Ru}(bpy)_3^{2+}$  and  $0.125\text{mM K}_2\text{S}_2\text{O}_8$ , and a voltage of  $4800\text{mV}$  applied to the glucose biosensor. Then a serum sample was used to test the performance of C-ECL-C-BPE glucose biosensor in human blood sample, as showed in Figure

4.8(C), the ECL intensity signal of light spectrum is very low (ca. 0.045V), out of detection range from the calibration curve showed in Figure 4.8(A) (0.7 V for 1mM glucose), while a 4.5mM glucose acquired using the commercial blood glucose meter. The reason to cause the inconsistent measurement between C-ECL-C-BPE glucose biosensor and commercial glucose meter, is probably two different aqueous system, the former is 0.1M PBS buffer, the latter one is human blood, the resistance of former is smaller than latter, which cause a decreasing current when measuring the blood sample. One way to avoid the big resistance change between BPE anode and driving cathode is short the distance.

Therefore, L4 was chosen for further study of C-ECL-C-BPE glucose biosensor. Note that, without further notification, L4 always serves as the BPE anode when using test strips in C-ECL-C-BPE glucose system.

#### 4.3.5 Performance of the Proposed Cathodic ECL Glucose biosensor in Closed BPE System

Two GCEs (3mm diameter) were bound together used in the reporting cell, and commercial blood glucose test strips that already modified  $GO_x$  and mediator were used in the sensing cell for the proposed C-ECL-C-BPE glucose biosensor. For the rest research, L4 serves driving cathode in the C-ECL-C-BPE glucose system. And the ratio of 2:1 was chosen for the persulfate co-reagent with  $Ru(bpy)_3^{2+}$  luminophore to prepared ECL solution. The volume of ECL solution used ca. 3mL in a small glass vial as the reporting cell for each measurement. To decrease the error difference of each measurement, two GCEs used in the reporting cell were rinsed with D.I. water and dried with nitrogen each time on the successively measurements, and the 3mL ECL solution changed to new one. Since the measuring range of light intensity by the PMT is from 0 to 10.5V, and the lowest glucose concentration for the commercial glucose meter (contains the test strip) can

determine is 1mM, the voltage used to apply on the proposed C-ECL-C-BPE glucose biosensor determined by adjusting the PMT light signal around 1V measuring 1mM glucose solution.

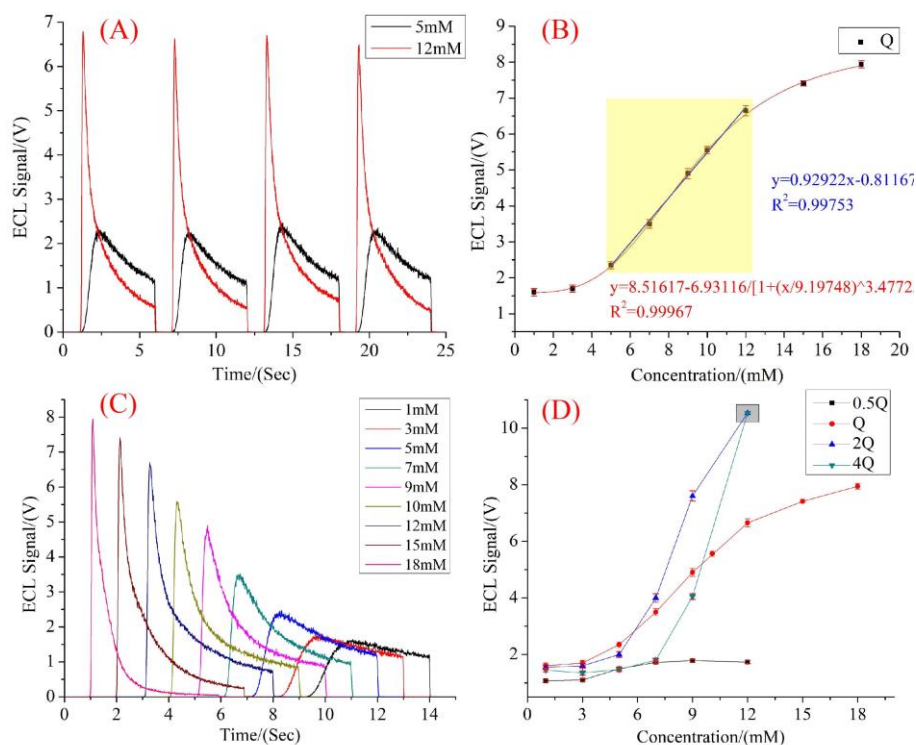


**Figure 4.9** (A) collected four individual cathodic ECL intensity measurement of 5mM and 12 mM glucose in closed BPE system, commercial glucose blood test strip used to measure in the sensing cell and two GCEs in the reporting cell with  $Q = (62.5\mu\text{M } Ru(bpy)_3^{2+}, 0.125\text{mM } K_2S_2O_8)$  ECL solution; (B) is the ECL intensity (V) calibration curve of glucose measurement using C-ECL-C-BPE glucose biosensor method with Q concentrated ECL solution as function of concentration; red line is the logistic fit of the data, blue line in the yellow area is the linear fitting of the data; (C) is the ECL intensity signals corresponding to calibration curve of (B); (D) is the calibration curves of ECL intensity at different concentration as function of glucose concentration using C-ECL-C-BPE glucose biosensor method. All the measurements obtained under 3.6V applied DC voltage and 5 sec except for 4Q curve achieved under 3635mV, each data point measured at least three times.

To investigate the reproducibility and stability of proposed C-ECL-C-BPE glucose biosensor, four individual measurements were performed in 5mM and 12mM glucose solution with Q=(62.5uM  $Ru(bpy)_3^{2+}$ , 0.125mM  $K_2S_2O_8$ ) ECL solution under 3.6V applied voltage from the DC power supply that determined from above mentioned method, as demonstrated in Figure 4.9(A), the ECL signal is ca. 2.3V in 5mM glucose solution and ca. 6.7V in 12 mM, and consistent with each measurement, which shows great reproducibility and stability for the proposed glucose biosensor. Thus, the ECL intensity calibration curve as a function of glucose concentration was collected by using Q concentrated ECL solution, each data point on the calibration curve measured at least three times with 5 sec for each measurement, as illustrated in Figure 4.9(B)-(C), the ECL intensity gradually increases as glucose concentration varied from 1mM to 18mM, and shows a linear relationship with the glucose concentration in the range of 5mM to 12mM ( $R^2=0.998$ ), which shown in the yellow area of Figure 4.9(B), and the red curve is the logistic fitting of collected data ( $R^2=0.999$ ). The limit of detection (defined as the concentration of glucose generating ECL signal three times higher than the standard deviation when it subtracts that of 1mM, which was treated as blank sample since it is the lowest concentration of glucose for the commercial test strip with the blood glucose meter can be measured) was calculated from the red fitting curve to be 3.8mM, and the sensitivity (defined as the smallest glucose concentration change that generating ECL signal higher than the standard deviation of blank sample) of proposed glucose biosensor using Q concentrated ECL solution is ca. 0.2mM.



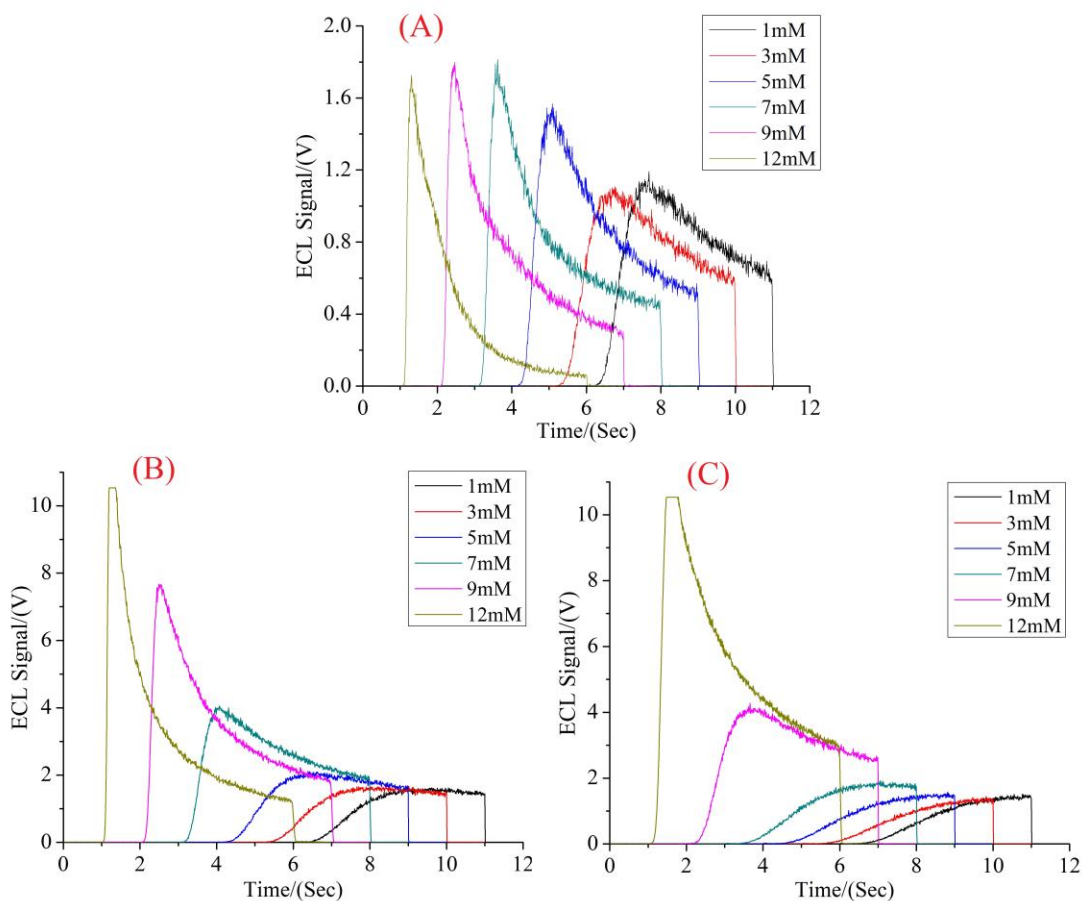


**Figure 4.10** (A) and (C) are ECL Signal intensity curves as function of measuring glucose concentration using different concentrated ECL solution, each data point measured at least three times; (B) and (D) are the ECL signal responses at different glucose concentration corresponding (A) and (C), respectively. Two GCEs used in the sensing cell under 4.6V applied voltage and 5 sec for each measurement.

To better understand the mechanism of proposed C-ECL-C-BPE glucose biosensor, different ECL intensity calibration curves were collected as a function of glucose concentration using different concentrated ECL solution (0.5Q, 2Q and 4Q), as indicated in Figure 4.9(D) (as for the corresponding ECL intensity spectra curves see Figure 4.10), the ECL intensity increases as glucose concentration varies from low to high, as expected, higher concentration of glucose would

produce higher current on anode of BPE, and higher cathodic current generated from reduction of  $Ru(bpy)_3^{2+}$  and persulfate on cathode of BPE was needed to compensate for it since current going through anode and cathode of BPE is same, which would obtain more  $Ru(bpy)_3^+$  and  $SO_4^{\bullet-}$  and result in stronger emission of ECL light, as mentioned above for the mechanism explanation of proposed C-ECL-C-BPE glucose biosensor in Figure 4.1. In terms of the black calibration curve of 0.5Q in Figure 4.9(D), the ECL intensity signal is low compared with that of red curve of Q at the same glucose concentration, even at higher concentration such as 12mM, the ECL intensity signal increased less than 1V compared with that of its blank point (mentioned above, defined as 1mM glucose concentration), we believe that is due to the concentration of  $Ru(bpy)_3^{2+}$  and persulfate used in the ECL solution too low, the limit amount of  $Ru(bpy)_3^{2+*}$  that could be generated, even though with increasing concentration of glucose. On the other hand, under the same applied potential, the ECL signal of blue calibration curve of 2Q increased sharply starts from 5mM, and reaches the measuring threshold of PMT at 12mM glucose, as the gray area showed in Figure 4.9(D), compared to that of red calibration curve of Q. This is probably owing to the cathodic current of BPE used to compensate for the increasing anodic current caused by the increased glucose concentration all contributes to reducing more  $Ru(bpy)_3^{2+}$  and persulfate and generating more  $Ru(bpy)_3^{2+*}$ , which results in a sharp increasing of ECL intensity. Furthermore, a small phenomenon should be noticed that the lowest detection limit of the calibration curve is gradually increasing as the ECL concentration varied from Q to 2Q, and it becomes much more obvious when ECL concentration changed into 4Q, the detection limit of the calibration curve of 4Q is ca. 7mM, even though the applied voltage for the calibration curve of 4Q is increased into 3635mV instead of 3600mV that used for other three ECL intensity calibration curves. This is due to as increasing the ECL concentration, the concentration of persulfate also increases since we kept

a constant ratio of concentration for  $Ru(bpy)_3^{2+}$  and persulfate in the ECL solution, plus the reduction of persulfate is much easier than that of  $Ru(bpy)_3^{2+}$ , as illustrated in Figure 4.4, the reduction peak potential of persulfate is ca. (-1.2)V while for  $Ru(bpy)_3^{2+}$  is ca. (-1.7)V versus Ag wire quasi-reference electrode, most of increased current caused by increasing glucose concentration in the sensing cell could be compensate by the reduction of persulfate, in that case, only small amount of  $Ru(bpy)_3^{2+}$  can be reduced to  $Ru(bpy)_3^+$  that used to react with  $SO_4^{\bullet-}$  or  $Ru(bpy)_3^{3+}$  to generate ECL light, which would indirectly lower the ECL intensity signal. This has the same effect as the oxygen mentioned above for the generation of ECL signal when the concentration of persulfate too high. In brief, it is easy to conclude that the sensitivity of proposed glucose biosensor would increase, and detection range of glucose concentration would decrease as increasing the ECL concentration.

To verify the proposed the mechanism of C-ECL-C-BPE sensor, in which the commercial test strip replaced with two GCEs, potassium ferrocyanide solution that prepared in 0.1M PBS with pH=7 were used to measure in the sensing cell. As demonstrated in Figure 4.11, two ECL intensity calibration curves were collected by performing in Q and 4Q concentrated ECL solutions under 4.6V applied DC voltage for 5 sec of each measurement, and the ECL intensity signal changes not large (ca. 3V difference) in calibration curve of Q as the concentration of ferrocyanide varied from 1mM to 7mM, as for the ECL intensity calibration curve of 4Q, the ECL signal difference changes over 7V. The trend of ECL signal calibration curves is similar with that used for the glucose measurement mentioned above when changing the ECL concentration, as expected.

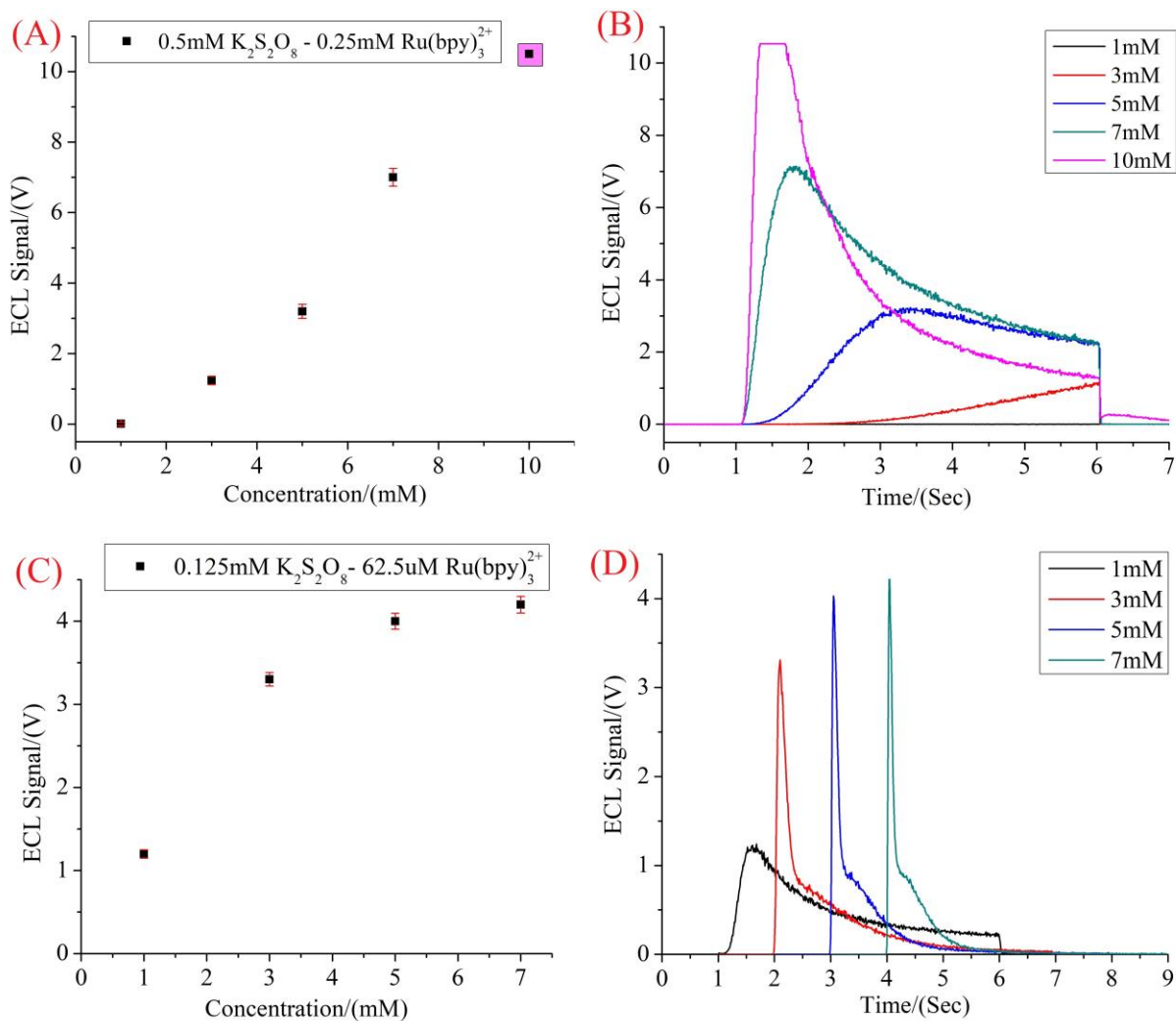


**Figure 4.11** (A), (B) and (C) are ECL signal intensity (V) responses at different glucose concentrations using C-ECL-C-BPE glucose biosensor method with 0.5Q, 2Q and 4Q concentrated ECL solution, respectively.

#### 4.3.6 Glucose Detection of Human Serum

Once we understand the operational mechanism of proposed C-ECL-C-BPE glucose biosensor, real clinical samples were used to determine the glucose concentration by employing the proposed glucose biosensor, crucially, to evaluate the reliability and application potential of this method, commercial blood glucose meter used as a comparison. Therefore, eight human serum samples, three from normal donors, the rest of five from the diabetes donors (including one from

diabetes type I) (more detailed information see Table 4.1) measured using these two methods. Noted that, every sample measured at least three times using each method. The similarity of the results between the proposed C-ECL-C-BPE glucose biosensor and commercial blood glucose meter shown in Figure 4.11. And the glucose concentration determined using proposed method through the logistic fitting function (red function) shown in Figure 4.9(B). Since glucose concentration, prepared in 0.1M PBS with pH=7, determined ca. 20% higher than the real value by using the commercial blood glucose meter, which probably caused by two measuring glucose solution system, one is prepared in 0.1M PBS, the other is in human serum. Thus, we corrected our results that used to determine glucose in serum by employing our proposed method by  $\times 120\%$ , as illustrated of the blue plotted data in Figure 4.12. More detailed data see Table 4.2. The results using both methods show great similarity, therefore, it is easy to conclude that the proposed C-ECL-C-BPE sensor has great potential as a reliable technique for determination of glucose in practical applications.

**Table 4.1** Information of Human Serum Samples.

<u>Serum #</u>	<u>Gender</u>	<u>Age/years</u>	<u>Race</u>	<u>Ethnicity</u>	<u>Diagnosis</u>	<u>Medications</u>
1	Female	24	Caucasian	Hispanic	Normal Donor	None
2	Male	50	Caucasian	N/A	Normal Donor	None
3	Female	38	African	African American	Normal Donor	None
4	Male	81	Caucasian	N/A	Diabetes Type 1	Metformin, Janumet
5	Male	21	Caucasian	Slavic	Diabetes Type 1	Novorapid 1.1iu-6.6iu, Lantus 2.22iu Glimepiride 4mg, Metoprolol 50mg, Plavix 75mg, Crestor 20mg, Iron, Vitamin D 3000, Timolol 0.5
6	Male	61	N/A	Hispanic	Diabetes Type 2	Metformin 1000mg, Losartan 21mg, Glipizide 5mg, Citalopram 10mg, Folic Acid 800mcg
7	Female	70	N/A	Hispanic	Diabetes, Depression Normal Donor, Type	Metformin 1000mg, Losartan 21mg, Glipizide 5mg, Citalopram 10mg, Folic Acid 800mcg
8	Male	59	Caucasian	N/A	2 Diabetes, Hypertension (HTN)	Lisinopril 10mg, Jardiance

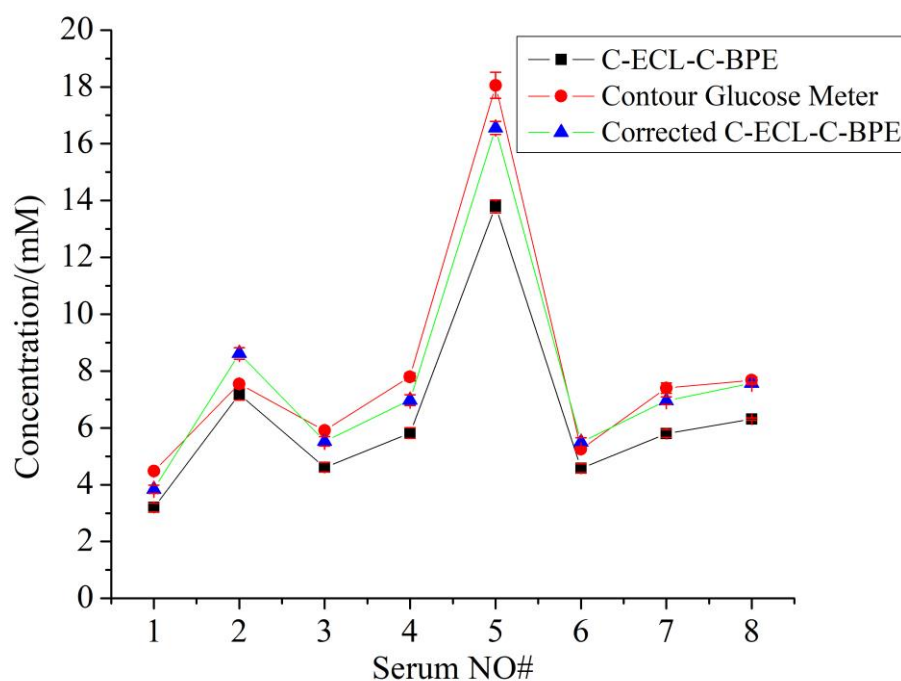


**Figure 4.12** Comparison of methods for determining glucose concentrations in human serum samples. Black data measured using proposed C-ECL-C-BPE method; blue data is the correction of black data; red data measured using commercial Contour NEXT EZ blood Glucose Meter. Each data point measured at least three times.

**Table 4.2** Comparison between C-ECL-C-BPE method with Contour NEXT EZ Blood Glucose Meter for glucose measurement.

Human Serum #	BPE-ECL		Corrected BPE-ECL		Contour NEXT EZ Blood Glucose Meter	
	Concentration/mM	Std/mM	Concentration/mM	Std/mM	Concentration/mM	Std/mM
NO.1	3.2	0.15	3.84	0.18	4.478	0.052
NO.2	7.186	0.205	8.62	0.247	7.549	0.056
NO.3	4.609	0.169	5.531	0.203	5.912	0.028
NO.4	5.818	0.189	6.982	0.227	7.799	0.139
NO.5	13.796	0.231	16.555	0.277	18.054	0.458
NO.6	4.58	0.155	5.496	0.189	5.255	0.069
NO.7	5.799	0.133	6.959	0.159	7.401	0.183
NO.8	6.311	0.043	7.573	0.052	7.679	0.114

#### 4.4 Conclusions

We have developed a new approach that using cathodic ECL in a closed system to determine the glucose concentration in samples. In this study, the operational mechanism of proposed C-ECL-C-BPE glucose biosensor has been studied; effect of oxygen and acetonitrile in the ECL solution for the generation of ECL signal has been discussed; different ECL concentration used by the proposed sensor for determination of glucose has been explained. To increase the sensitivity or adjust the detection range of interested analytes, many parameters could be optimized or change, such as the ECL solution composition, amplification voltage of PMT, modification of electrode used in the sensing cell (could do in the future), redesign the close BPE cell, etc. On the other hand, C-ECL-C-BPE method is a universal technique for detection of interested analytes. More importantly, easy to fabricate, cheap to use, fast to detect (only need 5 sec or even shorter), great similarity of the results for determination of glucose in human serum samples performed using proposed method and commercial blood glucose meter, showed the C-ECL-C-BPE sensor has a bright prospect as a reliable analytical strategy for detection of drugs, food, environmental monitoring, scientific research and so on.



## References

1. Mathers, C.; Stevens, G.; Mascarenhas, M., *Global health risks: mortality and burden of disease attributable to selected major risks*. World Health Organization: 2009.
2. Cho, N.; Shaw, J.; Karuranga, S.; Huang, Y.; da Rocha Fernandes, J.; Ohlrogge, A.; Malanda, B., IDF Diabetes Atlas: Global estimates of diabetes prevalence for 2017 and projections for 2045. *Diabetes research and clinical practice* **2018**, *138*, 271-281.
3. Heller, A.; Feldman, B., Electrochemical glucose sensors and their applications in diabetes management. *Chemical reviews* **2008**, *108* (7), 2482-2505.
4. Bartlett, P. N.; Tebbutt, P.; Whitaker, R. G., Kinetic aspects of the use of modified electrodes and mediators in bioelectrochemistry. *Progress in reaction kinetics* **1991**, *16* (2), 55-155.
5. Chen, C.; Xie, Q.; Yang, D.; Xiao, H.; Fu, Y.; Tan, Y.; Yao, S., Recent advances in electrochemical glucose biosensors: a review. *Rsc Advances* **2013**, *3* (14), 4473-4491.
6. Clark Jr, L. C.; Lyons, C., Electrode systems for continuous monitoring in cardiovascular surgery. *Annals of the New York Academy of sciences* **1962**, *102* (1), 29-45.
7. Sekretaryova, A. N.; Vokhmyanina, D. V.; Chulanova, T. O.; Karyakina, E. E.; Karyakin, A. A., Reagentless biosensor based on glucose oxidase wired by the mediator freely diffusing in enzyme containing membrane. *Analytical chemistry* **2012**, *84* (3), 1220-1223.
8. Cass, A. E.; Davis, G.; Francis, G. D.; Hill, H. A. O.; Aston, W. J.; Higgins, I. J.; Plotkin, E. V.; Scott, L. D.; Turner, A. P., Ferrocene-mediated enzyme electrode for amperometric determination of glucose. *Analytical chemistry* **1984**, *56* (4), 667-671.
9. Chaubey, A.; Malhotra, B., Mediated biosensors. *Biosensors and bioelectronics* **2002**, *17* (6-7), 441-456.

10. Lupu, A.; Compagnone, D.; Palleschi, G., Screen-printed enzyme electrodes for the detection of marker analytes during winemaking. *Analytica Chimica Acta* **2004**, *513* (1), 67-72.
11. Chen, C.; Wang, L.; Tan, Y.; Qin, C.; Xie, F.; Fu, Y.; Xie, Q.; Chen, J.; Yao, S., High-performance amperometric biosensors and biofuel cell based on chitosan-strengthened cast thin films of chemically synthesized catecholamine polymers with glucose oxidase effectively entrapped. *Biosensors and Bioelectronics* **2011**, *26* (5), 2311-2316.
12. Qin, C.; Chen, C.; Xie, Q.; Wang, L.; He, X.; Huang, Y.; Zhou, Y.; Xie, F.; Yang, D.; Yao, S., Amperometric enzyme electrodes of glucose and lactate based on poly (diallyldimethylammonium)-alginate-metal ion-enzyme biocomposites. *Analytica chimica acta* **2012**, *720*, 49-56.
13. Ghica, M. E.; Brett, C. M., A glucose biosensor using methyl viologen redox mediator on carbon film electrodes. *Analytica Chimica Acta* **2005**, *532* (2), 145-151.
14. Deng, H.; Teo, A. K. L.; Gao, Z., An interference-free glucose biosensor based on a novel low potential redox polymer mediator. *Sensors and Actuators B: Chemical* **2014**, *191*, 522-528.
15. Milton, R. D.; Minteer, S. D., Direct enzymatic bioelectrocatalysis: differentiating between myth and reality. *Journal of the Royal Society Interface* **2017**, *14* (131), 20170253.
16. Xia, H.-q.; Tang, H.; Zhou, B.; Li, Y.; Zhang, X.; Shi, Z.; Deng, L.; Song, R.; Li, L.; Zhang, Z., Mediator-free electron-transfer on patternable hierarchical meso/macro porous bienzyme interface for highly-sensitive sweat glucose and surface electromyography monitoring. *Sensors and Actuators B: Chemical* **2020**, 127962.
17. Liu, J.; He, Z.; Khoo, S. Y.; Tan, T. T. Y., A new strategy for achieving vertically-erected and hierarchical TiO<sub>2</sub> nanosheets array/carbon cloth as a binder-free electrode for protein

impregnation, direct electrochemistry and mediator-free glucose sensing. *Biosensors and Bioelectronics* **2016**, *77*, 942-949.

18. Paul, A.; Vyas, G.; Paul, P.; Srivastava, D. N., Gold-Nanoparticle-Encapsulated ZIF-8 for a Mediator-Free Enzymatic Glucose Sensor by Amperometry. *ACS Applied Nano Materials* **2018**, *1* (7), 3600-3607.

19. Fidal, V.; Inguva, S.; Krishnamurthy, S.; Marsili, E.; Mosnier, J.-P.; Chandra, T., Mediator-free interaction of glucose oxidase, as model enzyme for immobilization, with Al-doped and undoped ZnO thin films laser-deposited on polycarbonate supports. *Enzyme and microbial technology* **2017**, *96*, 67-74.

20. Pu, G.; Yang, Z.; Wu, Y.; Wang, Z.; Deng, Y.; Gao, Y.; Zhang, Z.; Lu, X., Investigation into the Oxygen-Involved Electrochemiluminescence of Porphyrins and Its Regulation by Peripheral Substituents/Central Metals. *Analytical chemistry* **2019**, *91* (3), 2319-2328.

21. Maar, R. R.; Zhang, R.; Stephens, D. G.; Ding, Z.; Gilroy, J. B., Near-Infrared Photoluminescence and Electrochemiluminescence from a Remarkably Simple Boron Difluoride Formazanate Dye. *Angewandte Chemie International Edition* **2019**, *58* (4), 1052-1056.

22. Baek, S.; Kwon, S.-R.; Yeon, S. Y.; Yoon, S.-H.; Kang, C. M.; Han, S. H.; Lee, D.; Chung, T. D., Miniaturized reverse electro dialysis-powered biosensor using electrochemiluminescence on bipolar electrode. *Analytical chemistry* **2018**, *90* (7), 4749-4755.

23. Wang, D.; Liang, Y.; Su, Y.; Shang, Q.; Zhang, C., Sensitivity enhancement of cloth-based closed bipolar electrochemiluminescence glucose sensor via electrode decoration with chitosan/multi-walled carbon nanotubes/graphene quantum dots-gold nanoparticles. *Biosensors and Bioelectronics* **2019**, *130*, 55-64.

24. Hai-Juan, L.; Shuang, H.; Lian-Zhe, H.; Guo-Bao, X., Progress in Ru (bpy) 32+ Electrogenerated Chemiluminescence. *Chinese Journal of Analytical Chemistry* **2009**, *37* (11), 1557-1565.
25. Cui, C.; Jin, R.; Jiang, D.; Zhang, J.; Zhu, J.-J., Electrogenerated Chemiluminescence in Submicrometer Wells for Very High-Density Biosensing. *Analytical Chemistry* **2019**, *92* (1), 578-582.
26. Zhang, J.; Jin, R.; Jiang, D.; Chen, H.-Y., Electrochemiluminescence-based capacitance microscopy for label-free imaging of antigens on the cellular plasma membrane. *Journal of the American Chemical Society* **2019**, *141* (26), 10294-10299.
27. Li, Z.; Qin, W.; Liang, G., A mass-amplifying electrochemiluminescence film (MAEF) for the visual detection of dopamine in aqueous media. *Nanoscale* **2020**.
28. Huang, B.; Liu, X.-P.; Chen, J.-S.; Mao, C.-j.; Niu, H.-L.; Jin, B.-K., Electrochemiluminescence immunoassay for the prostate-specific antigen by using a CdS/chitosan/gC 3 N 4 nanocomposite. *Microchimica Acta* **2020**, *187* (3), 155.
29. Liu, G.; Ma, C.; Jin, B.-K.; Chen, Z.; Cheng, F.-L.; Zhu, J.-J., Electrochemiluminescence investigation of glucose transporter 4 expression at skeletal muscle cells surface based on a graphene hydrogel electrode. *Analytical chemistry* **2019**, *91* (4), 3021-3026.
30. Wang, C.; Chen, L.; Wang, P.; Li, M.; Liu, D., A novel ultrasensitive electrochemiluminescence biosensor for glutathione detection based on poly-l-lysine as co-reactant and graphene-based poly (luminol/aniline) as nanoprobe. *Biosensors and Bioelectronics* **2019**, *133*, 154-159.

31. Zhu, H.-Y.; Ding, S.-N., Dual-signal-amplified electrochemiluminescence biosensor for microRNA detection by coupling cyclic enzyme with CdTe QDs aggregate as luminophor. *Biosensors and Bioelectronics* **2019**, *134*, 109-116.
32. Wu, Q.; Wang, P.; Yang, X.; Wei, M.; Zhou, M.; Pu, Y.; Zhang, M., Fe-Co-Co prussian blue analogues as a novel co-reaction accelerator for ultrasensitive electrochemiluminescent biosensor construction. *Sensors and Actuators B: Chemical* **2019**, *297*, 126767.
33. Qi, Z.; You, S.; Liu, R.; Chuah, C. J., Performance and mechanistic study on electrocoagulation process for municipal wastewater treatment based on horizontal bipolar electrodes. *Frontiers of Environmental Science & Engineering* **2020**, *14* (3), 1-10.
34. Lacina, K.; Kazda, T.; Syrový, T.; Trnková, L.; Vanýsek, P.; Skládal, P., Asymmetric bipolar electrochemistry: Detailed empirical description and determination of output characteristics of a galvanic system with multiple short-circuited cells in one electrolyte. *Electrochimica Acta* **2019**, *307*, 269-274.
35. Shannon, C.; Wang, B.; Yu, S., Reduction of 4-Nitrothiophenol on Ag/Au Bimetallic Alloy Surfaces Studied Using Bipolar Raman Spectroelectrochemistry. *ChemElectroChem* **2020**.
36. Sheridan, E.; Hlushkou, D.; Knust, K. N.; Tallarek, U.; Crooks, R. M., Enrichment of cations via bipolar electrode focusing. *Analytical chemistry* **2012**, *84* (17), 7393-7399.
37. Rafatmah, E.; Hemmateenejad, B., Colorimetric and visual determination of hydrogen peroxide and glucose by applying paper-based closed bipolar electrochemistry. *Microchimica Acta* **2019**, *186* (11), 684.
38. Arora, A.; Eijkel, J. C.; Morf, W. E.; Manz, A., A wireless electrochemiluminescence detector applied to direct and indirect detection for electrophoresis on a microfabricated glass device. *Analytical chemistry* **2001**, *73* (14), 3282-3288.

39. Wu, M.-S.; Liu, Z.; Shi, H.-W.; Chen, H.-Y.; Xu, J.-J., Visual electrochemiluminescence detection of cancer biomarkers on a closed bipolar electrode array chip. *Analytical chemistry* **2015**, *87* (1), 530-537.
40. Yu, X.; Liang, J.; Yang, T.; Gong, M.; Xi, D.; Liu, H., A resettable and reprogrammable keypad lock based on electrochromic Prussian blue films and biocatalysis of immobilized glucose oxidase in a bipolar electrode system. *Biosensors and Bioelectronics* **2018**, *99*, 163-169.
41. Wang, Y.; Jin, R.; Sojic, N.; Jiang, D.; Chen, H.-Y., Intracellular Wireless Analysis of Single Cells by Bipolar Electrochemiluminescence Confined in Nanopipette. *Angewandte Chemie International Edition* **2020**.
42. Feng, Q.-M.; Pan, J.-B.; Zhang, H.-R.; Xu, J.-J.; Chen, H.-Y., Disposable paper-based bipolar electrode for sensitive electrochemiluminescence detection of a cancer biomarker. *Chemical Communications* **2014**, *50* (75), 10949-10951.
43. Tian, Y.; Han, S.; Hu, L.; Yuan, Y.; Wang, J.; Xu, G., Cathodic electrochemiluminescence and reversible electrochemistry of [Ru (bpy) <sub>3</sub>] <sup>2+/1+</sup> in aqueous solutions on tricresyl phosphate-based carbon paste electrode with extremely high hydrogen evolution potential. *Analytical and bioanalytical chemistry* **2013**, *405* (11), 3427-3430.
44. Ege, D.; Becker, W. G.; Bard, A. J., Electrogenerated chemiluminescent determination of tris (2, 2'-bipyridine) ruthenium ion (Ru(bpy)<sub>3</sub><sup>2+</sup>) at low levels. *Analytical chemistry* **1984**, *56* (13), 2413-2417.
45. Ala-Kleme, T.; Kulmala, S.; Väre, L.; Juhala, P.; Helin, M., Hot electron-induced electrogenerated chemiluminescence of Ru (bpy) <sub>3</sub> <sup>2+</sup> chelate at oxide-covered aluminum electrodes. *Analytical Chemistry* **1999**, *71* (24), 5538-5543.

46. White, H. S.; Bard, A. J., Electrogenerated chemiluminescence. 41. Electrogenerated chemiluminescence and chemiluminescence of the Ru (2, 21-bpy)  $32+$ -S<sub>2</sub>O<sub>8</sub><sup>2-</sup>-system in acetonitrile-water solutions. *Journal of the American Chemical Society* **1982**, *104* (25), 6891-6895.
47. Cao, W.; Xu, G.; Zhang, Z.; Dong, S., Novel tris (2, 2'-bipyridine) ruthenium (ii) cathodic electrochemiluminescence in aqueous solution at a glassy carbon electrode. *Chemical communications* **2002**, (14), 1540-1541.
48. Clark, C. D.; Debad, J. D.; Yonemoto, E. H.; Mallouk, T. E.; Bard, A. J., Effect of Oxygen on Linked Ru (bpy)  $32+$ - Viologen Species and Methylviologen: A Reinterpretation of the Electrogenerated Chemiluminescence. *Journal of the American Chemical Society* **1997**, *119* (43), 10525-10531.
49. Truesdale, G. A.; Downing, A.; Lowden, G., The solubility of oxygen in pure water and sea-water. *Journal of Applied Chemistry* **1955**, *5* (2), 53-62.

## Chapter 5

### Conclusions and Future Directions

In terms of dissertation work, which used bipolar electrochemistry as a basic platform, we have successfully illustrated reduction of 4-NTP on Ag/Au bimetallic alloy surfaces using bipolar Raman spectroelectrochemistry, refinements of cell frames for BPE system, and cathodic ECL glucose biosensor using closed BPE system. The conclusions and future direction showed as below.

#### **5.1 Reduction of 4-NTP on Ag/Au Bimetallic Alloy Surfaces using Bipolar Raman Spectroelectrochemistry**

Herein, we describe an experimental approach for adapting the principles of Raman spectroelectrochemistry to electrodes controlled using a bipolar circuit. This method allows the simultaneous acquisition of spectroscopic data as a function of both the electrode potential and the chemical composition of a bimetallic alloy and can be generalized to other system variables. The electrochemical reduction of 4-nitrothiophenol (4-NTP) was carried out on bimetallic Ag/Au alloy gradients and monitored in situ using a confocal Raman microscope with 785 nm excitation. 2D Raman profiles as a function of potential and bimetallic alloy composition were collected serially across the BPE in a raster pattern. Continuous Ag/Au alloy gradients, in which the alloy composition varied from approximately 0.5 to 1.0 mole fraction Ag, were prepared by using bipolar electrodeposition and then modified with a monolayer of 4-NTP using self-assembly. The steady state surface concentrations of 4-NTP, 4-ATP, and DMAB (4,4'-dimercaptoazobenzene) on Au/Ag alloys were placed in a bipolar electrochemical cell and characterized as a function of applied potential and chemical composition by using surface-enhanced Raman scattering. The  $E_{1/2}$  for NTP reduction was observed to be a strong function of the alloy composition, increasing by over 100 mV as the mole fraction of Ag varied from 0.5 to 1.0. In addition, spectroscopic evidence



for the formation of the partially reduced intermediate, DMAB at intermediate applied potentials, was also found. The experimental strategy described herein can be generalized to gain access to a variety of 2D data sets for arrange of interesting electrochemical systems. Bipolar Raman spectroelectrochemistry (BRSE) is a valuable tool for the characterization of solid-state material libraries that should aid in the discovery of new electrocatalysts.

Future directions, bimetallic materials could be changed, such as Au/Ag/Pt/Pd/Cd, etc., and replacement of interested molecules used to study as well.

## **5.2 Potential Profile of BPE using Different Cell Frames Design**

In this work, the potential profiles from open cell frame, closed cell frame, and channel cell frame were studied. Also, four models from channel cell frames were offered to describe and explain the channel potential based on the variables of normalized channel length and width. Most importantly, this work could guide some researchers to determine what kind of cell frames to choose, what kind of details to be aware of for different cell frames, and what is the optimal cell frame design for the BPE system. And what we have learned shows below:

- 1) a closed cell frame would be preferred compared to open cell frame for the uniformed potential gradient across the whole cell, if open cell frame was needed to use, to ensure a relative uniform and stable potential, the BPE width should be not wider than  $1/3^{\text{rd}}$  width of the driving electrode;
- 2) cell frame width does not affect the potential profile or solution potential gradient using the closed cell frame under same circumstances;
- 3) increasing the concentration of supporting electrolyte would decrease the slope of solution potential gradient;
- 4) the channel should be placed in the middle of the cell frames to give the maximum channel potential enhancement;
- 5) BPE should have the same length as the channel;
- 6) to maintain the potential across BPE at least 60% solution potential across the cell, and avoid the interference from the reactions happening at the

driving, the normalized cell width should not larger than 0.2 and normalized cell length should keep in the range of 0.4 to 0.8; 7) the potential across the channel is also described using several models (rectangle, trapezoid, ellipse 1<sup>st</sup> and ellipse 2<sup>nd</sup>) based on the variables of channel length and width, turns out the model of ellipse 2<sup>nd</sup> is most accurate, however, a final modeling function to predict and describe the channel potential is determined by averaging function of trapezoid and ellipse 1<sup>st</sup> due to the complicated math calculation of ellipse 2<sup>nd</sup>; 8) the potential profile in the channel is not that uniform; 9) channel cell frame does enhance the potential across the BPE (or lower down applied voltage to achieve same redox reaction happens on the BPE) compared with closed cell frame; 10) in terms of BPEs in a line arrangement, using cell frames with multiple small channels would be better than one channel for BPE system; as for BPEs in parallel arrangement, channels should evenly separate in cell frames in order to ensure BPEs have same potential.

Future directions, using ECL solution, study the ECL intensity distribution on the anodic driving electrode with current going through the driving electrode, more information or results may be obtained or verified.

### **5.3 Cathodic ECL Glucose Biosensor using Closed BPE System**

For this project, we report a new glucose biosensor platform based on cathodic ECL (electrochemiluminescence) in a closed BPE (bipolar electrode) system. In this C-ECL-C-BPE (cathodic ECL in a close BPE cell) glucose biosensor,  $Ru(bpy)_3^{2+}$  (tris(2,2'-bipyridyl) ruthenium) used as luminophore and  $K_2S_2O_8$  used as co-reagent to generate the cathodic ECL signal; two GCEs (glassy carbon electrodes), one acts as BPE cathode and the other acts as driving anode, used in the reporting cell; and a commercial test strip that already modified  $GO_x$  (glucose oxidase) and mediator used in the sensing cell. Under a certain applied DC voltage, a higher current would produce when glucose concentration varied from low to high, which need reduce more

$Ru(bpy)_3^{2+}$  and persulfate to compensate for it and result in a more intense ECL signal, using this mechanism, a successive of calibration curves achieved. And under optimized condition, a detection range of glucose from 3.8mM to 18mM achieved, and the limit of detection is calculated to be 3.8mM with a 0.2mM sensitivity. Moreover, two methods between proposed C-ECL-C-BPE glucose biosensor and commercial blood glucose meter has compared for determination of glucose in human serum samples, and the results show great similarity between these two methods. Most importantly, the proposed C-ECL-C-BPE sensor is a universal tool, easy to fabricate, cheap to use, fast to detect (only need 5 sec or even shorter time), has a great potential as a reliable analytical technique for detection of drugs, food analysis, environmental monitoring, scientific research and so on.

As for future directions, 1) to increase the sensitivity or adjust the detection range of interested analytes, many parameters could be optimized or change, such as the ECL solution composition, amplification voltage of PMT, modification of electrode used in the sensing cell (could do in the future), redesign the close BPE cell. 2) Modification reporting electrode to lower down the reduction potential, this one would be challenging, but worth to achieve.